DYNAMIC ADAPTIVE COLLOIDAL CRYSTALS FAR FROM EQUILIBRIUM

A THESIS SUBMITTED TO
THE GRADUATE SCHOOL OF ENGINEERING AND SCIENCE
OF BILKENT UNIVERSITY
IN PARTIAL FULFILLMENT OF THE REQUIREMENTS
FOR
THE DEGREE OF
MASTER OF SCIENCE
IN MATERIAL SCIENCE AND NANOTECHNOLOGY

By
ROUJIN GHAFFARI
AUGUST 2019

DYNAMIC ADAPTIVE COLLOIDAL CRYSTALS FAR FROM EQUILIBRIUM

By Roujin Ghaffari

August 2019

We certify that we have read thesis and that in our opinion it is fully adequate, in scope and in quality, as a thesis for the degree of Master of Science.

_____

Serim KAYACAN İLDAY (Advisor)

_____

Çağlar ELBÜKEN

_____

Simge ÇINAR

Approved for the Graduate School of Engineering and Science:

_____

Ezhan KARAŞAN

Director of the Graduate School

ABSTRACT

DYNAMIC ADAPTIVE COLLOIDAL CRYSTALS FAR FROM EQUILIBRIUM

Roujin Ghaffari
M.S. in Material science and nanotechnology
Advisor: Serim Kayacan İlday
August 2019

Self-assembly has been the center of attention of many researchers from all branches of science. Self-assembly of static structures such as crystals often forms through energy minimization, while dynamic ones need constant energy flow to maintain their state. Most of the studies on self-assembly are limited to static self-assembly, and despite its ubiquity in nature, our comprehensions of dynamic self-assembly are still in its infancy due to lack of experimental settings that can keep the system in its dynamical state. In 2017 a state-of-the-art dissipative (dynamic) self-assembly method was introduced by S. Ilday, and co-workers (*Nature Commun*., 2017). Here, using this method, we studied the formation of dynamic adaptive colloidal crystals far from equilibrium. We use a femtosecond laser as an energy source to drive a quasi-2D confined colloidal system far from thermodynamic equilibrium, and for the first time, we observed the formation of a rich set of dynamic adaptive colloidal crystals of tens to hundreds of units of polystyrene spheres, which interact through hydrodynamic and hard-sphere interactions. We report formation of periodic 2D Bravais lattices, Moiré patterns, honeycomb lattices and aperiodic quasicrystals. Furthermore, we identify, analyze, and verify some of the key experimental parameters, e.g., physical boundaries, thickness of the liquid film, and the average velocity of Brownian motion, affecting the formation of such a variety of colloidal crystals. We anticipate this study to be a starting point to uncover the physical principles behind the emergence of patterns from simple parts.

Keywords: Far from equilibrium, dynamic, adaptive, colloidal crystals, self-assembly.

ÖZET

DENGEDEN UZAK, DINAMIK, ADAPTIF KOLLOIDAL KRISTALLER

Roujin Ghaffari
Malzeme Bilimi ve Nanoteknoloji, Yüksek Lisans
TezYöneticisi: Serim Kayacan İlday
Ağustos 2019

Kendiliğinden birleşme, bütün bilim dallarından pek çok araştırmacının ilgi odağı olmuştur. Dinamik yapılar kendilerini sürdürmek için enerji akışı gerektirirken, kristal gibi statik yapıların kendiliğinden birleşmesi, genellikle enerjinin minimizasyonu ile gerçekleşir. Bu konu üzerindeki pek çok çalışma, statik kendiliğinden birleşmeyle sınırlı kalmıştır. Doğada yaygın olmasına rağmen, dinamik kendiliğinden birleşme hakkındaki çalışmalar oldukça yetersizdir, çünkü sistemi dinamik durumda tutabilen deneysel ortamlar kısıtlıdır. Bununla beraber, 2017'de, yeni bir dinamik kendiliğinden birleşme metodu S.Ilday tarafından tanıtıldı. (*Nature Communication, 2017*) Bu çalışmada da, bu yöntemi kullanarak dengeden uzak, dinamik adaptif koloidal kristallerin formasyonunu çalıştık. Quasi-2d koloid sistemini termodinamik dengeden uzak tutmak için, femtosaniye lazeri enerji kaynağı olarak kullandık. Sadece birbiriyle çarpışan ve etraftaki sıvının etkisindeki yüzlerce polystyrene kürelerden oluşan bu koloid sisteminde, ilk defa bu kadar çeşitli kristal desenleri gözlemledik. Bu çalışmada, periyodik 2D Bravais desenleri, Moire desenleri, honeycomb desenleri ve periyodik olmayan quasikristalleri gördük. Bununla beraber, bu çalışmada, sıvı filmlerin kalınlığı, Brownian ortalama hız gibi fiziksel sınırları, bu koloidal kristallerin formasyonunu etkileyen temel deneysel parametreleri tanımlayıp aynı zamanda bu parametrelerin analizini yaptık. Bu çalışmanın, basit parçalardan desenlerin ortaya çıkışının ardındaki fiziksel ilkeleri ortaya çıkarmak için bir başlangıç noktası olduğunu düşünüyoruz.

Anahtar kelimeler: Dengeden uzak, dinamik, adaptif, kolloid kristaller, kendiliğinden birleşme

ACKNOWLEDGEMENTS

Firstly, I would like to thank my advisor Prof. Serim Kayacan İlday, for providing
me with a great opportunity to be a member of her research group and guiding me throughout this project.

I am grateful to my groupmate and friend Dr. Sezin Galioğlu Özaltuğ for being not just a colleague but also a sister to me throughout my hard times.

Special thanks go to Dr. Ghaith Makey for his help with computer programs and video processing. I was fortunate to work alongside him, with his passionate participation and input, I was able to conduct this research successfully.

I want to thank all members of UFOLAB, specially Özgün Yavuz, for their technical support throughout my research.

Finally, I must express my very profound gratitude to my parents and my friends for providing me with unfailing support and continuous encouragement throughout this study and through the process of researching and writing this thesis. This accomplishment would not have been possible without them. Thank you.

TABLE OF CONTENTS

LIST OF FIGURES

LIST OF TABLES

Chapter 1

Introduction

We live in a world exhibiting fascinating order, from the structure of snowflakes to formation of planetary systems, but why do we get order instead of complete chaos? This mystery can be allayed through discovering and learning more about the concepts of self-assembly and organization[1], which created a new approach to answering the question of how order emerges[2].

Self-assembly is a process in which an organized structure spontaneously emerges from initially disordered individual parts[2]. Cells self-organize to form complex body organs, bacteria self-organize and form biofilms, people interact and social communities emerge. We are only beginning to understand such dynamic behavior, and as we do, we are finding that these very diverse systems share various similarities in their emergent phenomena.

Nowadays, the matter can be organized, shaped, and formed into desired structures using self-assembly techniques. The self-assembly paradigm has advanced significantly in chemistry, biology, and physics over the past few decades[3]; yet most of the previous studies on self-assembly are either limited[4] to static self-assembly[5,6], or studies on dynamic self-assembly which depend on specific materials and active particles[7,8] and specific interactions between building blocks and the energy source (*i.e.* chemical, magnetic, electrical, optical)[9–11]. Unlike the former studies, in this study we used a methodology for dynamic self-assembly of particles with does not require any functionalized building blocks and there is no specific interactions between the particles such as chemical, magnetic, electrostatic interactions.

Here, our study is based on a state-of-the-art experimental setting introduced by S. Ilday, and co-workers in 2017[4] for dissipative (dynamic) self-assembly of

colloidal particles far from equilibrium. The experimental setup is comprised of an ultrafast laser integrated with an inverted microscope system, where a quasi-2D confined colloidal system is used to study dynamic adaptive crystal formation[4]. The laser provides the energy flux, which creates spatiotemporal thermal gradients that leads the formation of Marangoni flows, which acts as the drag force for the particles towards their collection at a physical boundary, a gas bubble[4].

In this thesis, we report the first observation of dynamic adaptive colloidal crystals that emerge from non-functionalized polystyrene spheres, which interact through hydrodynamic and hard-sphere interactions[12,13]. Self-assembly process is governed only by the dominant physical forces of fluid flow and Brownian motion acting on the system[4,12,13].

The aggregates formed through this dynamic self-assembly process show a rich variety of colloidal crystals with symmetries of all 2D Bravais lattices, Moiré patterns, honeycomb lattices, and quasicrystals. An illustration of the quasi-2D system and the observed colloidal crystals can be seen in Figure 1-1.

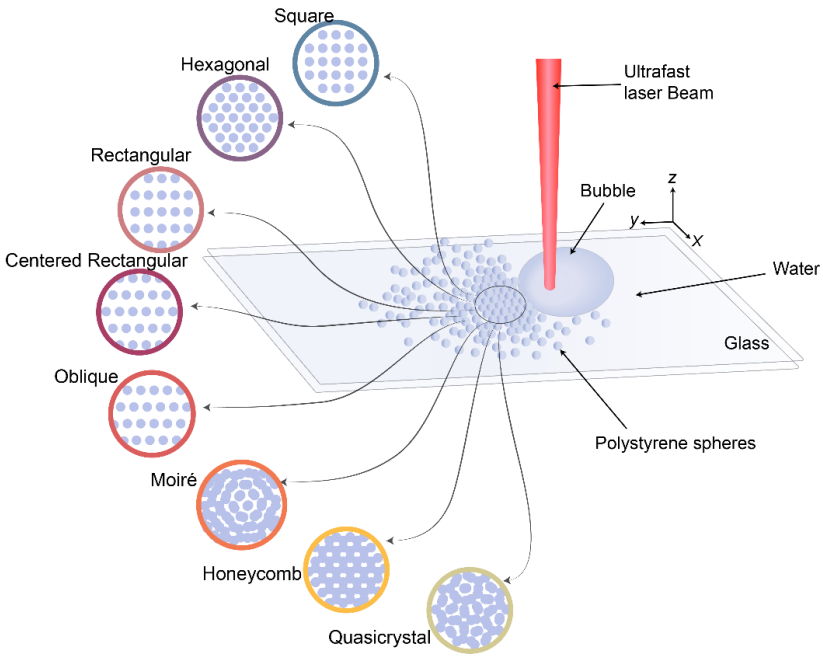

Figure 1-1 An illustration of the quasi-2D confined colloidal system and the variety of patterns emerged from the colloids.

Outline of this thesis is as follows**: Chapter 2** reviews a brief introduction to self-assembly and organization. This chapter also gives information on laser-induced

Marangoni flows and the Brownian motion of the particles. **Chapter 3** describes the methodology, sample preparation, experimental setting, fluid flow simulations, and video processing. **Chapter 4** discusses the experimental results and numerical simulations. Finally, **Chapter 5** concludes this thesis and reviews the results and achievements with their potential applications for future studies.

Chapter 2

Background

"Why then,
O brawling love,
O loving hate,
O anything of nothing first created!
O heavy lightness, serious vanity, Misshapen chaos of well-seeming forms!"

Shakespeare.

This famous quote of Shakespeare makes us wonder why do we get anything instead of nothing?

Nature spontaneously creates diverse complex structures ranging from galaxies to smallest ribosomes and proteins in nanometer scale. Nature's smart and efficient strategy of making ordered structures is through *self-assembly* and *organization*[1–4]. Living systems are the result of hierarchical self-organization of simple building blocks, and hence for a better understanding of nature, from the perspective of physics, chemistry and biology, we need to understand self-assembly processes[1].

The term "self-assembly" has been used in diverse research fields from social[14] to natural sciences[15]. Self-assembly is the process in which an ordered structure is spontaneously and autonomously emerge from pre-existing, initially disordered individual units[2]. Examples of self-assembly are ubiquitous in nature, as can be seen from Figure 2-1 A to C. Most of the research efforts are on mimicking similar pattern formations under laboratory conditions, as seen in Figure 2-1D. Self-assembly processes can involve building blocks of various sizes (from planetary systems and

galaxies to molecular scales in DNA and crystals), and different kinds of direct (e.g., electrostatic interaction between the parts[16]) or indirect (through the environment, e.g., phototactic response of artificial microswimmers[17]) interactions between the building blocks[18].

Self-assembly techniques used in research can be categorized into two classes: *i)* Static and *ii)* dynamic self-assembly[2,10,11]. Static self-assembly refers to the formation of patterns/structures through simple energy minimization[2,11]. In static self-assembly, the process of creating an organized pattern/structure is driven by an external energy flux[2] (for example in form of stirring[19,20]). Once formed, these structures can stay stable without the presence of an energy flux in the system[2,21]. Dynamic self-assembly, however, refers to the formation of patterns/structures that require constant energy supply to sustain their form or to transform to another configuration that is available to the system under nonequilibrium conditions[2,22]. Once the energy source is cut off from the system, self-assembled patterns/structures disassembles into their thermodynamic minimum energy configuration[2].

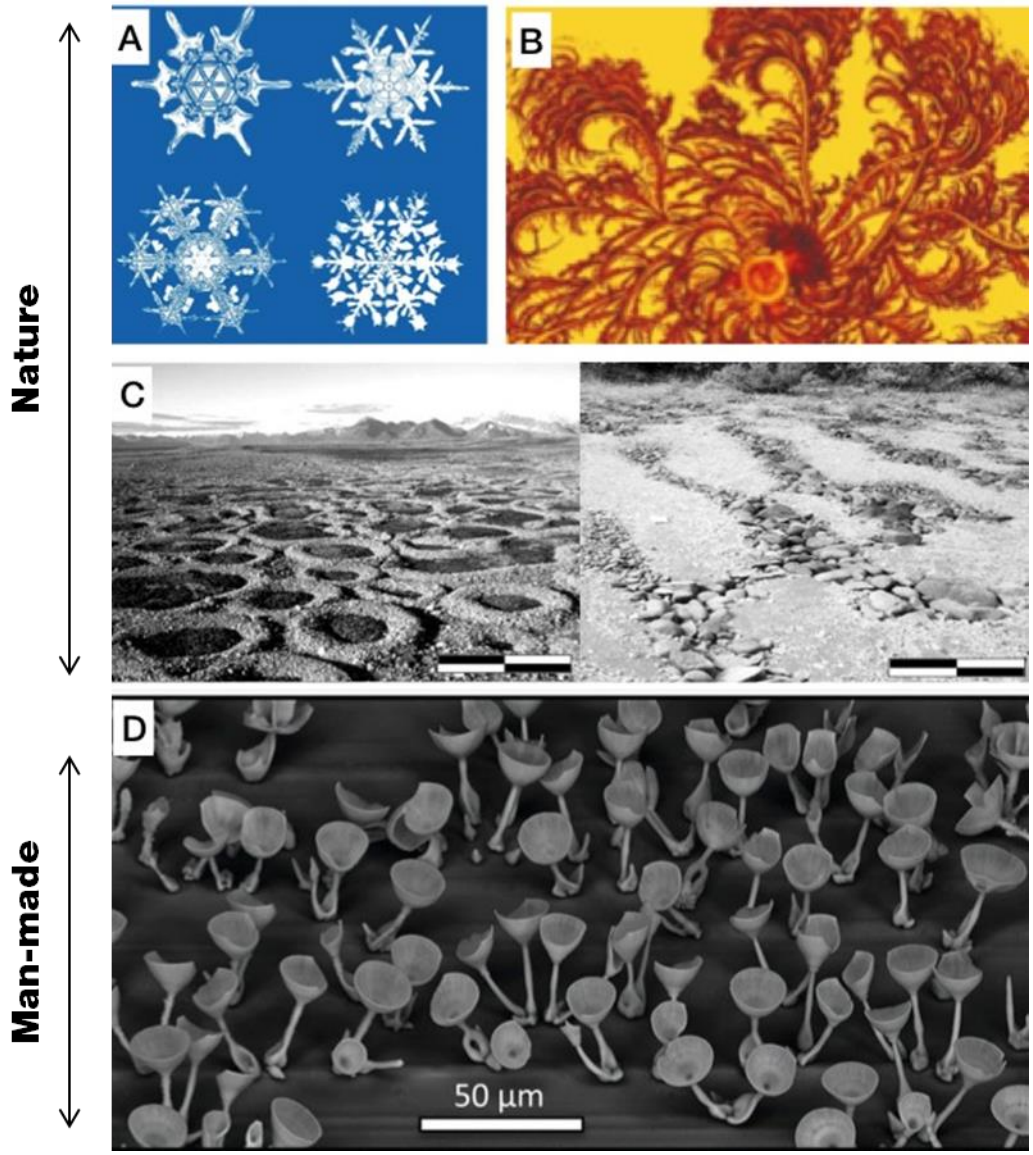

Figure 2-1 Examples of self-assembly and self-organization in nature; A) Photographs of snowflakes exhibiting various self-organized patterns (magnification x400)[23]; B) A pseudo-colored image of patterns formed by swarming *Paenibacillus Dendritiformis* bacteria[23]; C) Types of self-organized sorted pattern ground that shows circles (left; scale bar ~2m) and stripes (right; scale bar ~1m)[24]. Examples of self-assembly and self-organization that mimicks similar pattern formations seen in nature under laboratory conditions; D) Carbonate-silica microstructures developed in a dynamic reaction-diffusion system by carefully controlling diffusion of carbon dioxide in barium chloride and sodium metasilicate solution[25]. [Reprinted with permission from (A,B) Ref[23]; (C) Ref[24]; (D) Ref[25].]

2.1 Static self-assembly

Figure 2.2 shows some of the examples to static self-assembly research: In Figure 2-2A the researchers show concentric circle patterns of 50 μm glass spheres on a patterned polystyrene substrate. The patterned substrate was made using reactive wet stamping method (r-WETs) and the patterned regions were formed by locally oxidizing pendent groups of polystyrene. The glass spheres (building blocks) then were mechanically agitated on the polystyrene patterned substrate, exchanging more charges with oxidized regions than unoxidized ones, resulting in self-assembly of spheres on the patterned regions in concentrated circle configuration[26]. In this example, self-assembly process was provoked by electrostatic forces. Once the structures were formed, the electrostatic interaction between substrate and glass spheres keeps the spheres in their minimum energy position which ensures their stability over time.

In the second example (Figure 2-2B) complex hierarchical carbonate-silica microstructures were self-assembled by carefully controlling diffusion of CO_2 in a mixed solution of barium chloride and sodium metasilicate[25]. Precise modulation of pH, temperature, and CO_2 concentrations was used to modify chemical gradients which were the driving force for growth of complex flower like metasilica microstructures in solution of barium chloride and sodium metasilicate[25]. Molecules of silica and barium carbonate were the building blocks of this hierarchical structures. The morphology of self-assembled structures depends on conditions of the growth solution (e.g., pH, temperature, salt concentrations). Once these structures were formed, the growth solution was replaced with pure water to remove the chemical gradients and stop the reactions. Following this step, the structures were moved to acetone and afterwards dried in ambient air. The final structures were reported to be thermodynamically stable and static.

Figure 2-2C shows another example of static self-assembly. Here, the building blocks were cubic shaped magnetite nanocrystals (average edge length of 13.4 nm), which were self-assembled into helical superstructures at the air-liquid interface in the presence of magnetic fields. Complex structures such as helices can be obtained through self-assembly of nanocubes of magnetite, driven by competition between magnetic dipole-dipole, van der Waals interactions, and Zeeman coupling[27]. The

researchers used a drop of cubic magnetite particles dispersed in hexane, containing excess oleic acid on diethylene glycol-air interface while experiencing magnetic field. Since the size of the particles was within the superparamagnetic regime, the dipoles of individual nanoparticles were able to flip direction randomly because of the fluctuations in temperature. Initially random dipoles aligned partially in the presence of magnetic field, which made it possible for magnetic dipole-dipole coupling between the particles. As liquid evaporated, chains of magnetite nanocubes were formed, and the final structures were dried and moved to a substrate of choice. Finally, the competition between the magnetic and spatial symmetries gave rise to the formation of chiral nucleus of nanocubes, which resulted in formation of helices. Simulations were reported to show formation of helices was coupled with free energy minimization, where final structures were at equilibrium and stable.

An example of DNA assisted self-assembly is shown in Figure 2-2D where the researchers used short synthetic DNA strands (DNA bricks) as building blocks to form arbitrary 3D structures[28]. These DNA bricks were single stranded, consisting of 32 nucleotides, which had 4 binding domains. The interaction between DNA bricks was reported to follow simple local binding rules. By carefully designing the DNA sequences and one-step annealing reactions, the researchers were able to self-assemble more than one hundred 3D static structures from specified DNA bricks[28]. Desired 3D shapes were formed by simply mixing pre-synthesized DNA bricks. Since the final 3D structure depended on the sequences of the DNA bricks, the researchers used a software, which predicted the necessary bricks that should be mixed to give the desired 3D shape. Then, a liquid-handling robot mixed the mixture of the software picked bricks and equilibrium 3D structures formed according to local binding rules between various DNA sequences.

Another example is given for two-dimensional self-organization of Brownian square crosses in Figure 2-2E[29]. Researchers showed formation of complex 2D structures by raising 2D area fraction of hard colloidal square crosses dispersed in an aqueous solution in a quasi-static manner. In this study building blocks were the colloidal square crosses (end to end length: 4.2μm), the researchers formed a monolayer of colloidal square crosses at the bottom of a rectangular optical cuvette and tilted the cuvette at the angle of ~1º, they waited for a minimum of 2 months for equilibration. This formed a slowly varying area fraction, as the area fraction increases a disordered isotropic phase (Figure 2-2E, left image) changes into an ordered phase

(Figure 2-2E, right image). Since increasing the area fraction was done in quasi-static way the final structure was reported to be at equilibrium stable. The equilibrium structure was an entropically favored ordered phase (a self-organized structure at which combined translational and rotational entropy of the system was maximized). The entropy maximization principle for the equilibrium process here was reported to be dependent on the shape and geometry of the particles, which follows the entropomorphism principle[29].

Self-assembled colloidal arrays of square and hexagonal patterns is shown in Figure 2-2F. In this study researchers formed latex colloidal particles (~380 nm in diameter) into two packing configurations of colloidal crystals by deposition of the particles on an inclined plane. Latex colloidal particles were obtained by adding an aqueous solution containing $(NH_4)_2S_2O_8$ and NH_4HCO_3 and the monomer mixture consisted of styrene (St), methyl methacrylate (MMA) and acrylic acid (AA) (90:5:5) into a flask. After stirring the mixture for 5 hours under N_2 atmosphere, latex colloidal particles were formed. This solution then diluted 50 times, in which a pretreated silicon wafer (at 70-75 °C in a H_2SO_4/H_2O_2 (7:3 v/v) mixture for 30 minutes) with hydrophilic surface was dipped into the solution with a 45º angle. The self-assembly of the latex particles was controlled by the capillary force, evaporation rate of the water from solution, and free motion of the particles: As the water evaporated, the capillary force pushed the particles to move upwards on the wafer and dry there. Temperature and the rate of evaporation were reported to be the key parameters that controls the formation of crystals. They reported that when the evaporation was at room temperature (25ºC), latex particles formed hexagonal patterns, which is thermodynamically favorable, close-packed arrangement of the spherical particles. However, when the evaporation process was taking place at lower deposition temperature of 0ºC, latex particles formed through dislocation induced square patterns. This is so because at lower deposition temperatures kinetic energy of the particles decreases, which slows down the movement of the particles that leads to the formation of non-close packed arrangements of square patterns over large areas. Higher temperatures of 50ºC or 75ºC on the other hand were reported to speed up the evaporation rate and increased kinetic energy of the particles, therefore fasten their movement, which resulted in formation of disordered arrays. It was explained that the capillary force was related to the surface tension of a liquid; higher surface tension induced higher capillary force, which was reported to be in favor of forming hexagonal patterns. When surfactants were added

to the colloidal solution, formation of arrays of particles with larger space in between (*i.e.* square patterns) was reported to be more probable. Once the structures were formed, the samples were dried to stabilize the formed geometries[30].

Colloids have been introduced as "artificial atoms" to study the formation and evolution of natural crystals, since their characteristics are superficially similar to atoms and the crystals that they form can be model systems to natural crystals, and it is possible to observe the motion of these "artificial atoms" and the crystals that they form under the optical microscope[31]. Studying self-assembly of colloidal crystals is also quite important to scrutinize *e.g.*, the crystallization process, effects of imperfections to the crystals[32], nucleation and growth phenomena[33,34], and phase transformations[31,35].

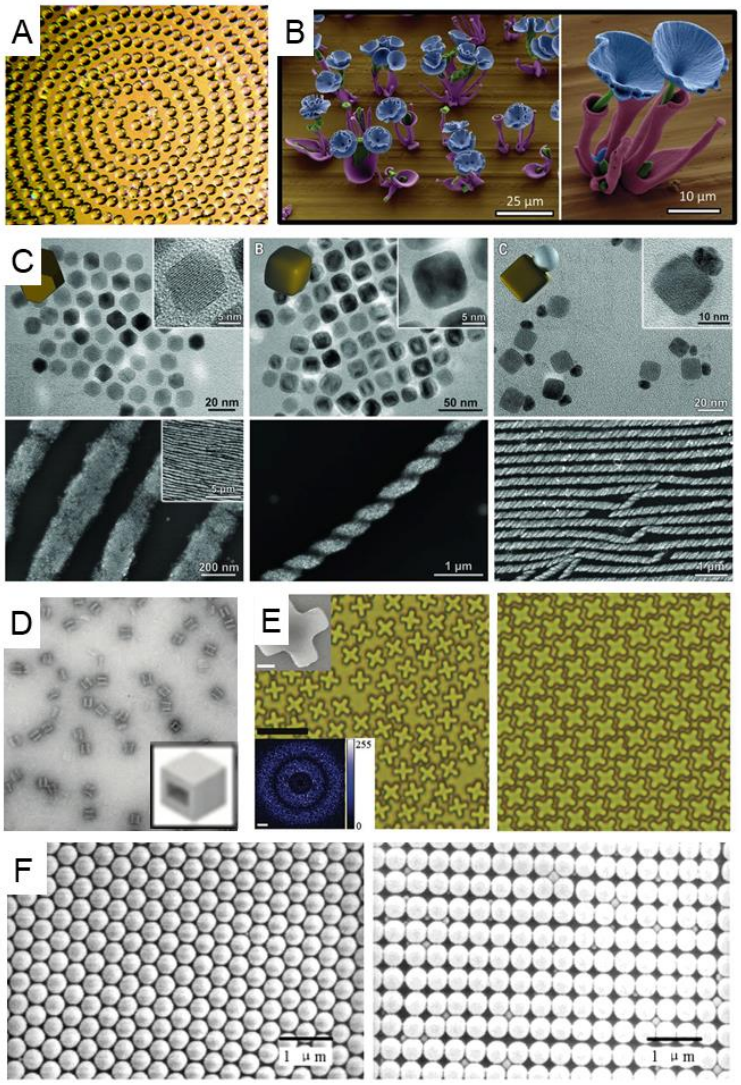

Figure 2-2 Examples of static self-assembly studies in the scientific literature; A) Electrostatic self-assembly of polymeric microspheres on a charge exchanging substrate made through reacting wet stamping (r-WETs) method[26]; B) Psuedo-colored SEM images of $SrCO_3$-SiO_2 microstructures developed in a dynamic reaction-diffusion system[25]; C) Fe_3O_4 nanocrystals self-assembled into helical structures[27]; D) DNA assisted self-assembly using short specific single stranded DNA sequences (DNA bricks) as building blocks[28]; E) Optical micrograph and Fourier transform image of isotropic Brownian square crosses (left) and self-assembled achiral rhombic crystal phase (right)[29]; F) SEM images of hexagonal and square arrays of P(St-MMA-AA) monodispersed copolymer latex colloidal crystals formed using an inclined plane and capillary force [30]. [Reprinted with permission from (A) Ref[26]; (B) Ref[25]; (C) Ref[27]; (D) Ref[28]; (E) Ref[29]; (E) Ref[30]]

Self-assembled colloidal structures are also technologically important owing to the possible applications of self-assembled colloidal structures in band gap materials (photonics devices with tunable band gaps to tailor light)[36–38], sensors[39], drug delivery[40], catalysts[41], templates[42] and more. Figure 2-3 shows some examples of technological applications of self-assembled colloidal structures. In Figure 2-3A, H. Cong and B. Yu (2010) used organic colloidal crystal templates because of their catalytic activity to make superparamagnetic macroporous Fe_3O_4[43]; Figure 2-3B shows a polymeric membrane reactor developed by K. Song and I. Kretzschmar (2009) using polystyrene colloidal arrays as templates[41]; Figure 2-3C shows a study on ordered silicon cone arrays by X. Zhang et.al. (2009). The researchers used ion etching on 2D silicon colloidal crystals to form silicon cones with controllable morphologies[42]. H. Fudouzi and Y. Xia fabricated colloidal crystals with tunable stop bands (*i.e.*, structural colors) using liquids (Figure 2-3D). Researchers prepared colloidal crystals of polystyrene spheres, lattice constant (thus Bragg-diffracted wavelength) of which can be altered by applying a liquid, capable of swelling on top of them[38]. Figure 2-3E shows a flexible polymer laser device made out of colloidal crystals by S. Furumi *et. al.* (2007)[37].

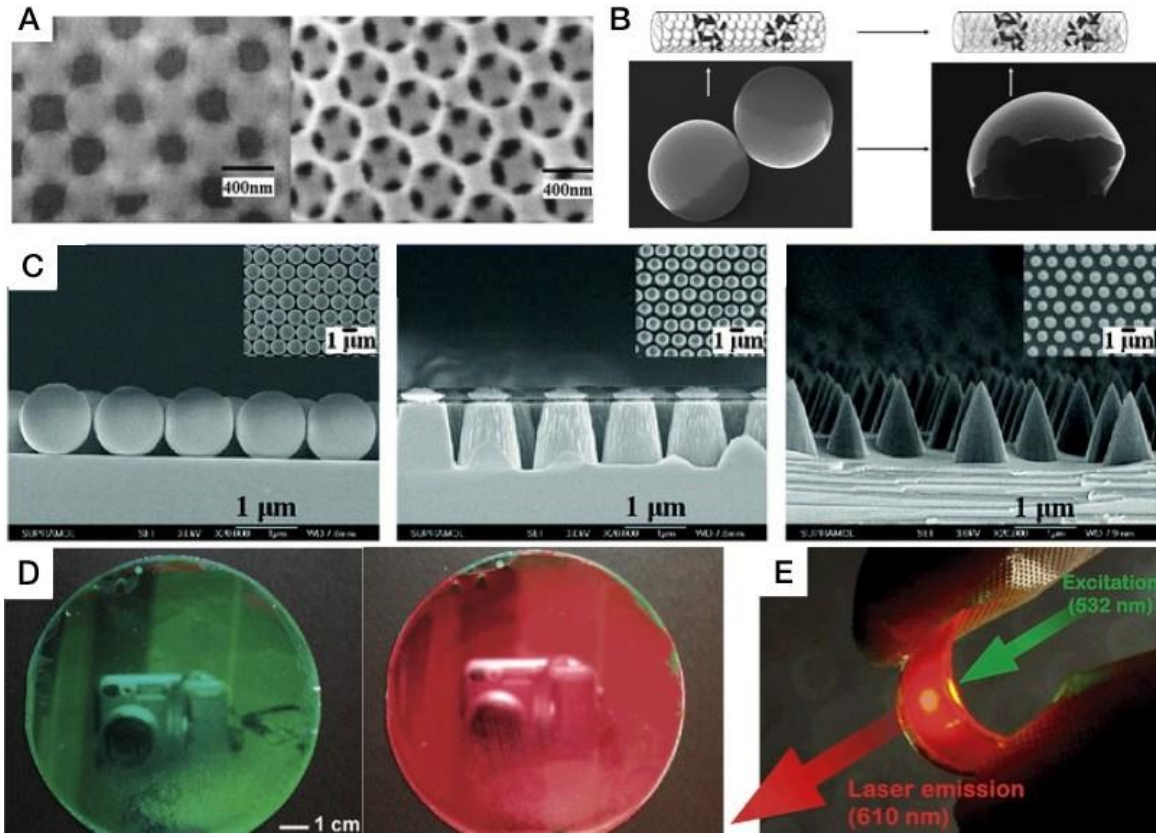

Figure 2-3 Applications of colloidal crystals; A) SEM image of colloidal crystal template filled with inorganic materials(left), inorganic macroporous structure left after sintering and eliminating the template (right)[43]; B) Fabrication of polymeric catalytic membrane reactor using templates of alternating assemblies of surface-anisotropic and plain polystyrene (PS) colloids[41]; C) Fabrication of silicon cones arrays using self-assembled silicon colloidal crystals as mask and ion etching[42]; D) Photographs of a photonic paper made of a thin film of colloidal crystal[38]; E) Flexible polymer laser devices excited by low-threshold optical light fabricated from colloidal crystals[37]. [Reprinted with permission from (A) Ref[43]; (B) Ref[41]; (C) Ref[42]; (D) Ref[38]; (E) Ref[37]]

As explained above, most of the studies on self-assembly and organization was focused on formation of static self-assembled structures[1] because most of the technological applications are based on static structures[44], however, to investigate dynamic adaptive behavior of these crystals or their emergent phenomena[45] such as early stages of crystallization and phase transformations[46], general principles that guide dynamic self-assembly[8], and structures that cannot be observed at equilibrium[47], we need dynamic self-assembly methodologies.

2.2 Dynamic self-assembly

Contrary to the static self-assembly where the formed structures are at equilibrium[2], dynamic self-assembly refers to the formation of structures under nonequilibrium conditions, which are sustained as long as there is continuous energy supply[10].

Figure 2-4 shows some of the examples to dynamic self-assembly studies: One of the most famous example is the so-called Rayleigh-Bénard convection cells, seen in Figure 2-4A[48]. These cells are formed through heating a liquid from below and cooling it from above. The density of the liquid used in these cells are dependent on the temperature gradient between the top and bottom of the liquid film. The mechanism of pattern formation is as follows: Heated liquid film from the bottom moves up due to the lower density of the liquid at the bottom and the temperature dependence of the Buoyancy forces, while the cooler liquid with higher density of the top sinks down[49], resulting in formation of convective cells. Presence of heating source is crucial for the existence of these cells and if the heating source below the liquid is eliminated at any time, the system proceeds toward equilibrium, the liquid temperature will homogenize throughout the system and given enough time the convective cells will disappear[50].

Another well-known example of dynamic pattern formation is the so-called Belousov–Zhabotinsky (BZ)[51,52] oscillatory chemical reactions, seen in Figure 2-4 B. Here, the system is typically the mixture of bromine, malonic acid, and a redox catalyst such as $Ce^{3+/4+}$ [53]. Once these chemicals are mixed, a series of reactions take place with many steps[54] but the overall reaction is given as below[55]:

$$3\ CH_2(CO_2H)_2 + 4\ BrO_3^- \rightarrow 4Br^- + 9\ CO_2 + 6\ H_2O$$

The oscillatory BZ reactions emerges in a reaction-diffusion system[48,56]. Oxidation of malonic acid in the presence of BrO_3^-, Br^-, and the catalyst is the driving force of these reactions[53]. After a series of reactions, the concentration of bromide changes. When the concentration is high, bromine is produced and bromide is consumed, as a result its concentration decreases. If bromide concentration drops below a certain threshold number, oxidation of the redox catalyst alongside the production of $HBrO_2$ in an autocatalytic process takes place. In this step, there will be a visible color change of the mixture due to the full oxidization of the catalyst. At this

point, the bromomalonic acid degrades, as a result, bromide is produced. The redox catalyst is reduced again, which initiates a color change of the mixture again. Then the cycle goes back to the point where the bromide concentration increases again, which lead to the periodic reaction oscillations in the system[53,57].

The BZ reaction is a nonlinear oscillatory reaction, represented by the balance between two main processes: oxidation and reduction of a catalyst between $+n$ and $+(n-1)$ states, which usually varies in color[58]. Patterns formed in BZ systems are unstable and are continuously formed and destroyed. There are many studies on controlling spatiotemporal dynamics in chemical systems based on, periodic forcing[59], and imposing medium heterogeneities/noise[60,61] or geometrical constraints[62]. These nonlinear systems are inherently sensitive to small perturbations, for example a specific configuration can be changed or stabilized by imposing very small perturbations, some coherent structures can be seen in noise imposed systems that do not exist in noise free media[63]. Chemical oscillatory reactions usually consist of two reaction pathways: an energy releasing path and an energy consuming path. One of the pathways produces an intermediate product and the other pathway consumes it. The reactions periodically switch from one path to the other triggered by the alteration of concentration of the intermediate product[64]. Here, the energy required for dynamic self-assembly is provided by the energy releasing reactions, and the free energy monotonically decreases[64]. Concentration of reactants continuously decrease and that of products continuously increase in an oscillatory reaction, only the concentration of intermediate species and catalysts can oscillate[64,65].

Self-organization can be seen in more complex biological systems such as school of fish (Figure 2-4 C) or flock of birds. In this case, the building blocks (*i.e.* fishes or birds) are complex biological systems. More than 50% of fish species show synchronous movement, whereby groups of fish can be especially large and the members of the group do not have interactions with all the members of their group. They only interact with the members present in their immediate vicinities[66]. Here, each fish continuously modifies its position with respect to other surrounding fishes. This collective motion is beneficial for fishes in order to hunt or evade the predators (evolutionary advantage), which is the driving force of this self-organization.

Figure 2-4 D shows a study on dynamic self-assembly of magnetized, millimeter-sized objects to provide an experimental demonstration to test the stability theories of interacting point vortices and vortex patches as well as finding a better

understanding of dynamic self-assembly by B. A. Grzybowski *et. al.* (2000)[11]. The objects spin at a liquid-air interface due to changes in magnetic fields. The disks (~1 mm inside diameter and ~2 mm outside diameter) were fabricated by filling hallow rings of polyethylene with magnetite doped polydimethylsiloxane (PDMS), then dispersed at air-liquid interface. A permanent magnet was set 2-4 cm below the interface. When the magnet was not moving, the disks were aggregated toward the poles of the magnet. When the magnet started rotating the disks formed hexagonal patterns with centers on the axis of rotation of magnet. They were also spinning around their centers. The ordered patterns were formed due to the balance between magnetic attractions and hydrodynamic repulsions associated with spinning of disks around their centers (Figure 2-4 D-b). required the provided field magnetic dynamic The .assembly-self dynamic for flux energyThe disks retained their shape for as long as there is dynamic magnetic field but once the magnet stopped, the disks lose their order. The researchers conducted the experiments for different number of disks and showed when there were 10 and 12-membered aggregates, the patterns constantly changed between two available polymorphs. Polymorphs are different configurations with the same set of building blocks. In case of 19 disks they show two polymorphs, one of which only appears when rotation speed of magnet was above a certain threshold. Maximum number of disks that can be used in this system is 19, the reason is that when the aggregates become bigger, less homogenous magnetic field was applied to the outermost disks than the disks placed in the center, hence they stopped spinning.

More recent demonstration of dynamic self-assembly was published by J. Palacci *et. al.* (2013)[9] (Figure 2-4 E). The researchers used functionalized 3-methacryloxypropyl trimethoxysilane (TPM) polymeric spheres (1.5 μm in diameter) with a hematite cube (600 nm in length) embedded in them, immersed in a solution containing H_2O_2, tetramethylammonium hydroxide, and sodium dodecyl sulfate (SDS). The self-assembly process was driven by an externally applied blue light, which catalyzed the decomposition of H_2O_2 in the liquid medium, creating thermal and chemical gradients that induce phoretic motion needed for self-assembly. When the blue light was turned on, clusters start forming after ~25 seconds, formation of aggregates took ~200 seconds. As soon as the blue light was turned off, the aggregates start dissolving, after ~100 seconds aggregates have dispersed completely. The only symmetry observed in this study was two-dimensional hexagonal clusters out of ~35 particles, which is the thermodynamically favored close-packed arrangement.

Another study on dynamic self-assembly tried to bridge the gap between static and dynamic self-assembly, which is given in Figure 2-4 F (J.V.I Timonen *et. al.* 2013)[10]. The researchers introduced a system that can alternate between static and dynamic self-assembly of ferrofluid droplets, placed on super hydrophobic surfaces, by switching between static and oscillating external magnetic fields. First, they created ferrofluid droplet patterns (such as hexagonal pattern shown in Figure -F 4-2 they then field, magnetic static external applying by droplet parent one from (I static the that show and field magnetic oscillating to switched equilibrium patterns obtained by static magnetic field can change into dynamic structures. Transformation to dynamic structures can only be seen when the oscillating magnetic field provides sufficient energy flux to keep the structures away from thermal equilibrium. If the energy flux was not sufficient, droplets simply move along the hydrophobic substrate with the oscillating magnetic field (close to thermodynamic minimum energy configuration). There was a threshold of amplitude and frequency of the magnetic field, above which emergence of various dynamic patterns were observed such as formation of 6 droplets (Figure 2-4 F-II), or 4 droplets (Figure 2-4 F-III) from originally 7 droplets in hexagonal order (Figure 2-4 F-I); or formation of line-like structures from combination of multiple droplets (Figure 2-4 F-IV to X). Similar to the other dynamic self-assembly studies the structures in this study switched to their thermal equilibrium configuration as soon as the energy flux (here, oscillating magnetic field) was eliminated.

Figure 2-4G shows a study on far-from-equilibrium dynamic self-assembly of colloids by S. Ilday *et. al.* (2017)[4]. The researchers used femtosecond laser-induced Marangoni flows to form colloidal aggregates. 500-nm pure polystyrene colloidal particles were used as the building blocks. Femtosecond laser was the energy source here, that was focused on a colloidal solution sandwiched between two thin glass slides. When the laser was off, particles were at thermal equilibrium and doing random Brownian motion, when the laser was turned on, the system was driven to far from equilibrium since nonlinear absorption of femtosecond laser pulses by the glass and the liquid created spatiotemporal thermal gradients. Also, due to localized heat deposition, the liquid under the laser beam boiled and formed a gas bubble. The gas-liquid interface and laser induced thermal gradients set up Marangoni flows, which dragged the particles toward laser spot to form aggregates.

Unlike the former studies discussed here, they did not use any functionalized particles. The self-assembly did not depend on the specific interactions such as chemical, magnetic, electrostatic interactions. The only interactions between particles were of hard-sphere and hydrodynamic type. Using this methodology they were able to manipulate tens to thousands of particles, whereas in the aforementioned studies (Figure 2-4 D,E,F) the number of building blocks are very limited and the spatial and temporal manipulation usually were not relevant to the dynamics of their systems. Also, they were able to show, for the first time, different symmetries of dynamic adaptive colloidal crystals such as hexagonal, square, oblique lattices as well as Moiré patterns. The researchers showed that they can control the size of the aggregates, as well as the bubbles by changing the laser power and beam position. By controlling the size and shape of the bubbles they can create new physical boundary conditions and observe the immediate effect of them on formation of various patterns without the need for any prior modification to the experimental setup. Lastly, they showed that the colloidal aggregates exhibited a rich set of life-like behaviors such as autocatalysis, self-regulation, self-replication, competition and self-healing.

All of the systems discussed above and others that are dynamically self-assembled operate out of equilibrium when the energy is dissipating[1,2,67,68]. A system is at its thermal equilibrium when its state variables stays constant over time. On the other hand under non-equilibrium condition, there is continuous flow of energy and matter, thus, the state variables are not constant over time[49].

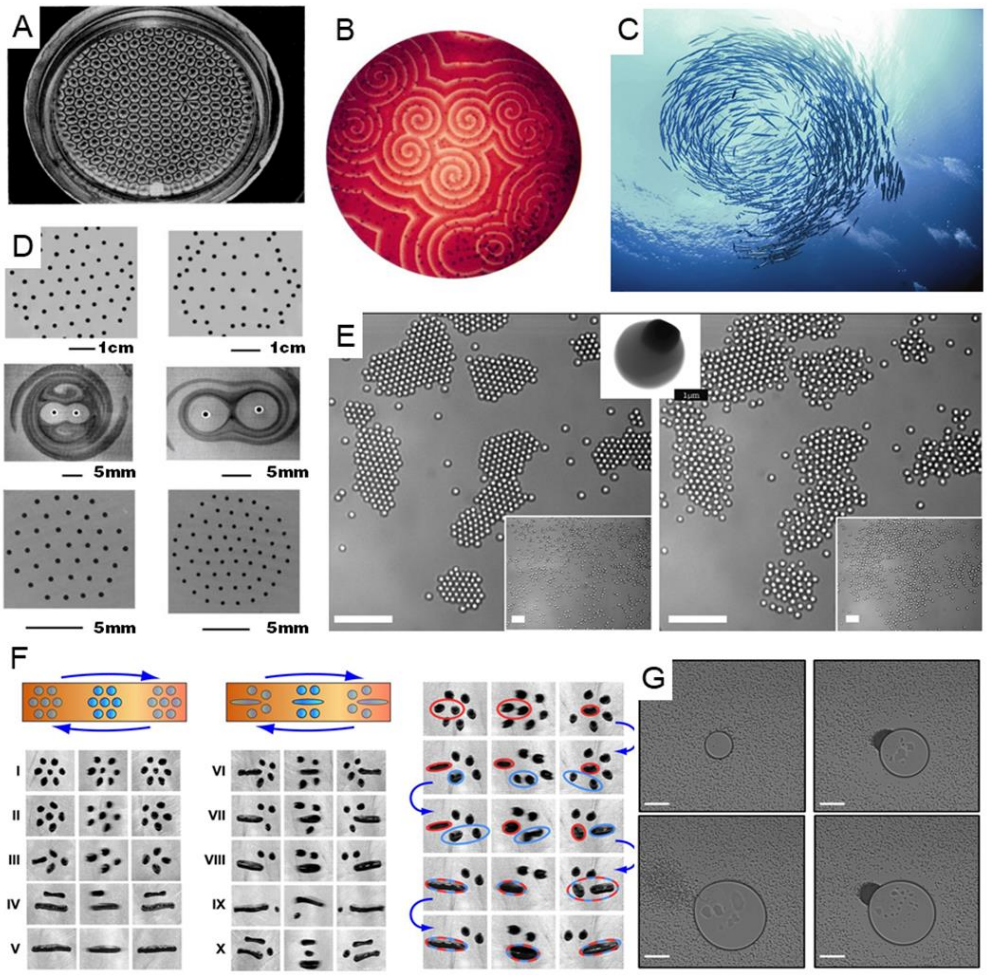

Figure 2-4 Examples of dynamic self-assembly and organization in scientific literature; A) Rayleigh-Bénard convection cells in silicone oil under an air surface[48]; B) Belousov–Zhabotinsky reaction, a classical example of non-equilibrium self-assembly, C) Dynamic self-organization of a school of fish; D) Dynamic self-assembly of magnetically-rotating millimeter-sized disks at the liquid-air interface[11]; E) Living crystals, dynamic self-assembly of TPM (3-methacryloxypropyl trimethoxysilane) polymeric spheres with embedded hematite cubes under the blue light (left), and melting of colloidal clusters when light is turned off (right; scale bar is ~10 μm)[9]; F) Switching between dynamic and static self-assembly of ferrofluid droplets on super hydrophobic surface by changing between static magnetic field to time variating magnetic fields[10]; G) Dynamic self-assembly of pure polystyrene spheres far from equilibrium using laser-induced flows (scale bar is ~40 μm)[4]. [Reprinted with permission from (A) Ref[48]; (D) Ref[11]; (E) Ref[9]; (F) Ref[10]; (G) Ref[4]].

Dynamic self-assembly is regarded to be quite important among biologists (to understand organization of cells and organs), physicists (to expand the non-

equilibrium thermodynamics), and chemists (to create self-assembling chemical networks and develop new methodologies for synthesis)[69]. Therefore, studies on dynamic self-assembly can contribute to more understandings on the principles of dynamic self-assembly from fundamental point of view.

2.3 Dynamic self-assembly of colloidal particles far from equilibrium

Diverse scientific and technological applications of colloidal particles make colloidal studies an active area of ongoing research. Most of the previous studies on colloidal self-assembly[4] were limited to static self-assembly[5,6]. Researches on dynamic self-assembly were mostly based on specific materials and particles (active particles, patchy particles)[7,8], and certain interactions between parts (magnetic, chemical, etc.) and the energy source[9–11]. Quite recently, S. Ilday *et. al.* (2017) introduced a unique, dynamic far-from-equilibrium self-assembly methodology that is independent of the materials (e.g., type, size, geometry) it uses and the microscopic details of the system[4,13] Here, using this methodology in this thesis, we investigated dynamic adaptive colloidal crystals of a multiplicity of patterns formed by non-functionalized, pure polystyrene colloidal spheres with 500 nm diameters. We present dynamic adaptive crystal symmetries in a wide range of arrangements from simple periodic 2D Bravais lattices, namely, square, rectangle, centered rectangle, hexagonal, and oblique, to more complex arrangements of Moiré patterns, honeycomb lattices, and aperiodic quasicrystals[13].

The methodology is described as follows: A femtosecond laser is used as the energy source for dissipative self-assembly, which is focused on a quasi-2D confined solution of 500-nm-sized pure polystyrene spheres that are sandwiched between two thin glass slides, shown in Figure 2-5.

At the laser wavelength of 1μm all the materials used in the sample are optically transparent and the energy intake is based on multiphoton absorption of the laser pulses[4]. Laser heats up the glass and the water, creating a hot spot. The rest of the system stays relatively cold. This spatiotemporal thermal gradient creates Marangoni flows[70]. Simultaneously, the localized heat deposition boils flithe water and creates a gas bubble at the liquid-glass interface. Marangoni flows drag the particles toward their aggregation at the bubble boundary. Spatiotemporal thermal

gradients induced by the femtosecond laser drives the system far from equilibrium, and the nonlinearities in the system give rise to multiple fixed points in phase space (the dynamical space in which all the possible states of a system are presented), which present us with the possibility to observe a number of dynamic adaptive patterns in the system.

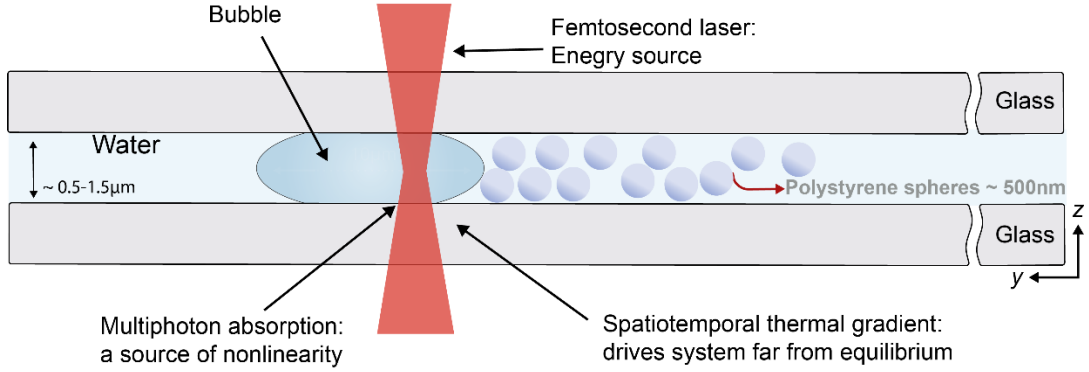

Figure 2-5 An illustration showing the cross-section arrangement of the experimental setting, where a colloidal solution is sandwiched between two thin glass slides with a femtosecond laser beam focused on the sample, due to the localized heat deposition the water boils down and creates a vapor bubble, which serves as a physical boundary for particles to hit and collect[4].

Well-controlled spatiotemporal gradient forms nonlinear feedback loops due to two counter-balanced physical forces: A negative feedback between the aggregate and the Brownian motion of the particles, and a positive feedback between the aggregate and the fluid flow[4]. The balance between these forces determines whether an aggregate grows or not and we are able to control this system through these intrinsic feedback loops (Figure 2-6).

Depending on the laser power, the positive feedback can overcome the negative feedback and the aggregates grow or they are comparable so that the aggregates can stay stable. When the laser is turned off, there will be no positive feedback, there is only negative feedback so the aggregates start dissolving due to random Brownian motion of particles[4,12,13] (Figure 2-6).

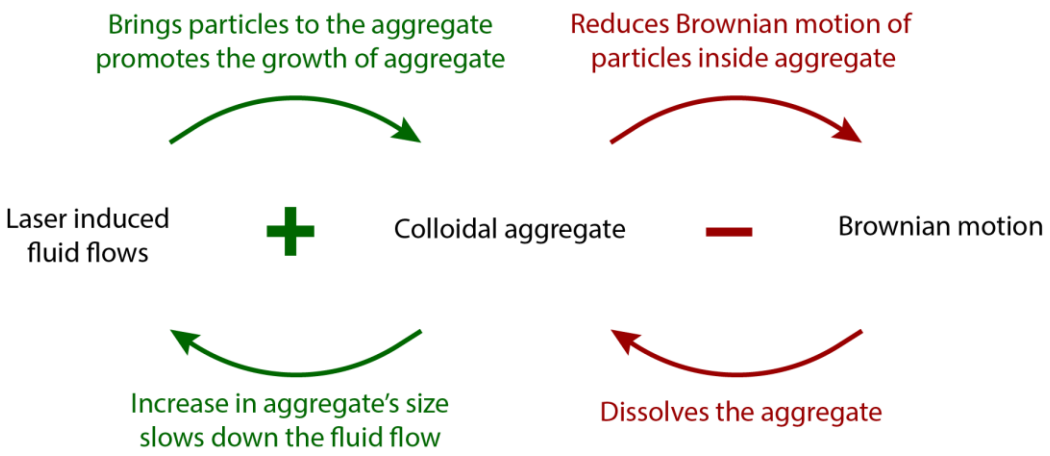

Figure 2-6 Nonlinear feedback loops present in the system; Counter balanced forces of Brownian motion and laser induced flows will create a feedback loop which can be controlled by turning the laser off and on. Positive feedback is between the aggregate and fluid flows, flows continuously bring particles toward aggregate to grow and as the aggregate grows in size it slows down the fluid flow. Negative feedback is between the aggregate and Brownian motion; Brownian motion dissolves the aggregate and when an aggregate is formed the Brownian motion of particles inside it would be reduced[4].

when the laser is turned on positive feedback is formed (laser induced flows) and the aggregates will grow, if the size of aggregate grows larger than a threshold, it can alter the flows[4] and the growth slows down due to negative feedback (Brownian motion of particles on edges of aggregate) which regulates size of the aggregate and prevents its further growth, also when the laser is turned off, negative feedback overcomes the positive feedback and the aggregate will disperse.

For better understanding of Marangoni effect consider a glass of wine; if you hold up the glass, you will see teardrops on the glass running down. These tears of wine are caused by the surface tension gradient on the interface between two fluids (here liquid-gas) which causes mass transfer alongside the interface, called Marangoni effect[71]. Such gradient can be created by the differences in composition or temperature of the solution along this surface. Surface tension is a property defined at an interface. It is the energy needed to expand the surface area of interface by one unit[72].

Figure 2-7 shows a liquid phase in contact with its vapor. The molecules at the interface have asymmetrical force applied on them by the liquid to pull the surface of liquid together, while molecules in the bulk have symmetrical interactions in all

directions. To expand the surface area of liquid. Molecules in the bulk need to go to surface and break their interactions which requires energy.

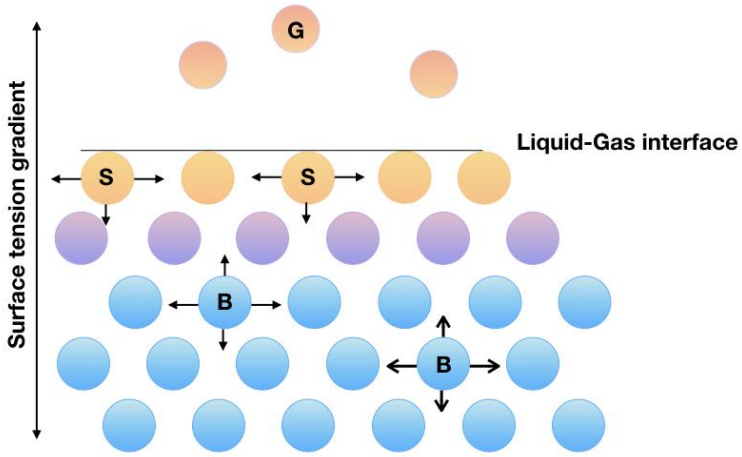

Figure 2-7 Surface tension in a liquid in contact with gas; The molecules at the surface (labeled with S) experience asymmetric interactions, molecules below the surface (violet) undergo slightly more isotropic interactions, while the molecules in the bulk (labeled with B) experience isotropic interactions[71].

For the cases where surface tension gradient is due to thermal gradient (such as here), the Marangoni effect is referred to as Marangoni convection or thermocapillary convection[71].

As mentioned above, the relationship between the aggregate and the Brownian motion forms the negative feedback in our experimental setting. The stochastic movement of particles suspended in a fluid, in random directions is called Brownian motion[73]; Random bombardment of particles by solvent molecules is the reason behind this movement[74]. Brownian motion scale inversely with the particle size, and for particles larger than 1 μm the effect of Brownian motion significantly reduces[75]. The random motion of colloidal particles is an evidence of thermal molecular motion, which always exists including at thermal equilibrium[76].

Suppose an external force is applied to these colloidal particles as the driving force, in this case, there will be a friction or a resistive force rising from the random collisions of molecules on the particles, the results will be proportional to the velocity of particles.

Random motion of the surrounding molecules can have two effects on the particles dispersed in a liquid: *(i)* Firstly, a random driving force on Brownian particles to keep the nature of their random motion, *(ii)* to give rise to frictional forces between

liquid and the particles. These systematic (random Brownian motion) and random (frictional forces) parts must be related since they come from the same origin. Their relation is explained through fluctuation-dissipation theorem[76]. This theorem explains that there is a general relation between the response of a system to an external perturbation and internal fluctuation of the undisturbed system[76]. For example, Johnson–Nyquist noise is a thermally agitated noise generated by electrons (charge carriers) at equilibrium in an electrical conductor. When no current is applied to the system, the resistance R, thermal energy k_BT, which are the source of internal fluctuations and the bandwidth $\Delta\nu$, determine the mean square voltage[77].

More examples of applications of this theorem can be seen on spatial fluctuations of magnetization which lead to spin disorder scattering[78], Brownian motion[79], and dissipative harmonic oscillator[79].

In our system, external perturbation comes from the laser induced flows and Brownian motion of the particles is the source of internal fluctuations. According to the fluctuation-dissipation theorem, there is a relation between response of the system to laser-induced flows (formation of colloidal aggregates) and internal fluctuations of undisturbed system (Brownian motion of particles when there are no external perturbations, in other words when the laser is turned off). Based on this, the relation between Brownian motion velocity of undisturbed system and the types of formed patterns when the laser is turned on in the exact position (response of system to perturbations) on was studied.

Here, we provide an experimental study on formation of dynamic colloidal crystals far from equilibrium. We study the effect of fluid flow, thickness of the liquid film, and Brownian motion of the particles on formation of dynamic adaptive crystals and try to carefully control their formations. Since this experimental setting is uniquely capable of observing and studying dynamic adaptive colloidal crystals with a number of patterns, our findings can have significant implications for nanotechnology, crystallography, far from equilibrium dynamics, and emergent phenomena.

2.4 Patterns formation in colloidal systems

Technological applications[44,80] aside, ordered crystals formed by colloidal particles can give us valuable insights about the characteristics and behavior of

crystalline solids[81–83]. Colloidal systems have also been the subject of applied and fundamental studies[84]. This is due to larger size of colloidal particles compared to atoms, which enables researchers to manipulate and observe them under optical microscopes[85,86]. Furthermore, formation of 2D colloidal crystals with various symmetries as well as the transitions between crystalline phases and symmetries have been of great interests to researchers[87].

Since many properties of solids (mechanical, optical, magnetic, and many other properties) are closely related to their crystalline structures, crystalline structure of a solid is one of the important properties. As an example, consider various allotropes of iron. α-iron (Ferrite) has body-centered-cubic (BCC) crystalline structure thus it has ferromagnetic properties. On the other hand γ-iron (Austenite) has face centered cubic (FCC) crystalline structure, which shows non-magnetic properties[88].

Crystalline arrays of spherical colloids have many applications in photonic devices such as light polarizers and lenses[89], band gap materials[90], photonic papers[38], and colloidal lasers[37], and other applications such as masks for lithography purposes and templates for porous materials[91]. Optical properties of colloidal crystals depend on their crystalline structures and building blocks. For example, optical diffraction of a visible light beam in colloidal crystal with lattice parameter close to wavelength of visible light can result in colorful structures. Therefore by tuning the crystalline structure and changing lattice parameter various colors can be obtained which makes colloidal crystals useful for photonic applications[90].

Various methods have been used to fabricate two-dimensional arrays of colloidal crystals such as interfacial self-assembly at air-liquid interface[30], light assisted self-assembly[92], optoelectrofluidic processes[93], electrophoretic and evaporation deposition methods[90], and spin coating methods[94]. Five types of periodic crystalline lattices are possible in two dimensions, which are known as 2D Bravais lattices, namely, square, rectangle, centered rectangle, hexagonal, and oblique. Among all 2D colloidal crystals hexagonal structures are the most probable patterns since they have the highest packing ratio and minimum free energy thus thermodynamically stable[94]. Fabrication of monodispersed colloidal crystals into arbitrary 2D pattern other than hexagonal is not thermodynamically favorable, hence to from colloidal arrays with symmetries other than hexagonal lattice, particles should be guided towards their desired positions by external energy flux. Various cases of formation of quasi-2D colloidal crystals into square patterns have been reported[30,95]. For example,

N. N. Khanh *et. al.* developed a dry manual assembly process. They fabricated a template with holes designed in square pattern in size of desired colloid, and placed the colloids in desired positions by mechanical rubbing[95].

To fabricate complex colloidal patterns in quasi-2D settings, many researchers have used binary colloidal mixtures. For instance, Z. Zhaho *et. al.* used a sequential self-assembly method to fabricate binary colloidal crystals in structures of honeycomb, Kagome, and other complex lattices[96]. They first fabricated a crystalline array of polystyrene spheres (~1 μm in diameter) into hexagonal or square patterns using flow-controlled vertical deposition (FCVD) method[97], then, a layer of silica spheres (~280 nm and 400 nm in diameter) were grown on top of the polystyrene layer. The final films were heated for 5 hours in 500ºC to eliminate the polystyrene layer. As a result, complex non-close-packed structures were obtained.

Fabrication of complex Moiré patterns using colloidal microspheres has also been reported by K. Chen *et. al.* using convective self-assembly method[98]. Moiré patterns were formed of two layers of hexagonal patterns rotated on top of each other. To form the Moiré patterns, first, they fabricated a monolayer of hexagonal arrays of polystyrene microspheres (~510 nm in diameter) on a substrate. They used a container as a water reservoir and a clean substrate is dipped in the water. They dispersed colloidal suspension into the water through a tilted glass slide with one end in the container. While particles were slowly entering the water they formed a monolayer of spheres in hexagonal pattern, after the monolayer was formed they slowly drain the water container and move the monolayer onto the substrate. They repeated the same steps to deposit the second layer and left the samples to dry in ambient air. These crystals can be used as templates for lithography purposes after dry etching.

Arrangement of colloidal particles in shape of honeycomb structures were reported by L. Jiang *et.al.*; First, they created a monolayer of silica colloidal spheres (~3μm in diameter) in close-packed hexagonal arrangement as substrate, the particles were fixed in the substrate with no thermal movement. Then they built a sample cell on top the monolayer and filled it with dilute colloidal suspension of silica particles (3.4μm in diameter), the particles in the suspension sediment at the bottom layer after some time. To form honeycomb structure at the top layer, they used vector assembly method and optical tweezers. They moved the randomly dispersed silica particles in the top layer to proper positions one by one using optical tweezers to form honeycomb

arrangement of colloidal particles at the top layer[99]. This method requires great precision, and it is a very slow method since particles should be moved one by one.

Formation of quasicrystals have also been reported in colloidal crystals[100,101]. Quasicrystals lack translational symmetries[102], They have unique properties such as low thermal conductivity, strong anisotropy in electronic transport, which are closely related to their aperiodic structures[102]. Quasicrystals were first observed in intermetallic alloys[103], later 2D monolayer of colloidal quasicrystals arrays were reported[100,104]. Y. Roichman and D. G. Grier reported self-assembly of colloidal silica microspheres (~1.53μm in diameter) into quasicrystals. They used a method based on holographic optical trapping in which a 3D array of optical traps is created by computer generated holograms. Silica colloidal particles were dispersed in an aqueous solution (180:12:1 (wt/wt) acrylamide, N,N'- methylenebisacrylamide and diethoxyacetophenone). The solution was poured into a 30μm thick sample slit on a microscopic glass slide and sealed carefully. Since the silica particles are denser than water, they sediment into a monolayer. As the holographic optical tweezers were applied to a dilute layer of silica particles, they arranged into various 2D quasicrystals shapes depending on the applied holograms[104].

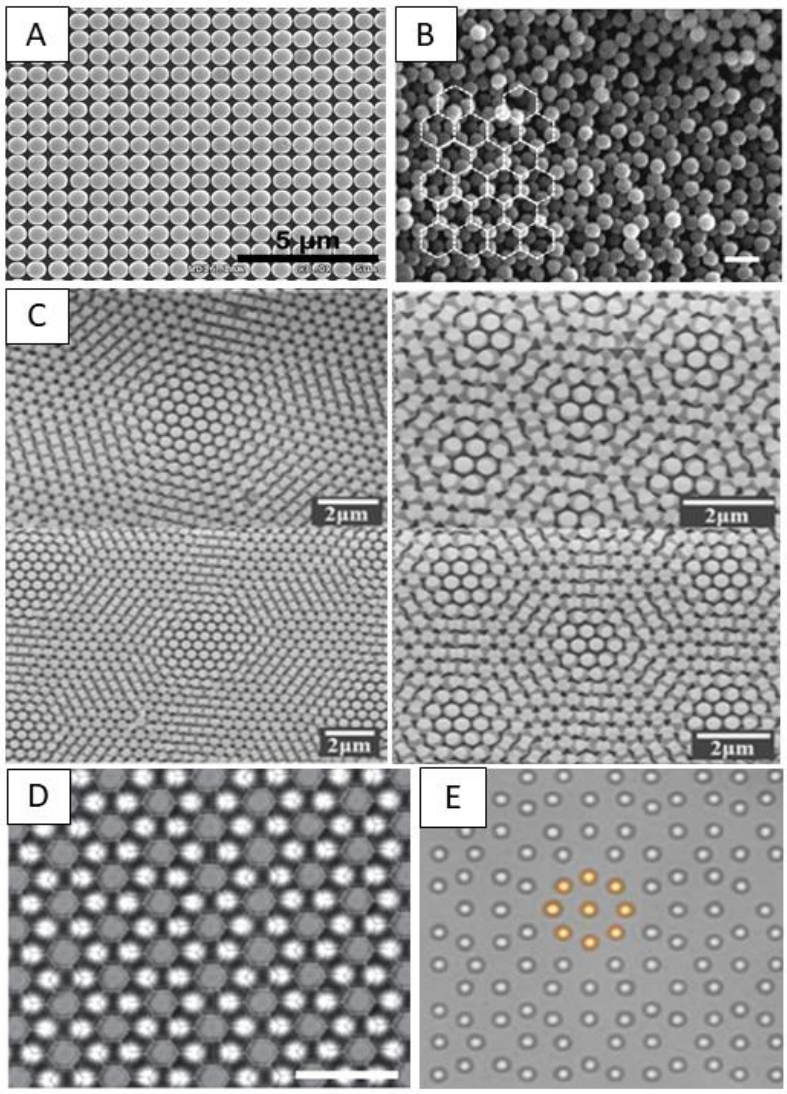

Figure 2-8 Colloidal patterns fabricated through various methods; A) SEM image of 700-nm silica beads organized into perfect square patterns through rubbing particles on a patterned substrate, the particles are positioned on nanowells fabricated on the substrate[95]; B) SEM image of honeycomb arrangements in binary colloidal crystals (size ratio of particles: 0.4) made of silica particles after process of calcination[96]; C) SEM images of a series of Moiré patterns fabricated through dry etching two layers of hexagonal arrays of colloids rotated on top of each other for lithography purposes[98]; D) Arrangement of colloidal particles into honeycomb structure using vector assembly method directed by optical tweezers (scale bar is ~10µm)[99]; E) Two dimensional colloidal crystal formed using holographic optical traps[104]. [Reprinted with permission from: (A) Ref [95]; (B) Ref[105]; (C) Ref[98]; (D) Ref[99]; (E) Ref[104].]

In this thesis, we report formation of colloidal crystals into all the 2D Bravais lattices, honeycomb lattices, Moiré patterns and quasicrystals. We use monodispersed

pure polystyrene spheres (500 nm in diameter) as building blocks. Formation of rich variety of patterns in our system is possible thanks to highly nonlinear and strongly stochastic far from equilibrium conditions[4,12,13]. Unlike the aforementioned studies, our methodology is simple and does not require any prior modifications such as fabrication of templates for growing colloidal crystals. Most importantly, the colloidal crystals formed in this system are dynamic and adaptive. A structure is called adaptive when it can modify itself in response to perturbations and fluctuations in environment to be better fit. Dynamic structures exist at a distance from equilibrium where they continuously sustain themselves by a flux of energy and change from one structure to another.

The possibility of studying such crystals can contribute to studies on emergent phenomena far from equilibrium, adaptive dynamic systems, complex systems, and model studies for atomic world.

The system used in this thesis provides the opportunity of recording and observing the behavior of system far from equilibrium. We can add external stimuli to the system within short timescales (few seconds) by changing laser position or bubble configurations, and observe the response of the system within seconds. Colloidal crystals obtained in this system can be used to study early stages of crystallizations, nucleation and growth, phase transitions, and formation of defects. Using colloidal particles with their superficial similarities to atoms makes the results of this research valuable for studies of the atomic world and will give deep insight about similar systems with various length and timescales.

Chapter 3

Methods

3.1 Materials

Colloidal solution of pure polystyrene particles (497±7 nm in diameter, standard deviation of 0.013μm) was purchased from Microparticles GmbH. The colloidal solution contains 0.07%wt SDS surfactant (Sodium dodecyl sulfate) as stabilizing agent, to keep particles from clustering, and 0.007%wt NaN_3 preservative. ~150 μm thick optically transparent glass slides were purchased from ISOLAB (Isolab Laborgeräte GmbH).

3.2 Experimental setup

The experiments were conducted in an inverted microscope system (Nikon, Eclipse Ti-U) where an ultrafast laser (Spectra Physics, Spirit One 1040-8-SHG) is integrated. Central wavelength of the laser was 1,040 nm, with repetition rate of 1 MHz, and a spot size of ~8 μm in diameter ($1/e^2$). Laser was guided to the specimen through an optical path shown in Figure 3-1. The sample is placed on a high-speed motorized 2D transverse scanning stage (Thorlabs MLS203-1), with a minimum step size of ~100 nm, that enables precise movement of the sample.

A short pass filter blocks the IR laser beam passed through the sample and the rest is guided to CMOS camera. A fast scientific-CMOS camera (QImaging. OptiMOS sCMOS), is used for live imaging and recording the experimental videos. Experimental videos of patterns formation are recorded with minimum frame rate of

10 fps. To record Brownian motion of particles for video processing purposes high speed camera (Fastec IL5-s) with 300 frames per second is used.

A blue light source is used to illuminate the specimen, choice of blue color is made to minimize the diffraction of light and obtain a clear image. After passing through the sample, both illumination light and the laser are sent through a magnification objective (CFI Plan Fluor ADH 100 × Oil).

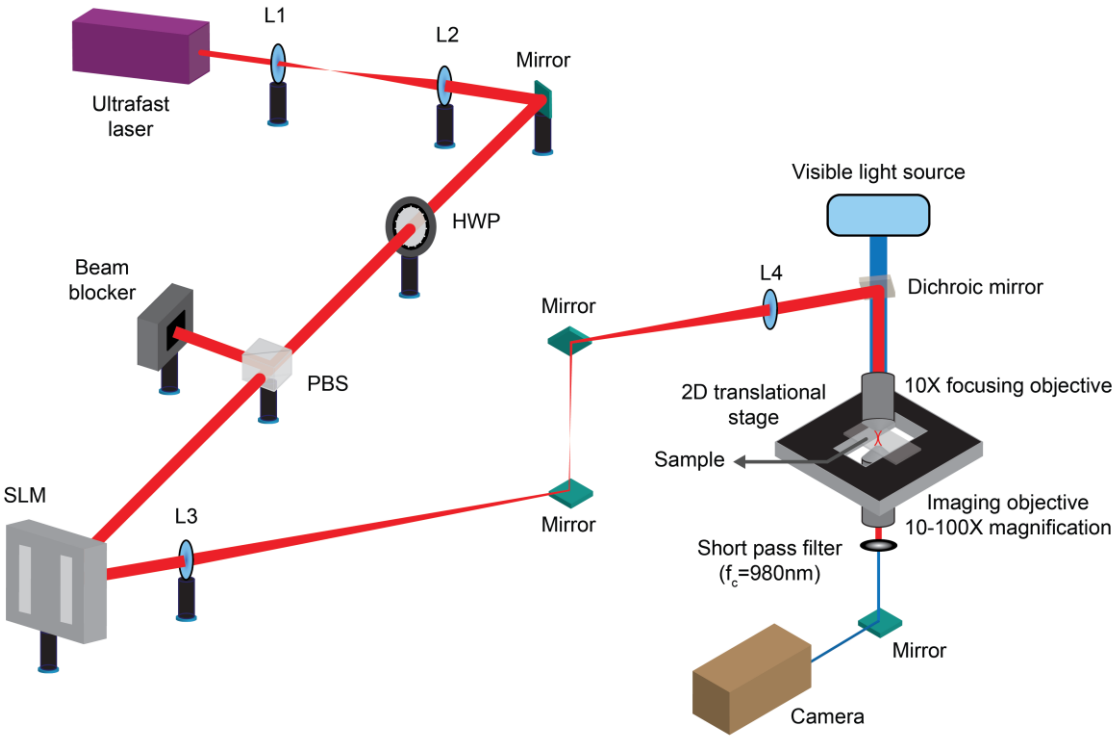

Figure 3-1 Schematic illustration of the experimental setup; An ultrafast laser beam is directed through an optical path to shine on the sample through an inverted microscope, which is connected to a camera for imaging. (Abbreviations: L: Lenses; HWP: Half-Wave Plate (the power controller); PBS: Polarizing Beam Splitter; SLM: Spatial Light Modulator).

3.3 Sample preparation

1µl* of 500 nm mono-dispersed polystyrene colloidal solution is sandwiched between a pair of optically transparent glass slides of ~150 µm thickness. Edges of the

* Axygen micropipette (0.5-10µl) was used, with accuracy of ±4%, and precision of 2.8%.

samples were carefully sealed to prevent any pressure differences in sample as well as keeping the sample from drying out easily due to evaporation. Figure 3-2 shows the steps of sample preparation.

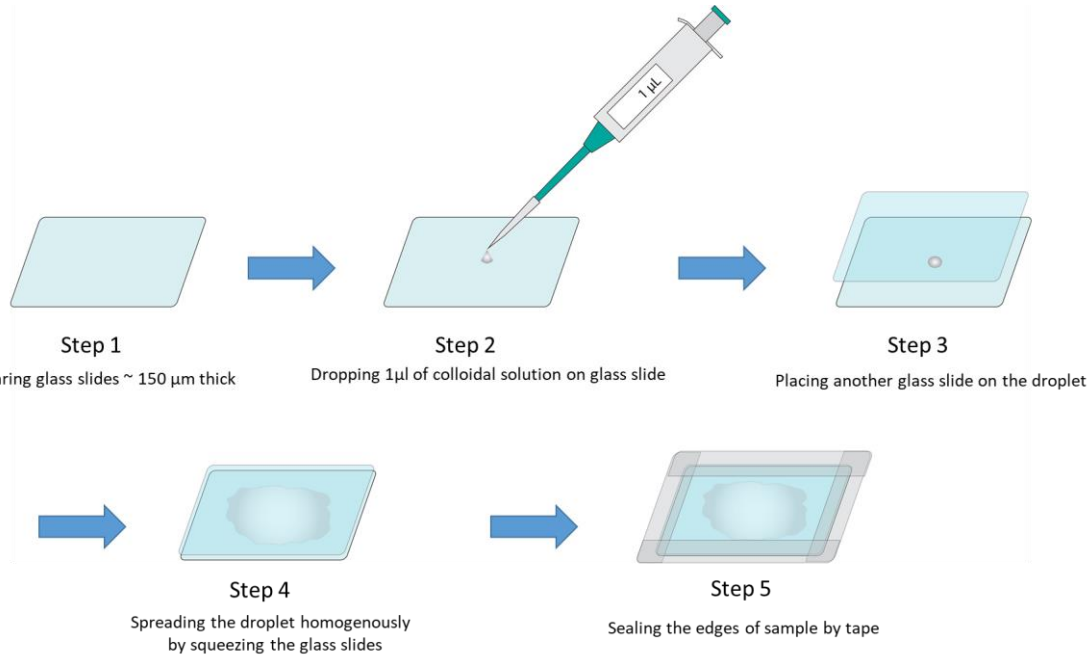

Figure 3-2 Sample preparation steps; 1µl of colloidal solution was sandwiched between two thin glass slides to form a thin layer of colloidal solution, edges of the sample were sealed carefully in order to keep the sample from drying out and prevent any pressure difference throughout the sample.

3.4 Formation of the aggregates and various crystals

First step is to place the sample on the sample holder and to fix it. To create colloidal aggregates, first, we create a gas bubble, either by using the "bubbleator" button on, or by increasing laser power slowly on the laser interface software. "Bubbleator" button is designed to create bubbles in a more controllable fashion[4], it would instantly increase the laser power for short amount of time to boil the water, then rapidly decrease to prevent further growth of the bubble. We can adjust the laser power to enlarge or shrink the bubbles upon forming a bubble, to enlarge a bubble laser power should be increased which heats the gas inside the bubble and increases pressure therefore the size of bubble increases. Upon turning laser off bubble would shrink due to asymmetric heat flow. If the pressure inside the bubble is same as the pressure of fluid or more it will be stable and wouldn't shrink by turning the laser off.

Next step is to position the beam inside the bubble and increase the power. Laser will create well controlled spatiotemporal thermal gradient which would cause Marangoni flows that drag that particles toward laser spot.

Various parameters can affect formation of colloidal crystals in our system such as: total volume of solution, concentration of particles in solution, size of particles, thickness of liquid film, laser parameters (power, wavelength, repetition rate, beam diameter), physical boundaries, and laser induced flows. Total volume of solution, concentration of particles in solution, size of particles, and laser parameters (except laser power) is fixed. Laser power is changed and modified between 0 to 50 mw to form and stabilize a bubble, then it is fixed to a value between 10-20 mw to form the aggregate. The values of effective parameters are listed in the following table:

Table 3-1 Parameters affecting on formation of colloidal aggregates and their values.

Volume of solution	**Concentration of particles in solution**	**Size of particles**	**Thickness of liquid film**	**Laser power**	**Laser wavelength**	**Laser repetition rate**	**Beam diameter**
1 µl	2 %wt/wt	~497±7nm	~ 0.5-1.5µm	~ 0-50mw	1024 nm	1 MHz	~ 8µm

The effect of physical boundaries and fluid flow is investigated through COMSOL simulations.

3.5 Fourier transform analysis of the colloidal crystal

A Fourier transform analysis is applied to raw images of formed colloidal crystals, recorded by video microscopy. Fourier transform provided us with the reciprocal lattices of the crystals, crystalline structure of aggregates can be identified by their reciprocal lattices[4,106]. A Fast Fourier Transform (FFT) algorithm is used to calculate discrete fourier transform of an image using FFT function in Matlab (version 2018b). The Matlab code is provided in supplementary material[*]. Images used for

[*] Courtesy of the Matlab algorithm goes to Dr. Ghaith Makey.

fourier transform analysis are selected from large aggregates with various geometries, the images should be cropped in 1:1 aspect ratio.

3.6 Fluid dynamics simulations

To simulate fluid flow in two dimensions, the commercial finite element simulation software COMSOL Multiphysics (version 5.0) is used*. To model the pressure and velocity fields, the Navier-Stokes equations for steady state incompressible Newtonian fluid should be solved[4]. Changes in temperature of fluid would affect the velocity field and create a buoyancy force. Bouyancy force is the net force applied to an object in any fluid. This force must be presented in Navier-Stokes equations, and we must somehow relate it to temperature of fluid. The Boussinesq approximation is used to represent the buoyancy term in Navier-Stokes equations. Boussinesq approximation is an approximation which is used to make calculations simpler, by stating that density variations are neglected everywhere except in buoyancy term[107].

$$\rho\,(u\,.\nabla)\,u = \nabla.[-pI + \mu(\nabla u + (\nabla u)^T)] + F \qquad (3\text{-}1)$$

$$\nabla.(u) = 0 \qquad (3\text{-}2)$$

$$\nabla.\left(-k\nabla T + C_p\rho T u\right) = 0 \qquad (3\text{-}3)$$

Where u, μ, ρ, β, T, k, C_p, I and F are convection velocity, viscosity, density of fluid, thermal expansion coefficient, temperature, heat conduction coefficient, specific heat, Identity matrix and external forces, respectively. Equation 3-1 is the Navier-Stokes momentum balance equation which is the result of second law of Newton applied to a bulk fluid particle. Equation 3-2 is the continuity equation at steady state, continuity equation is another form of conservation laws, which shows transport of a quantity. Equation 3-3 is the heat balance equation. Here the F parameter in equation 3-1 is gravitational force or buoyancy forces.

* Simulations were originally done by Dr. Gursoy B. Akguc.

$$F = \rho g \tag{3-4}$$

As mentioned above we used Boussinesq approximation[108] to make the calculations simpler.

$$\Delta\rho = \rho - \rho_0 \tag{3-5}$$

$$\rho = \Delta\rho + \rho_0 \tag{3-6}$$

$$\Delta\rho g = (\rho - \rho_0)g = -\rho_0\beta(T - T_0)g \tag{3-7}$$

To avoid potential round-off errors in the calculation of the buoyancy term, $(\Delta\rho + \rho_0)g$, the pressure and buoyancy terms on the right-hand side of the Navier-Stokes equations $\nabla p + (\Delta\rho + \rho_0)g$ is written as $\nabla P + (\Delta\rho + \rho_0)g$ where P is defined as $P = p + \rho_0 gh$.

After all the equation of momentum yields as:

$$-\nabla\mu(\nabla u + (\nabla u)^T) + \rho(u.\nabla)u + \nabla P = -\rho_0\beta(T - T_0)g \tag{3-8}$$

Numerical simulations were conducted in COMSOL for a computational area of 1cm by 1cm. Physical boundaries (bubbles) with various shapes observed in experiments were replicated in simulations. With laminar flow interface in COMSOL we solved the momentum balance equations and with heat transfer in fluids interface we solved heat transfer equation. Figure 3-3 shows a computational area replicated in COMSOL.

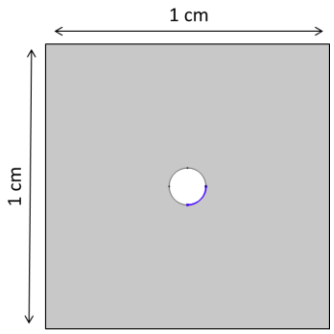

Figure 3-3 Computational area in COMSOL, the blue line on the spherical bubble indicates the boundary heat source, size of the bubble is considered as 50μm in diameter.

Laser is introduced as a boundary heat source in a quarter of the bubble boundaries to break the symmetries and form fluid flows. Temperature difference between laser spot and the rest of the sample is set at 2ºC, which is optimum for this case[4].

We simulated fluid velocity field and pressure field for the representative bubble types observed in the system. The observed bubbles can be categorized into 5 different configurations namely: *(i)* spherical bubbles, *(ii)* elliptical bubbles, *(iii)* flat bubbles, *(iv)* V-shaped bubbles, and *(v)* a spherical bubble on flat bubble, Figure 3-4 shows the various bubble shapes observed.

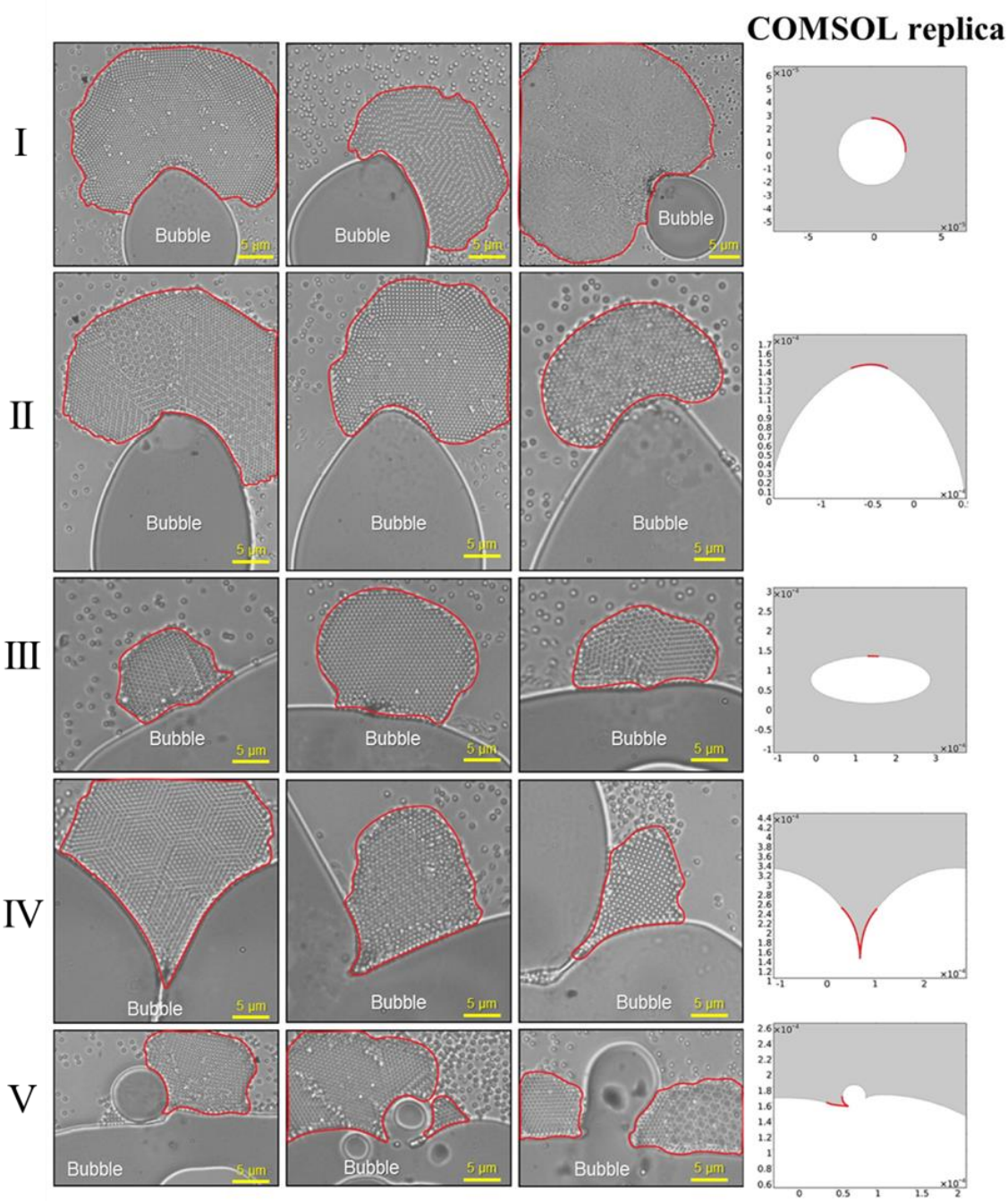

Figure 3-4 The bubble shapes formed in system and their respective COMSOL replica; I) Spherical bubbles; II) Elliptical bubbles; III) Flat bubbles; IV) V-shaped bubbles; V) a spherical bubble on flat bubble; Red lines in COMSOL replicas represent the position of laser.

3.7 Data analysis of Brownian motion and liquid film thickness measurements

Velocity of the Brownian motion of particles depends on the temperature of fluid, concentration, size and confinement of particles. To perform analysis on Brownian motion the concentration of particles and the temperature are kept constant for all samples. However, thickness of liquid film can slightly change form one sample to another or in different spatial positions within one sample. The reason is that the glass slides used for sample preparation are not completely flat, and their surfaces has peaks and bottoms. The profilometry analysis on 5 glass slides along a 7mm line showed on average the maximum height difference between peaks and bottoms is ~200nm while local surface roughness is ~2nm. This means although the surfaces of glass slides are not completely flat and can cause thickness difference throughout the sample, locally we can consider them as flat. Therefore, in same spatial positions on sample thickness is unified while within longer ranges in can differ. To prepare a sample two glass slides are positioned on top of each other which can create ~400nm thickness difference between various spatial positions. Another factor effective in thickness of liquid film is sample preparation. If the colloidal solution is not perfectly spread between glass slides it can create differences in liquid film thickness form one spatial position to another.

Change in thickness of liquid film can change the average velocity of Brownian motion from one spatial position to the other spatial position when the laser is off. This is the reason why average Brownian motion velocity in each spatial position should be measured prior to formation of patterns.

In our samples the particles are doing Brownian motion in a confined area (confined in Z direction), it is well known and generally agreed that if the particles are undergoing Brownian motion near a fully wetted solid liquid boundary (no-slip boundary condition) mobility of particle is lower and diffusion of particle is slower compared to the particles in the bulk[109]. This is called surface confinement, firstly introduced by Lorentz 1907[110]. The diffusion coefficient for Brownian diffusion in bulk is predicted by Einstein-Stokes relation:

$$D_b = \frac{kT}{4\pi\eta R} \qquad (4\text{-}1)$$

In this equation D_b is diffusion coefficient of particles in bulk, kT is thermal energy, η is viscosity of liquid, and R is the hydrodynamic radius of the particle. Viscosity is a measure of fluid's internal flow resistance; thickness of liquid film can modify how easily the fluid flows.

For particles close to solid liquid boundary (wall), Lorentz predicted a reduced diffusion coefficient[111]:

$$D_w = D_b(1 - \frac{9R}{16h}) \qquad (4\text{-}2)$$

Here D_w is diffusion coefficient of particles near wall, h is the distance between center of particle and the wall. Equation 4-2 shows as the distance between particle and wall increases, the diffusion coefficient increases. As diffusion coefficient increases and mean square displacement also increases ($< x^2 >= Dt$) which means average velocity of Brownian motion in system should increase as the distance between wall and particles increases.

To investigate the effect of Brownian motion velocity as the source of internal fluctuations in the system, 15 specimens of ~500 nm polystyrene colloidal solution were prepared. Specimens were prepared as explained in Sample preparation (section 3.3).

For each trial following steps were followed:

1. While laser beam is blocked by shutter, approximately 1-minute video of particles doing random Brownian motion was recorded using high speed camera (Fastec IL5-s) with 300 frames per second and 100X oil immersed objective. High frame rate videos are necessary for accurate calculation of Brownian motion velocity in video processing step.
2. In the same spatial position, colloidal aggregates were obtained by unblocking the laser beam and creating a bubble. Formation of patterns was recorded in this step using fast CMOS camera (10 fps).
3. Moving in the nearby area (within ~100μm range) the second step was repeated 2 more times.

In each specimen, the aforementioned steps were taken for 3 trials in various spatial positions. To move from one spatial position to another, we moved for minimum of 5000μms. Figure 3-5 demonstrates steps of this experiment.

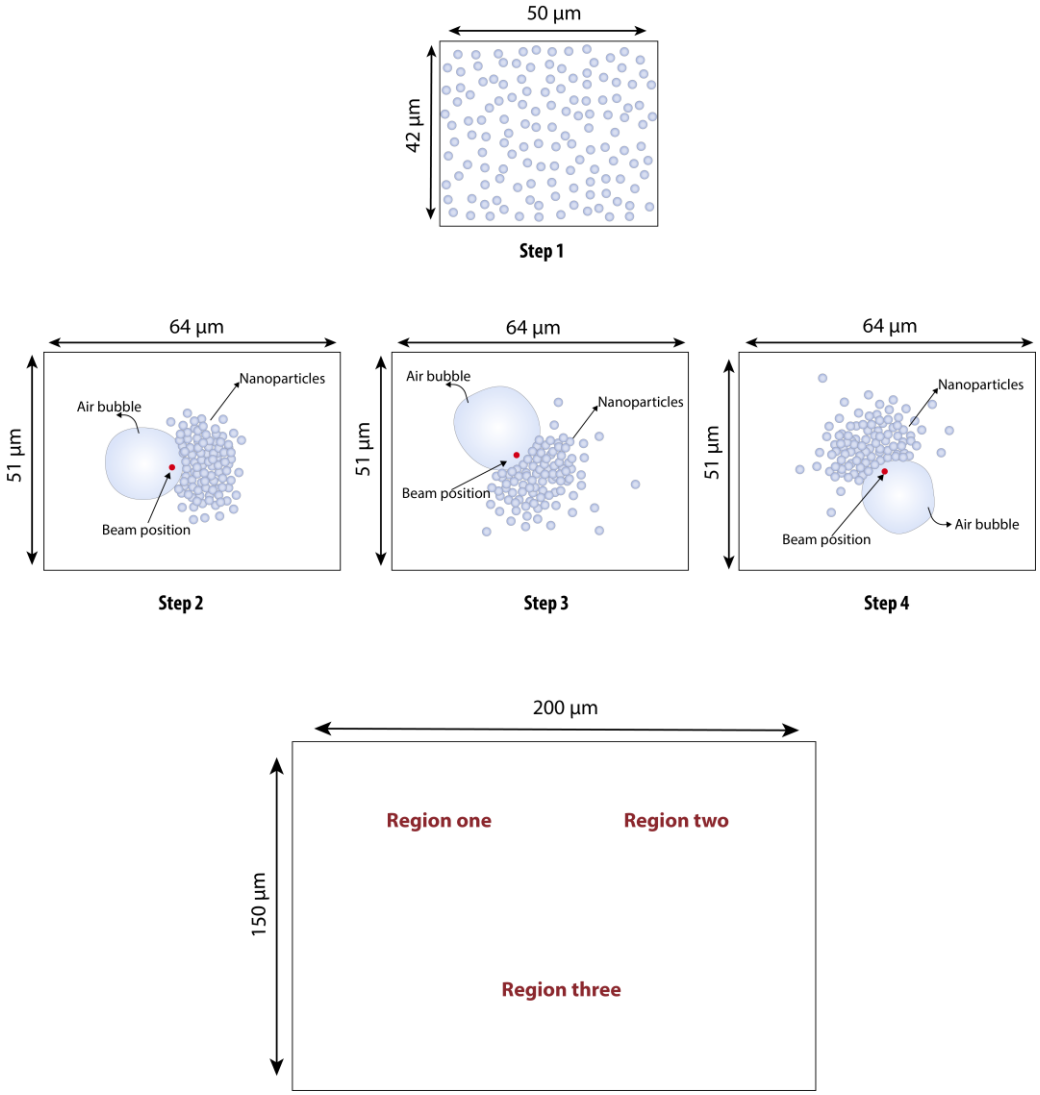

Figure 3-5 Steps of Brownian motion experiments explained above: Step 1) Find an area without directionality and record 1 minute video of particles doing random Brownian motion with fast camera (field of view: 42*50µm, and frame rate of 300 fps); Step 2) Form an aggregate in the same area (region one) and record the crystalline structure; Step 3) Move about ~60µm (region two) and form and aggregate and record the crystalline structure.; Step 4) Move about ~60µm in another direction (region three) and repeat step 3. Position of the regions with respect to each other is shown on the bottom of this picture.

The videos recorded in first step were processed to calculate average velocity of Brownian motion, the videos recorded in second and third steps were used to document the types of patterns observed in that spatial position. Figure 3-6 summarizes the whole process. In total 15 samples were prepared, and 43 videos were recorded from them.

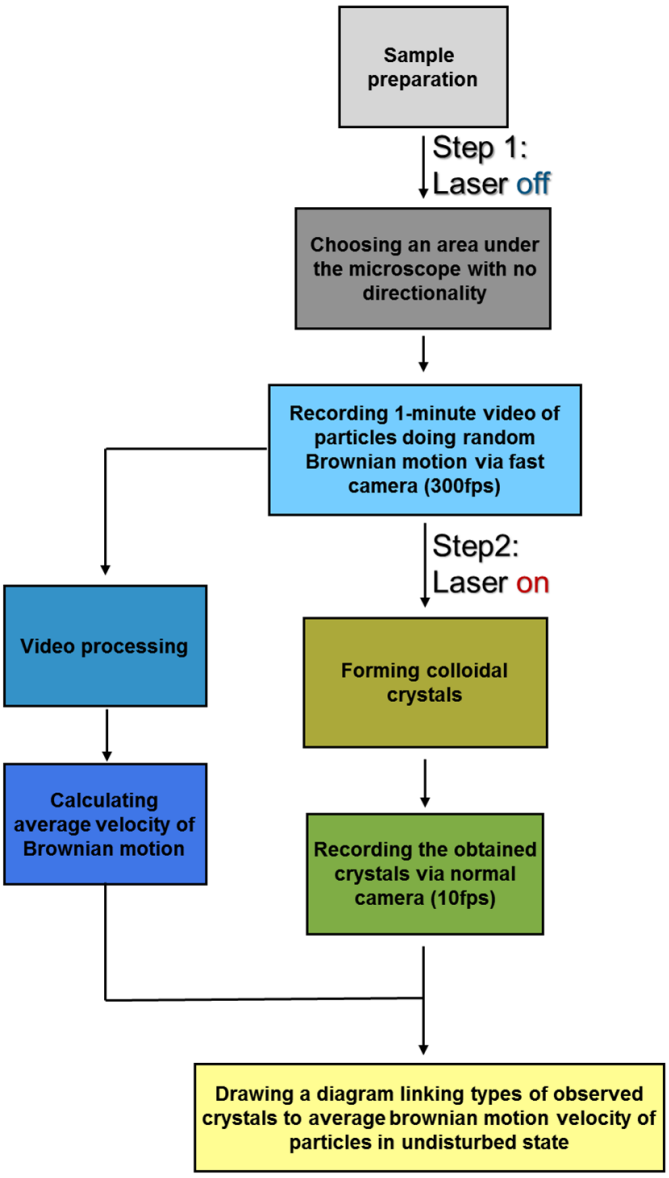

Figure 3-6 The steps taken to obtain average Brownian motion velocity for each pattern; starting with sample preparation, then finding an area under the microscope which shows no directionality (particles are doing random Brownian motion without moving toward any specific direction) and recording 1-minute video of particles doing random Brownian motion when laser is blocked, with fast camera (300fps). Next step is to create colloidal crystals in the same area and document the observed patterns. Lastly, we perform video processing on the 1-minute Brownian motion video to obtain average Brownian velocity corresponding to the observed patterns.

3.8 Video processing for calculation of average Brownian motion velocity of the particles

Videos of colloids doing random Brownian motion were processed using a MATLAB algorithm[*]. The video processing algorithm has four main step which are shown in Figure 3-7: First, it reads the videos frame by frame (Figure 3-7-I); Second, it adjusts the pre-processing parameters (color, contrast, sharpness, etc.) on each frame so that the algorithm can detect the particles more easily (Figure 3-7-II); Third, Circle Hough Transform[112] is used to detect the position of particles in the particle detection step (Figure 3-7-III). Circle Hough Transform is a method to detect circles in imperfect images which are the frames of our videos here. Last, after detecting the positions of the particles over the video. The motion track of each particle is calculated using Hungarian method[113]. Hungarian method is a particle tracking method used to track moving objects by detecting the objects frame by frame. The motion track shows the x-y coordinates of each particle as functions of time (Figure 3-7-IV).

Using those coordinates, we calculated the displacement of each particle and then the average velocity of them. We further average the velocity of all the particles to get a single value that shows the mean velocity of the Brownian motion in the video. The calculations are done in videos are 1 minute in length (~18,000 frames).

For the algorithm to work perfectly, we need to have videos in which all the particles are seen white. If the thickness of liquid is high, particles move in depth (z-axis) and change their focus[114], therefore the algorithm confuses and cannot link the position of particles between frames to draw the motion tracks. Here we have to prepare samples in which liquid film thickness is low (~0.5-1 μm in thickness) so that movement of particles in depth would not change the color on them significantly, and this limits the experiments only to thin samples.

[*] Courtesy of the Matlab algorithm goes to Dr. Ghaith Makey.

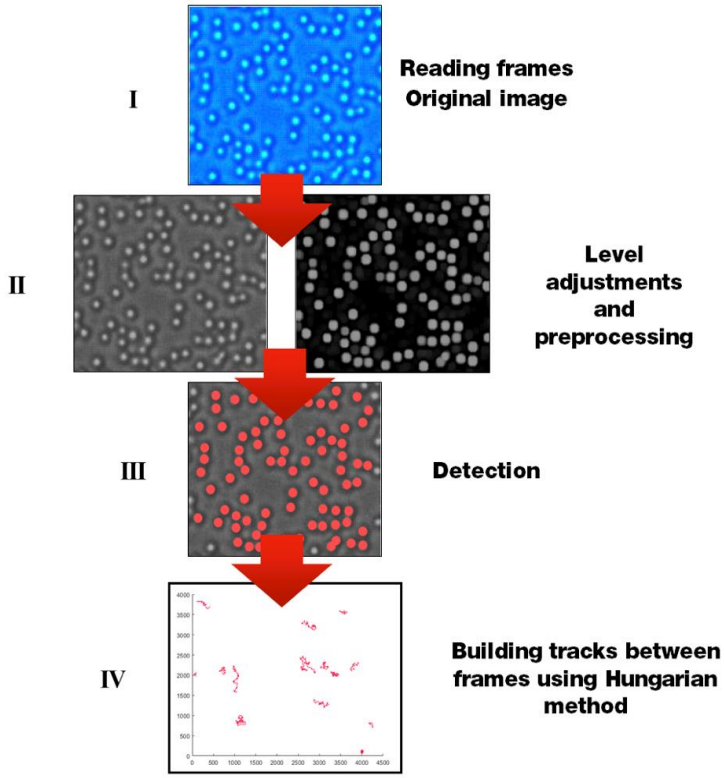

Figure 3-7 Steps of video processing algorithm, I) starting with reading the videos frame by frame; II) Next step is to adjust levels and perform some preprocessing steps; III) Detection of particles for each frame; IV) Linking the detected particles in each frame to other frames to draw the trajectories.

3.9 Formation of patterns in same spatial position

Environmental factors of the system such as thickness of the liquid film, concentration of particles, and temperature of the liquid can affect formation of patterns. Thickness of the liquid film creates some constraints on pattern formation, such that some patterns are geometrically impossible in low thicknesses, this has been discussed in details in section 4.7. Temperature of liquid and concentration of particles have effect on Brownian motion of particles, as temperature increases, Brownian motion speeds up therefore fluctuations increases. As concentration of particles increases interparticle collisions increases and Brownian motion slows down which can influence pattern formation. To investigate which patterns can coexist in the same environmental factors, aggregates were formed in one spatial region repeatedly for 9 times, that the environmental factors be the same and patterns were recorded. Three

specimens were prepared as explained in section 3.3. After the specimen was placed under the microscope and laser beam was focused on sample, colloidal aggregates were obtained within the same spatial position (within a 350µm*350µm area) for 9 trials. Various focuses under microscope indicate that light is focused in different heights[114]. Moving from one focus to another required changing the height which is possible by using automated z-stage (Thorlabs 1-Channel 150 V Benchtop Piezo Controller).

We simply measure the thickness of the multi-layered aggregations using the automated z-stage model number. We do that by moving the stage to get the objective focus plane at the highest layer of the aggregation (Figure 3-8 a) then we move the stage to get the focus plane at the lowest layer (Figure 3-8 b). The z value at each of those layers is obtained from the z-stage digital reading (resolution at 25 nm) and then the thickness of the aggregation is estimated. This accuracy of this method depends on the diffraction limit of the imaging system, which was calculated to be ~200nm.

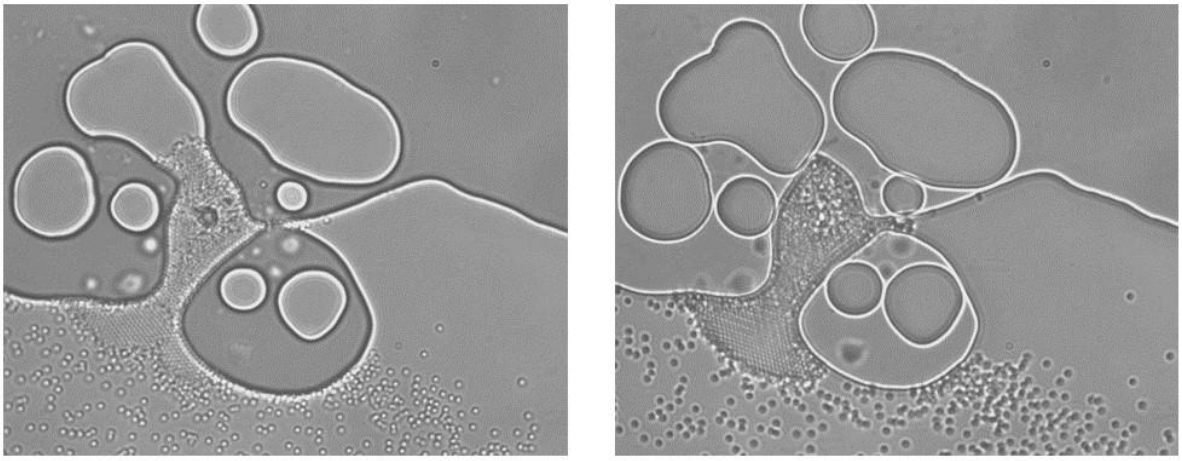

Figure 3-8 Thickness measurements focuses, Focus a: all particles are light meaning light is focused on top of the particles, Focus b: All particles are dark meaning light is focused on bottom of all particles[114]. If in one focus some particles are viewed as dark and some as light it means that the particles are at different heights (z-values).

Chapter 4

Results and discussion

In this chapter, first all observed crystalline structures namely, 2D Bravais lattices, Moiré patterns, honeycomb patterns, and quasicrystals are reviewed. Then, emergent properties and characteristics of these patterns such as adaptability, competition, dynamic behavior, and self-healing are discussed. Finally, the effects of different parameters such as thickness of liquid film, fluid flow and boundary shapes, and Brownian motion velocity of particles on formation of patterns are discussed.

4.1 Two-dimensional Bravais lattices

Two-dimensional Bravais lattices are formed by arrays of discrete points which are generated by translational operations in 2D space, described by:

$$R = n_1 a_1 + n_2 a_2 \qquad (4\text{-}1)$$

where n_i are any integers and a_i are primitive vectors that span the lattice.

There are 5 types of Bravais lattices in 2D, namely, square, rectangle, centered rectangle, hexagonal and oblique.

Figure 4-1 shows experimental bright field microscopy images chosen from more than 6000 minutes of videos recorded from more than 50 samples. We show all 2D Bravais lattices formed from simple polystyrene spheres that are interacting through hydrodynamic and hard-sphere interactions. To confirm these lattices, we have performed Fast Fourier Transform (FFT) analysis on the raw experimental images using the algorithm explained in section 3.5. We observed hexagonal lattices formed both when the aggregates are one layer thick or when the aggregates have more

than one layer. However, all other 2D Bravais lattices (square, rectangle, centered rectangle and oblique) were only observed in our experiments when the aggregates were more than one layer thick, therefore they are quasi 2D aggregates.

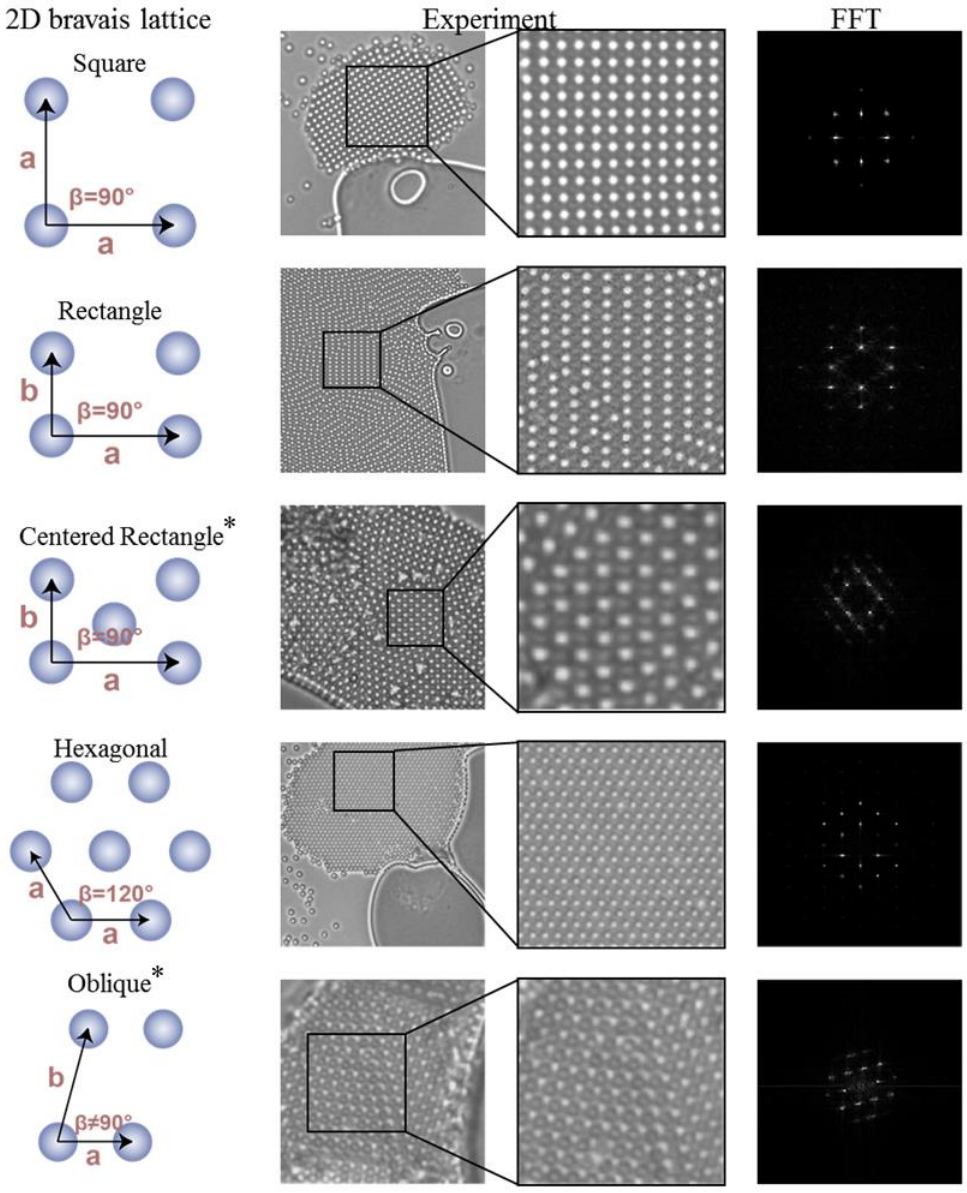

Figure 4-1 Microscope images show all 2D Bravais lattices of colloids formed in our experiments. Except hexagonal patterns that can be formed in one layer, all the other patterns are formed of at least two layers of particles therefore they are quasi 2D patterns. Centered rectangular patterns and oblique patterns were rarely observed.

Among all the observed 2D Bravais lattices observed in our experiments, centered rectangular patterns and oblique pattern were rarely observed, therefore there is no statistical evidence obtained from these structures.

At thermal equilibrium, only one configuration has the minimum free energy for spheres, which is hexagonal lattice[94], yet when the system is driven far from equilibrium, the probability of it to gain access to multiple steady states increases significantly because of highly nonlinear and strongly stochastic conditions[4]. When far from equilibrium, linear stability of system is lost since system cannot be described by linear equations, and system has nonlinearity. Nonlinearity and far-from-equilibrium conditions make it possible for the system to develop diverse structures and transfer from one state to another states through noise induced transitions[4,115].

4.2 Moiré patterns

Another set of structures that we observed in our experiments are Moiré patterns. Moiré patterns are formed when two lattices overlap with a misorientation angle with fixed centers as shown in Figure 4-2[116].

We reproduced these patterns in computer. Two layers of hexagonal arrays were drawn in Adobe illustrator 2018 software, one layer was rotated on top of the other layer, when centers of two layers were fixed. By changing the rotation angles, different shapes of Moiré patterns can be formed.

In our experiments we observed Moiré superstructures based on overlapping of 2 layers of hexagonal lattices. Based on the rotation angle we can see five various types of Moiré structures in our system (β angle is shown in Figure 4-2).

.

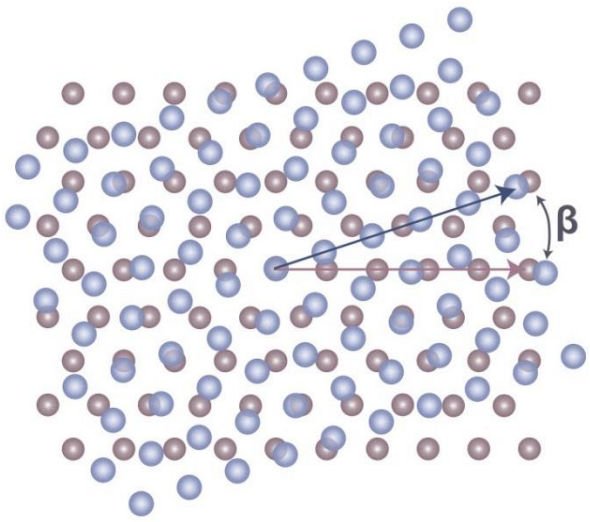

Figure 4-2 Illustration of Moiré patterns made of two layers of hexagonal lattices rotated on top of each other when centers are fixed with misorientation angle β.

Figure 4-3 shows bright field microscopy images of experimentally observed Moiré patterns, their computer generated replicas and Fast Fourier Transform (FFT) analysis of each pattern. We performed FFT on the raw experimental images and compared the results with FFT of computer generated replicas of the patterns (drawn in Adobe illustrator 2018) to identify the misorientation angle. Mainly, 5 various types of Moiré patterns were observed in our system, namely Moiré patterns with rotation angles of ~ 6.5°, 10.5°, 14.5°, 18°, and 20.5°. These patterns exhibit translational periodicity, meaning position of particles repeats in space regularly.

To observe these structures two layers of hexagonal patterns should be rotated on top of each other. Rotation of layers is possible if a thin layer of fluid is passing between the layers, therefore fluid flow plays an important role in formation of these patterns.

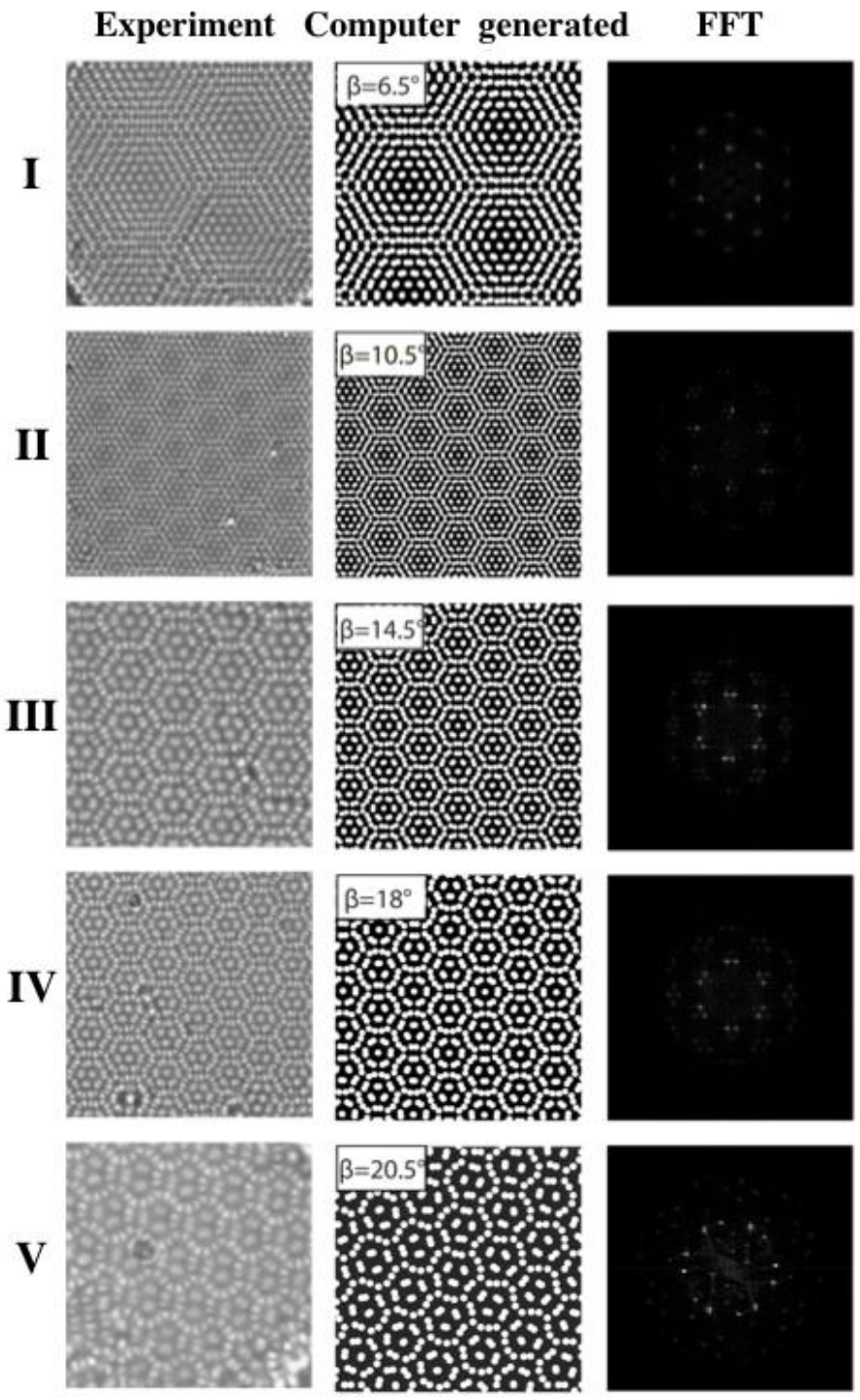

Figure 4-3 Various types of Moiré patterns can be observed depending on their misorientation angles, their computer generated replicas (drawn in Adobe illustrator 2018), and FFT pattern of experimentally obtained patterns.

4.3 Honeycomb patterns

Honeycomb patterns are observed when two layers of hexagonal lattices overlap and one of them is shifted on top of the other one (Figure 4-4). To produce computer generated honeycomb patterns, we used Adobe illustrator 2018 software to draw two layers of hexagonal patterns similar to what we did for Moiré pattern. This time we shifted one layer on top of the other layer along shifting vector *R* as demonstrated in Figure 4-4.

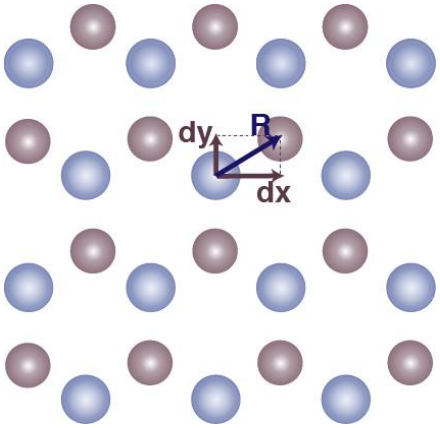

Figure 4-4 Illustration of Honeycomb patterns made of two layers of hexagonal lattices shifted on top of each other. *R* is the shifting vector, where *dx* the x component of *R* direction and *dy* is the y component of *R*.

Depending on direction and size of shifting vector *R*, with x and y component of *dx* and *dy*, we reproduced 3 various types of experimentally observed honeycomb patterns in computer. Bright field microscopy images of the experimentally observed honeycomb patterns, their computer generated replica and Fast Fourier Transform (FFT) of each pattern is shown in Figure 4-5. FFT of these structures are similar to hexagonal lattices.

These structures are formed when two layers of hexagonal lattices are shifted on top of each other. Shifting of two layers of patterns is possible if a thin layer of liquid is passing between the layers and moves one layer slightly. Therefore, similar to Moiré patterns fluid flow can have an important role in formation of honeycomb patterns.

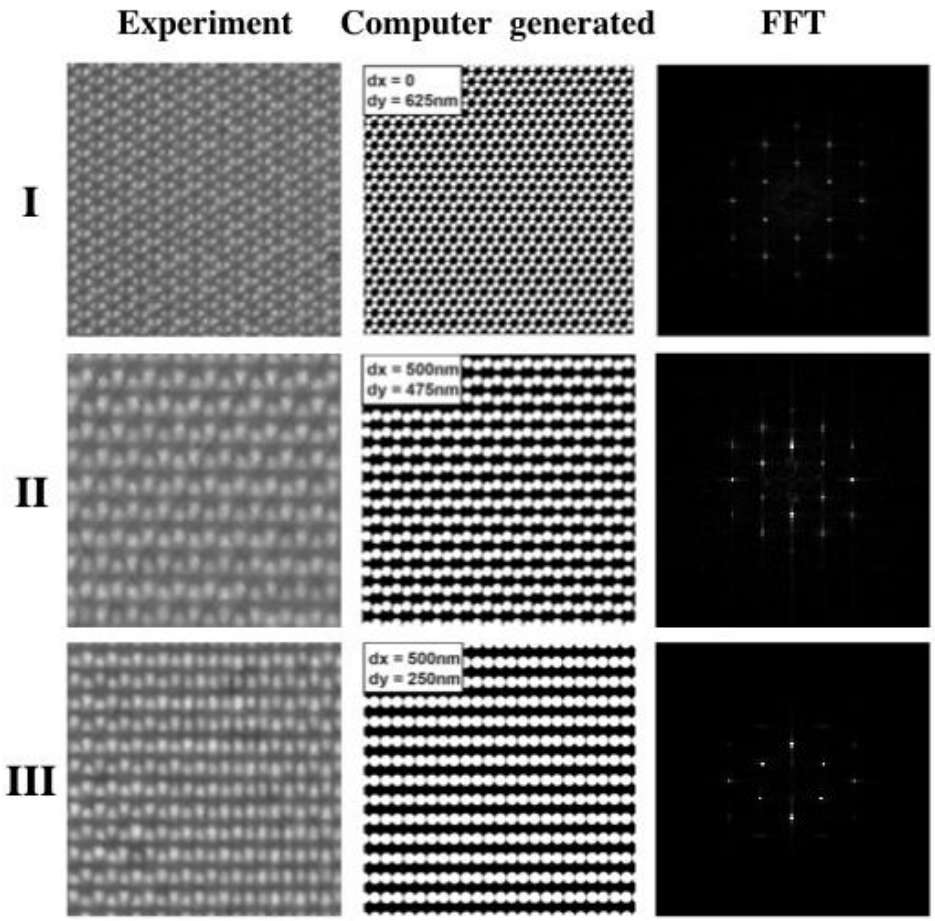

Figure 4-5 Bright field microscope images, computer generated lattices and FFTs of experimental honeycomb lattices. Depending on the shifting ratio, various types of Honeycomb patterns can be observed in the system.

4.4 Quasicrystals

Quasicrystals are aperiodic patterns that can continuously fill the space, they show long-range orientational order and quasiperiodic translational order[117]. In the literature there are various types of quasicrystals based on their rotational symmetries, such as 5-fold[118], 8-fold[119], 10-fold[101], and 12-fold[116,120]. We observed quasicrystals formed of two monolayers of hexagonal lattices with misorientation angle close to 30 degrees as demonstrated in Figure 4-6 which have 12-fold (dodecagonal) symmetries.

To produce computer generated honeycomb patterns, we used Adobe illustrator 2018 software to draw two monolayers of hexagonal patterns similar to Moiré patterns. One of the layers was rotated on top the other layer with misorientation angle close to 30º, as demonstrated in Figure 4-6.

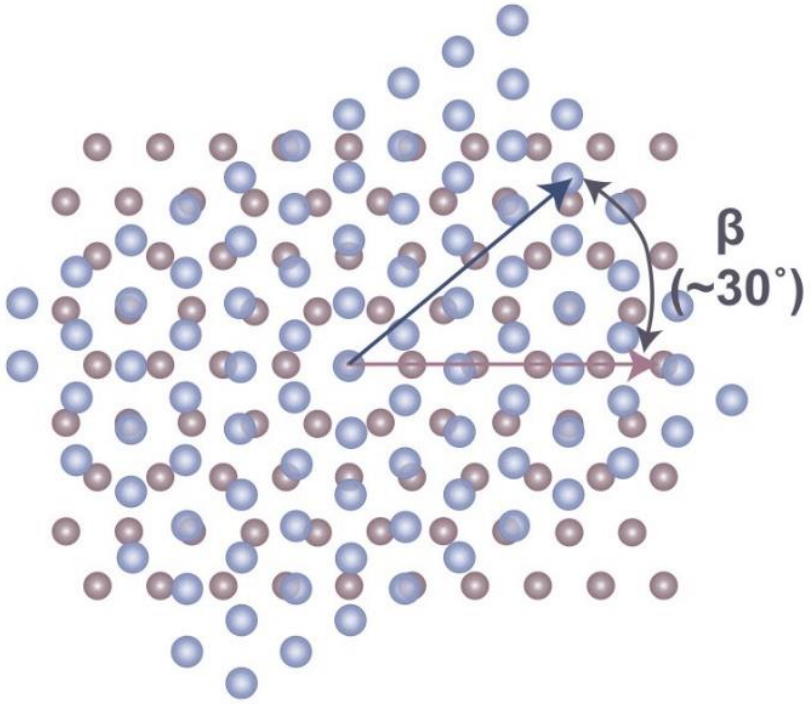

Figure 4-6 Computer generated aperiodic quasicrystal patterns, made of two hexagonal lattices with misorientation angle close to 30 degrees.

In the previous studies[116,120,121] the dodecagonal quasicrystals were formed through static self-assembly, and the procedure of creating them required special methodologies (lithography methods[116], magnetron sputtering in ultrahigh vacuum conditions[120], special synthesis and centrifugations[121]). Here we were able to dynamically observe these exotic patterns without the need for any prior modifications to the setup. Similar to Moiré patterns these structures are formed of two layers of hexagonal lattices rotated on top of each other which can be due to the fluid flow in the middle of two layers.

Figure 4-7 shows bright field microscopy images of experimentally observed quasicrystals, their computer generated lattices and Fast Fourier Transform (FFT) of each pattern. We performed FFT on the raw experimental images and compared the results with FFT of perfect drawn crystals in computer to identify their misorientation angle.

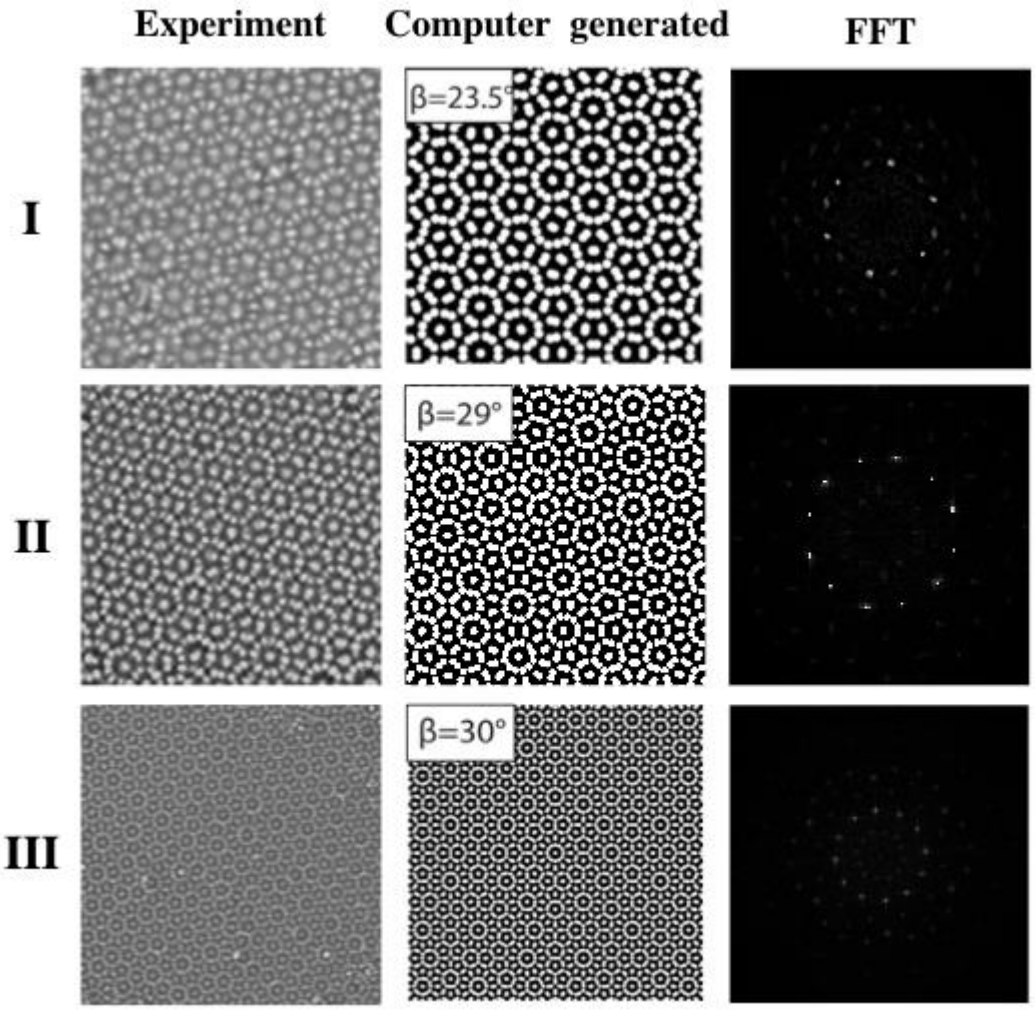

Figure 4-7 Bright field microscope images, computer generated lattices and FFTs of experimental quasicrystals lattices. Depending on the misorientation angles, various types of Honeycomb patterns can be observed in the system.

4.5 Dynamic adaptive crystals with multi and mono-stable structures

The colloidal crystals reported in this study are formed through dynamic self-assembly. As discussed in chapter two, dynamic self-assembly process requires continuous energy flow which is provided by femtosecond laser here. Dynamic structures are not at thermal equilibrium and require energy to sustain. If the energy source (laser) is cut off from the system dynamic structures are destroyed and system develops toward its thermodynamic equilibrium configuration. Figure 4-8 shows dynamic behavior of the colloidal crystals observed in this system. When the laser is on, positive feedback (laser induced flows as described in Figure 2-6) overcomes

negative feedback (Brownian motion of particles as described in Figure 2-6) and aggregates grow (Figure 4-8-I&IV), as soon as laser is turned off (Figure 4-8-II&V) there is only negative feedback in the system and the aggregate starts dissolving and after approximately 30 seconds the particles that formed the aggregates are still dissipating back to the system until a homogenous distribution of particles is achieved.

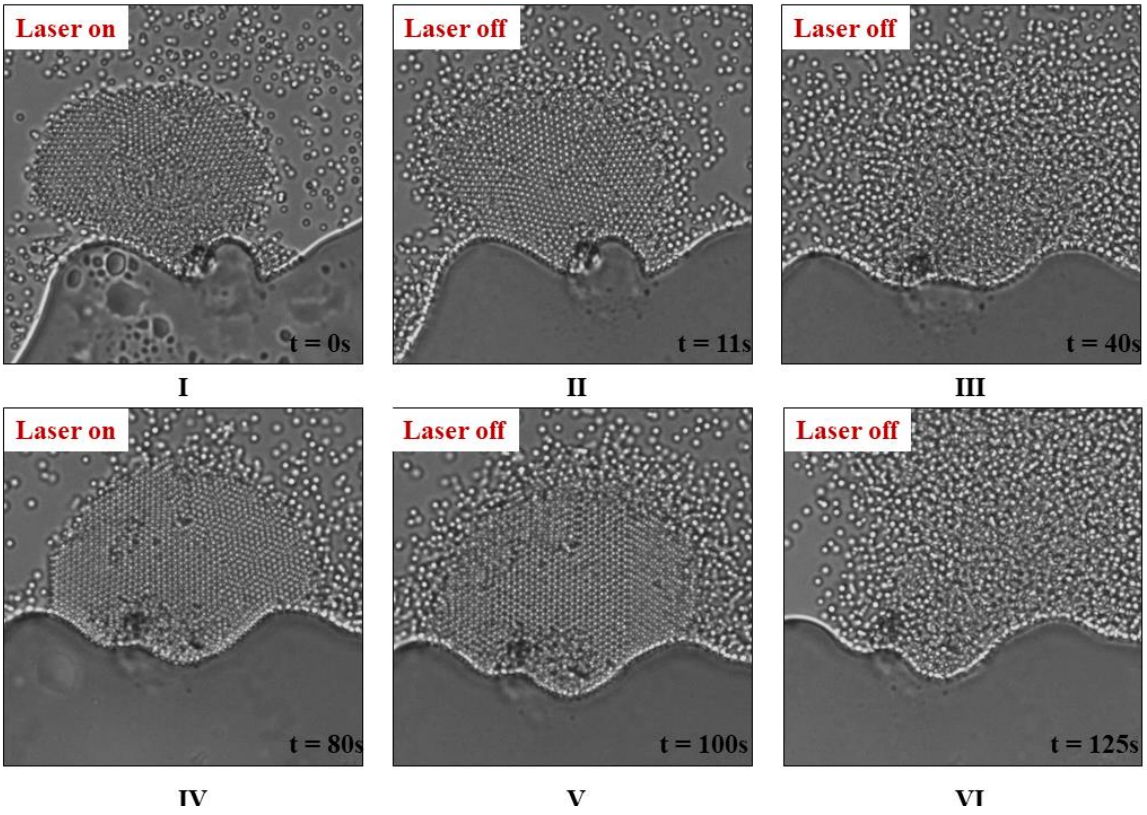

Figure 4-8 Dynamic self-assembly of colloidal crystals; when laser is on laser induced flows are formed due to spatiotemporal thermal gradient, the flows bring particles toward laser point inside the bubble and the aggregate grows (I, VI), when the laser is turned off there is no laser induced flow anymore and the aggregates start dissolving into the solution random Brownian motion of particles (II,V), after ~30 seconds particles are more dispersed into the solution (III, VI).

Experimental studies based on dynamic self-assembly have some advantages over static self-assembly, these studies provide platforms to investigate unique properties of dynamic structures such as adaptability, self-healing, self-replication and the ability to withstand large perturbations which are closely related to dynamic nature of structures[2]. One example of dynamic behavior of the colloidal crystals is demonstrated in Figure 4-9 with a scenario of two aggregates on each side of a bubble.

This case shows the ability of system to withstand small perturbations: At t = 0 s there is Moiré pattern on the left and quasicrystal on the right of Figure 4-9, in response to small fluctuations due to changes in fluid flow in system the aggregate on left (Figure 4-9 panel A) changes from one type of Moiré pattern to another type of Moiré pattern with a slightly larger misorientation angle at t = 2 s, and the aggregate on the right (Figure 4-9 panel C) changes from quasicrystal to different types of honeycomb lattices at t = 4 s and t = 10 s. In this example the perturbations are not large enough to destroy the crystals, instead they push the system from one steady state to another.

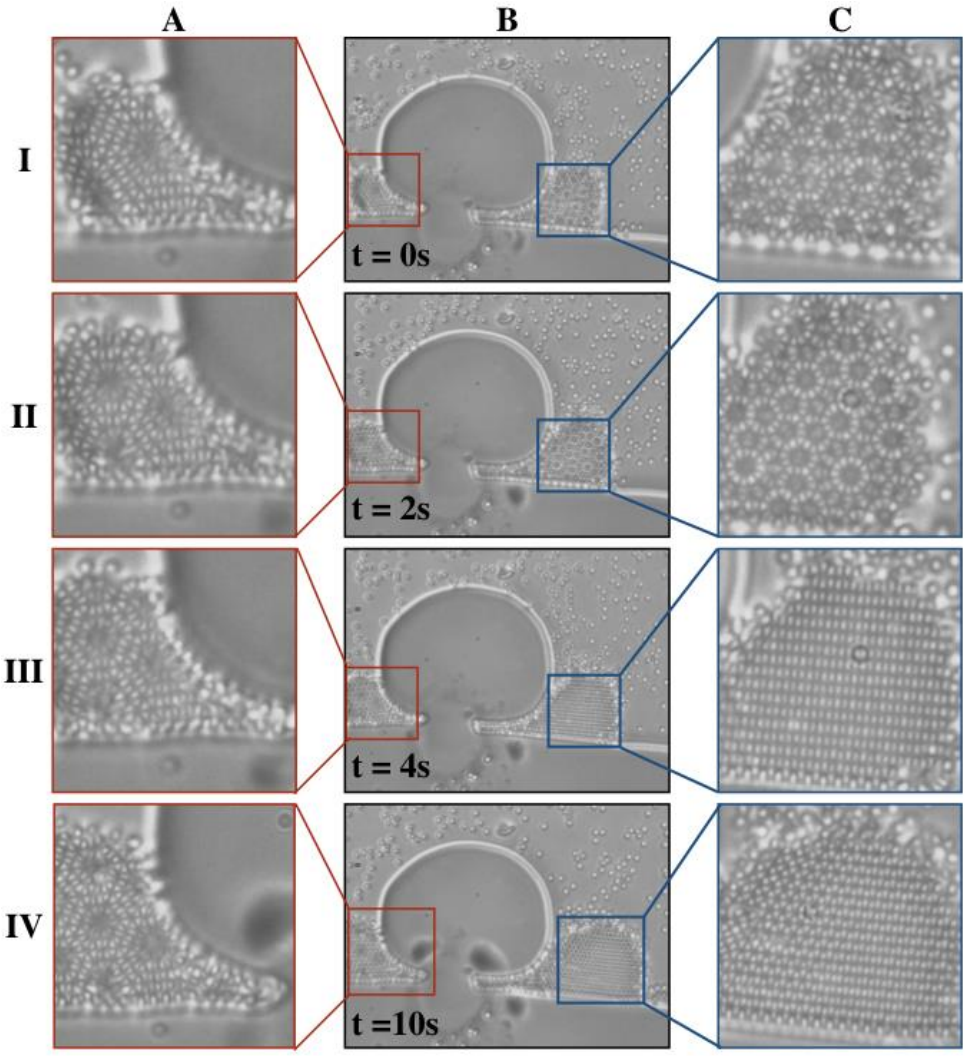

Figure 4-9 Dynamic behavior of far from equilibrium colloidal crystals; Starting with I-A) Moiré patterns, and I-C) quasicrystals at t = 0, s which changes to II-A) another type of Moiré patterns at t = 2 s, and III-C) type three honeycomb at t = 4 s and IV-C type two honeycomb at t = 10 s.

These dynamic colloidal crystals exhibit adaptability. Adaptability is the ability to respond to changes in environment and modify the structure in response to perturbations in environment that makes the structure a better fit for the new conditions, such as response of the system to large perturbations or changes in energy flow and environmental conditions (bubble boundaries). If a perturbation is large enough to change the fluid flow in a way that can result in movement or destruction of a pattern even for less than a second (such as sudden change in bubble configurations or sudden movement of laser position) we refer to it as large perturbation. If the perturbation is not large enough to move or destroy the whole pattern we refer to it as small perturbation.

Figure 4-10 shows the response of the system to large perturbations in the environment. In this example perturbations are large enough to destroy the crystals completely or a part of them and rearrange it again. Figure 4-10 panel A demonstrates a honeycomb aggregate at t = 0 s, after 3 seconds system is largely perturbed, the aggregate is slightly separated from the bubble for a very short time and is formed again. The new aggregate is in form of coexisting patterns of hexagonal and Moiré patterns (at $t = 10s$). The large perturbation was applied to the system by changing the laser beam position slightly, which changed the Marangoni flow and separated the aggregate from the bubble at $t = 3s$ (Figure 4-10A-II), accordingly the honeycomb pattern rearranged itself to coexisting patterns of hexagonal and Moiré.

Most of the fluctuations decay gradually until the system returns to its original state, yet when the system is far from equilibrium, they can be amplified fluctuations called giant number of fluctuations, which can change the state of order in system[4,115] as seen in Figure 4-10.

Figure 4-10 panel B shows coexisting patterns of quasicrystal and honeycomb at t = 0 s, after a large fluctuation in bubble boundary which changed the shape of the boundary at t = 2 s, the quasicrystal aggregate is destroyed and rearranged in form of honeycomb lattice at t = 3 s.

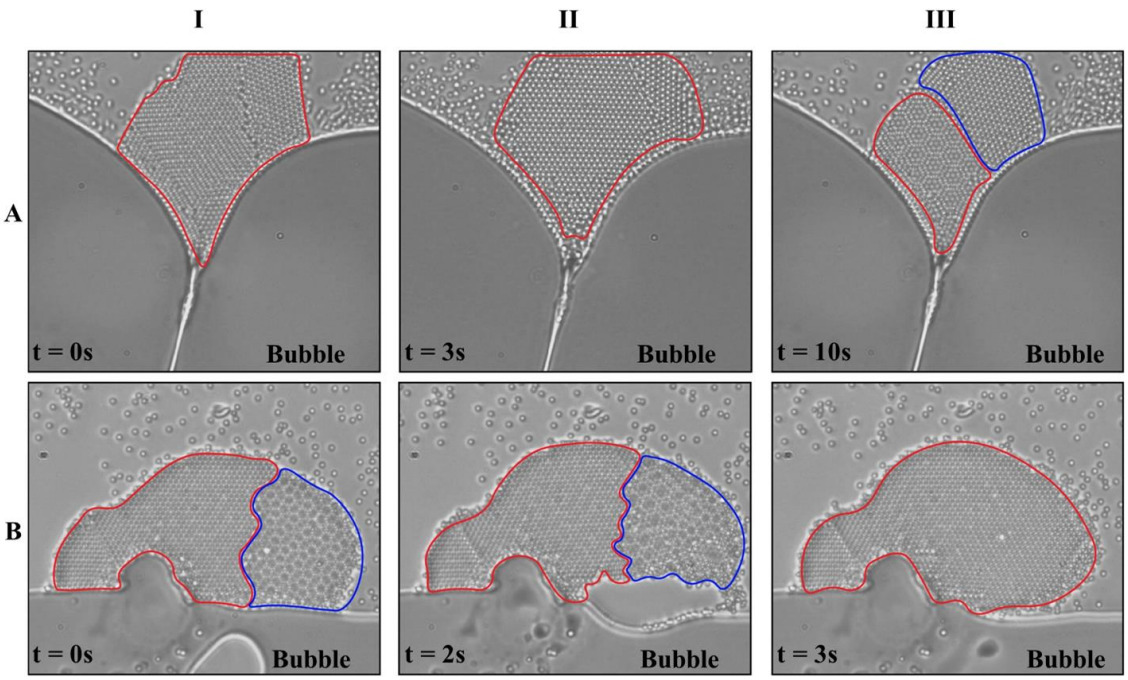

Figure 4-10 Time-lapse images showing response of the system to large perturbations, the fluctuation is defined as large here since it destroyed the patterns for a short time; Panel A: starting with an aggregate of honeycomb lattices (A-I) which changes to two grains of hexagonal and Moiré patterns (A-III) due to a large perturbation induced by changing the laser position at t = 3 s (A-II); Panel B: starting with the aggregate of honeycomb lattice coexisting with a quasicrystal (B-I) which changes to one single grain of honeycomb lattice (B-III) due to a large perturbation induced by a fluctuation in bubble boundary at t = 2 s (B-II).

These dynamic structures are far from equilibrium, and retain themselves by continuous energy flux supplied to the system, each of the dynamic colloidal crystals observed here represent a stable attractor (an attractor is a state that a nonlinear system tends to evolve toward in for a wide variety of initial conditions, *i.e.*, steady states) in the phase space. The structure of stable attractors depends only on environmental constraints[2] (here, thickness of the liquid film, concentration of the particles, velocity and type of fluid flow, and internal fluctuations) and energy flow (here, position of the beam and laser power). Therefore, changes in environmental conditions and energy flow can create, destroy or modify the stable structures.

The dynamic crystals can change their structures in response to the perturbations, meaning they can switch between the available configurations in response to changes in their environment (perturbations). Far from equilibrium

conditions provides possibility of converting a structure to another structure and jumping between the available steady states in the phase space. However, the conversion of patterns to each other was not observed in all the structures within the scope of our experiments. The reason is that the required environmental conditions and energy flux parameters to form some patterns can be quite different from the other patterns. This means there are some environmental constraints that limit formation of patterns in one spatial positions, such as thickness of the liquid film and Brownian motion of particles which will be discussed in details in the following sections.

One of the most observed conversion between patterns is in case of double layer hexagonal, Moiré and honeycomb patterns, these patterns can interconvert to each other in response to smallest perturbations as demonstrated in Figure 4-9 and Figure 4-10. Conversion between double layer square patterns and single layer hexagonal, rectangular, Moiré, honeycomb patterns has not been observed. Similarly, conversion of single layer hexagonal pattern to any patterns other than double layer rectangular pattern has not been observed in the system, more details are provided in section 4.9. It can be said that if two structures are capable of converting to one another, their corresponding attractor in the phase space are close to each other, and environmental conditions and energy flow properties required for those structures have common factors[2].

Another example showing adaptability in these crystals is shown in Figure 4-11. This example demonstrates the adaptive behavior of crystals in response to changes in physical boundaries; originally at $t = 0$ s Moiré and hexagonal patterns are coexisting, upon shrinkage of bubble (Figure 4-11-I&II) the Moiré pattern changes in size and rotation angles to be a better fit to the new boundary conditions.

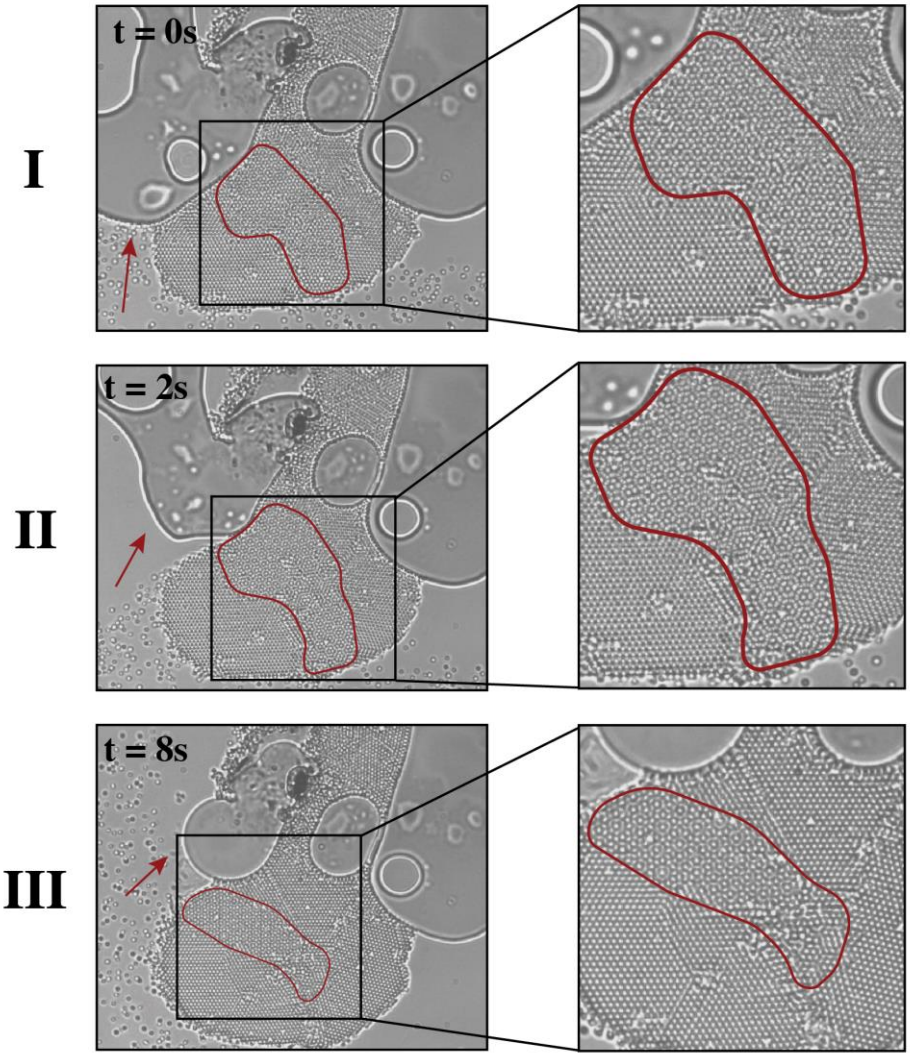

Figure 4-11 Time-lapse bright field microscope images showing adaptive behavior of the dynamic colloidal crystals to the changes in the physical boundaries; initial coexisting patterns are Moiré patterns and hexagonal (I), upon shrinkage of bubble the Moiré patterns change in time (II) and eventually turn some portions of itself to hexagonal pattern (III).

The coexisting aggregates are capable of competition, meaning different crystals compete with each other for the limited resources (particles). Figure 4-12 shows time-lapse images of two coexisting aggregates of quasicrystal and hexagonal patterns, these crystals grow in time and compete for the particles dragged by flow, where after 84 seconds (Figure 4-12V) the aggregate saturates and after 28 seconds (Figure 4-12VI) hexagonal lattice “wins” the competition and eventually converts the quasicrystal to hexagonal pattern.

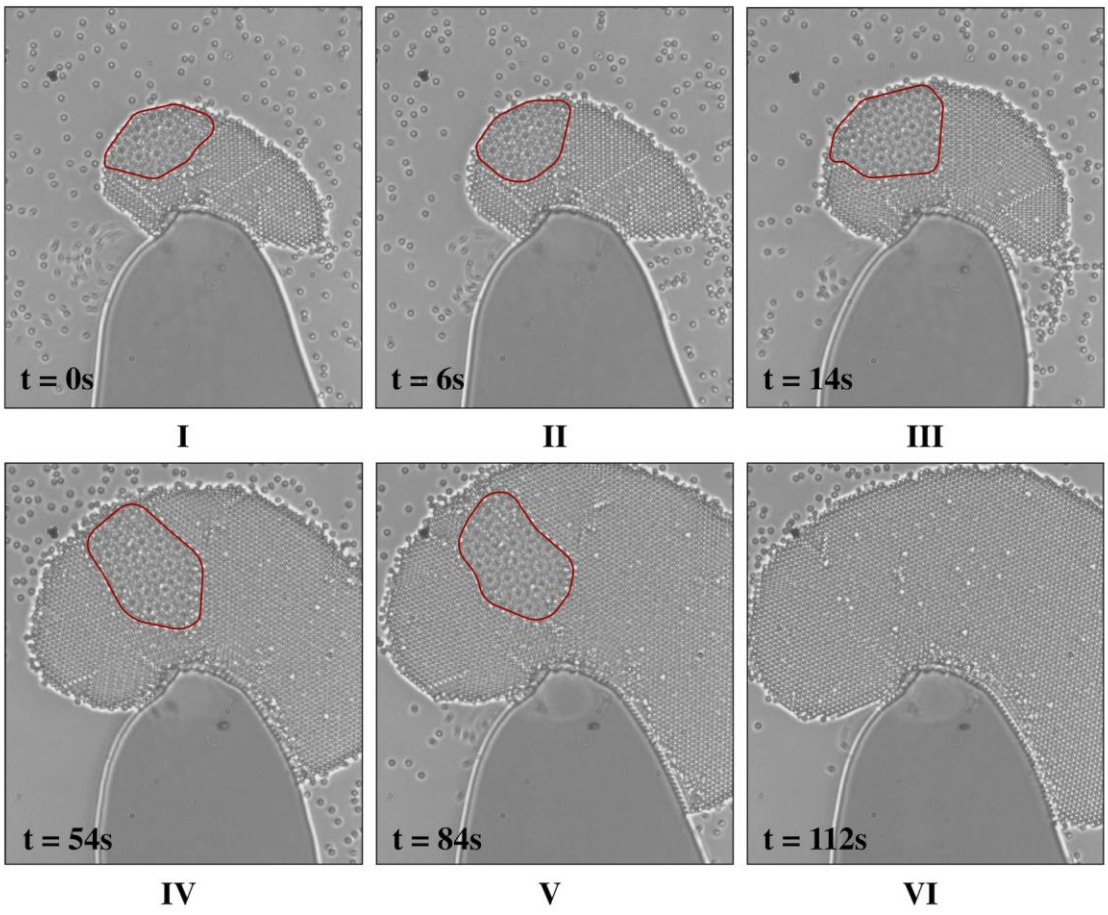

Figure 4-12 Time-lapse images showing competition between honeycomb lattice and quasicrystal, where eventually the quasicrystal turns to honeycomb lattice after 112 seconds.

In response to the fluctuations (internal such as Brownian motion and external such as changes in laser position and power), and perturbation in the environment, some defects and errors rise in the dynamic crystals. Each dynamic state is representative of a basin of attraction of an attractor in phase space (it is a region in the phase space such that any point in that region eventually evolves toward the attractor), if a state is perturbed depending on how large the perturbations are, the system can either heal and return back to its stable state or switch between the available steady states and evolve into another stable configuration. If the perturbation is large enough to push the system out of the current basin of attraction[2,4]. Given time and energy, these dynamic crystals try to diminish their structural defects and imperfections which is called self-healing. Figure 4-13 shows an example of self-healing in these crystals, in the left frame the aggregate has structural defects such as

vacancies (some of which are shown by arrows), after approximately 10 seconds in the right frame we see these defects are diminished.

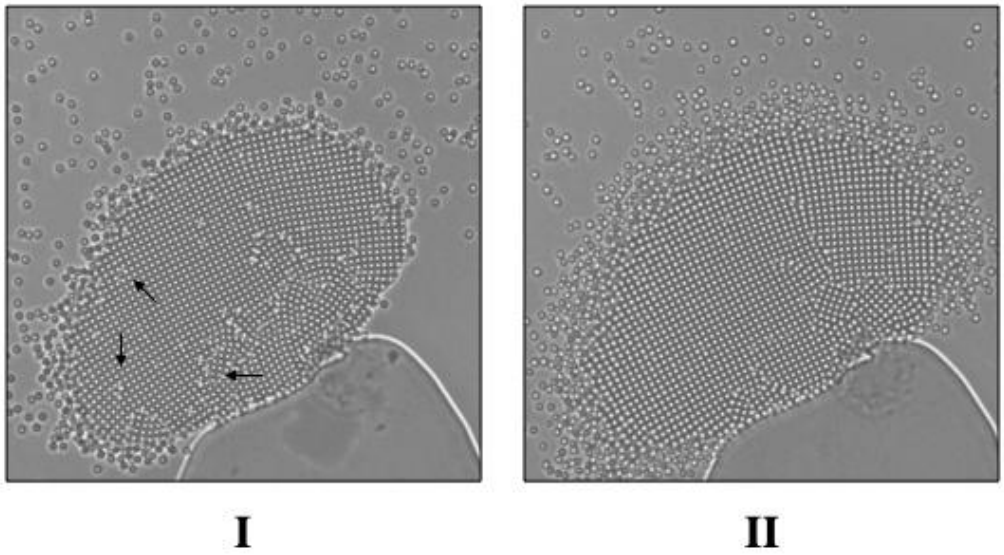

Figure 4-13 Self-healing of a square pattern; I) arrows showing vacancies and defects, II) self-healed square pattern after 10 seconds.

In other words, the system adapts to large perturbations (see Figure 4-10) and heal the small imperfections (see Figure 4-13).

Furthermore, if an aggregate is created through a fast deposition meaning particles do not have enough time to find their perfect position, the aggregate can exhibit amorphous structure. Given enough time these initially amorphous aggregates can anneal into an ordered structure. Figure 4-14 demonstrates transition of an initially amorphous aggregate into square patterns.

So far the types of patterns observed in this study and their properties have been introduced. Next step is to investigate the experimental parameters affecting formation of various patterns, first laser induced fluid flow is investigated, then the effect of Brownian motion velocity as the source of internal fluctuations is studied and finally the effect of liquid film thickness is reported.

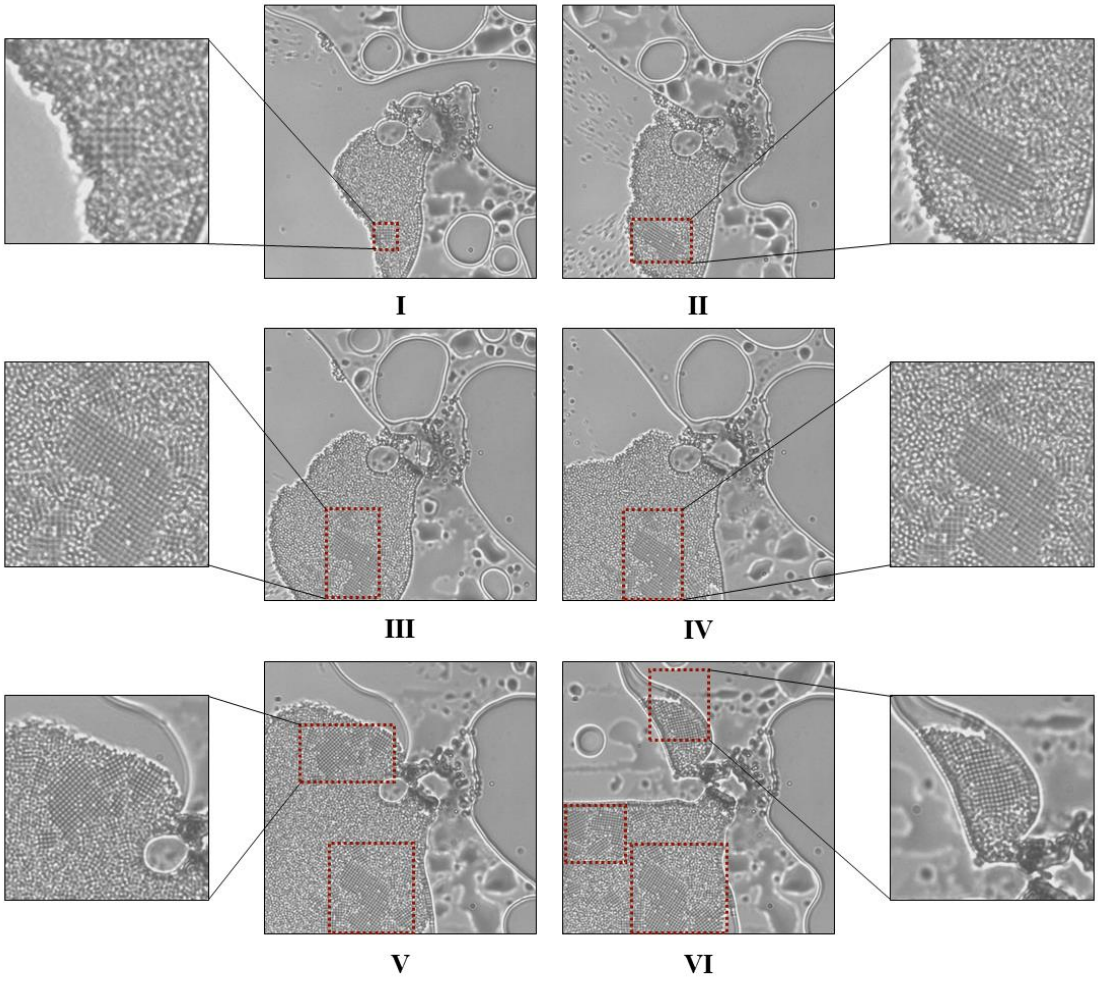

Figure 4-14 Time-lapse bright field microscope images showing transition of amorphous aggregate into square pattern; Red rectangles show the square pattern grains, between each two images there is ~5 seconds time difference.

4.6 Fluid field simulations

We analyzed more than 1200 minutes of video shooting from more than 20 samples, and classified the observed bubbles to 5 different shapes. Fluid flow simulations were conducted for this 5 classes of experimentally observed bubbles as shown in Figure 4-15. The results of simulations are provided in Figure 4-15. We performed the simulations for $\Delta T = 2$ K, ΔT shows the temperature difference between laser spot and the environment. The velocity of the fluid fields in all the

cases share similarities. Here laser is defined as a boundary heat source. There is a dark blue region in velocity fields close to laser position, which shows the velocity of fluid in these regions is very low and close to zero. This area is where the patterns are formed, if the velocity of fluid is high colloids cannot form aggregates because they will be dragged by the fluid.

Let's take a look at pressure fields, the dark blue lines indicate lower pressure areas compared to surrounding which would drag the particles form high pressure areas toward the lower pressure parts. In the first three bubble shapes (Figure 4-15 I, II, III) the low pressure area is much larger than the last two bubble configurations (Figure 4-15 IV, V), while the fluid velocity field is very similar in all the bubble types.

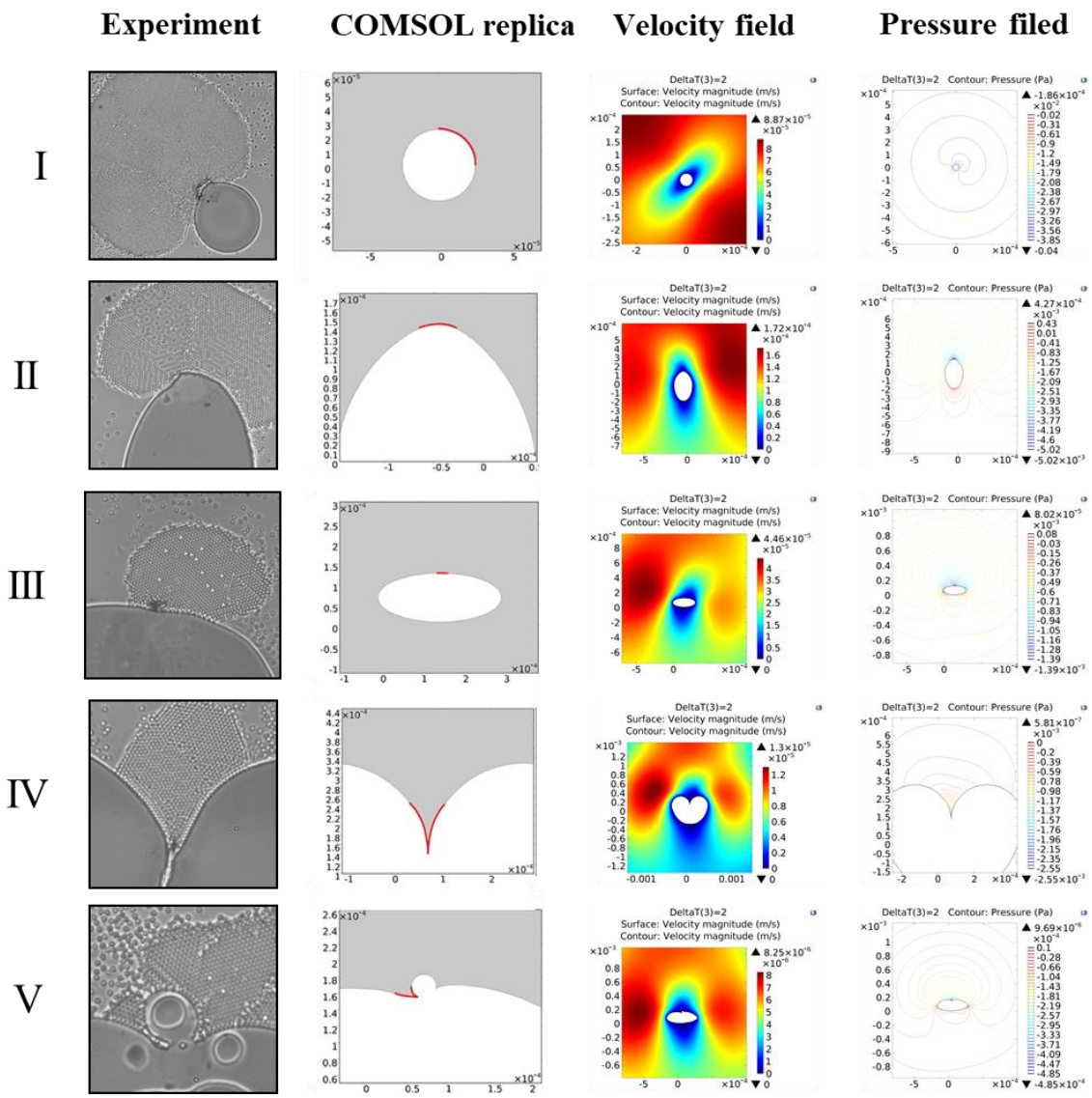

Figure 4-15 Simulated fluid velocity fields and pressure fields for replicated physical boundaries, I) Spherical bubbles; II) Elliptical bubbles; III) Flat bubbles; IV) V-shaped bubbles; V) a spherical bubble on flat bubble.

Furthermore, the effect of curvature or concavity of V-shaped bubbles on velocity and pressure fields were investigated, Figure 4-16 demonstrates the comparison between two V-shaped bubbles. The V-shape in these bubbles can vary, meaning the angle can be wider or smaller. The v-angle of the bubble shown in Figure 4-16I is wider than the bubble shown in Figure 4-16II. Although the velocity fields of these bubbles are very similar, pressure fields show significant difference, as the bubble has smaller v-angle, the dark blue lines cover smaller area, hence low pressure

area is larger wide angle v-shaped bubbles. The patterns are formed in low velocity and low pressure regions, therefore patterns formed in wide angle bubble V-shaped bubble are more likely to grow larger in low pressure region compared to low angle V-shaped bubbles.

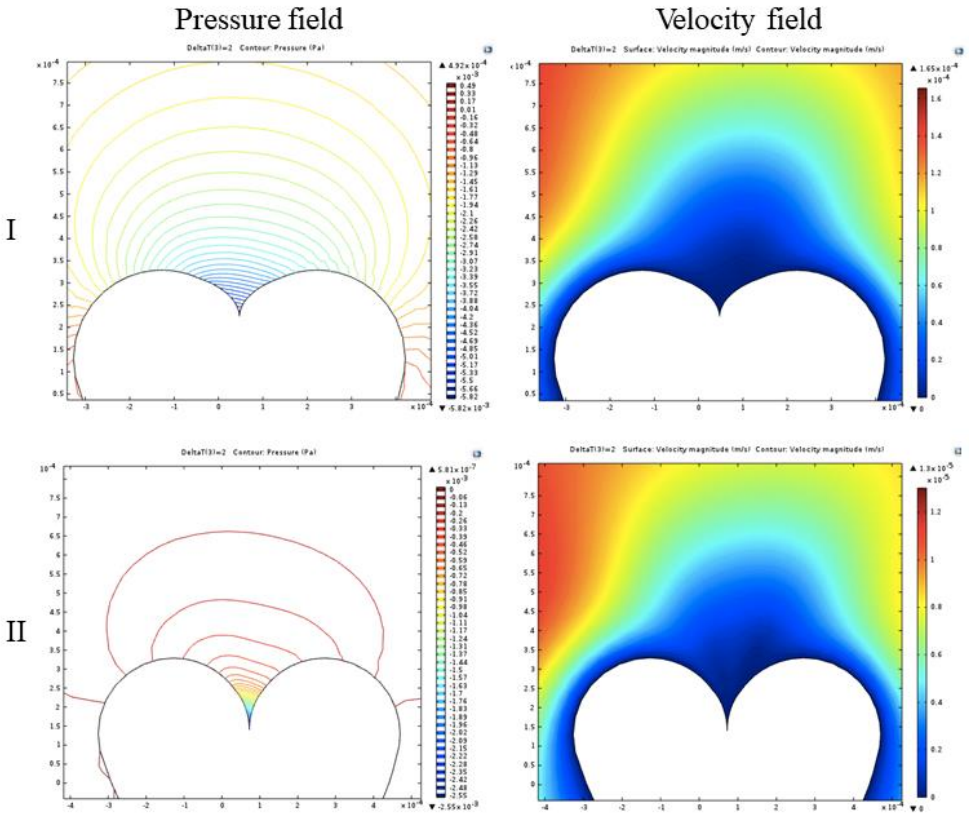

Figure 4-16 Comparison between pressure and velocity fields based on concavity of bubble.

The results of fluid flow simulations for all types of bubbles are very similar; and within the scope of our experiments all patterns have been observed in all types of bubble shapes. Therefore, we cannot answer the question that what type of patterns are more likely to be seen in which bubble configurations. Yet, we can answer the question that where and why we get any pattern at all. Patterns are formed in the low velocity area close to bubble, the fluid flow brings large number of particles toward the low velocity area, resulting in an increase in interparticle collisions, and overcoming the Brownian motion which forms aggregates at the bubble boundary which is why aggregates are formed[4,12,13].

4.7 Effect of thickness of the liquid film and related parameters on formation of patterns

4.7.1 Constraints of thickness of the liquid film

Thickness of the liquid film is an experimental parameter that can affect formation of patterns. Theoretically we can calculate the minimum thickness required for each pattern, this provides a geometrical constraint. If it is not satisfied, formation of certain patterns is geometrically impossible. We define the thickness as the distance between two glass slide which can vary throughout the sample for two reasons: First, the surface of glass slides is not completely flat and has peaks and bottoms; Second, the colloidal solution is not uniformly spread between glass slides in sample preparation step.

Figure 4-17 shows schematic illustration of the top and cross section view of a computer generated single layer hexagonal pattern. Since there is only one layer, the minimum thickness required for this pattern is the same as the diameter of particles, which is 0.5 μm. However, since these patterns are dynamic they have the possibility to move up and down and change their structure in the liquid. They are not completely confined by the two glass slides and there should be a layer of liquid (either above or beneath the pattern) to enable slight movement of particles along Z direction hence we can say that thickness required for obtaining single layer hexagonal pattern is larger than 0.5 μm.

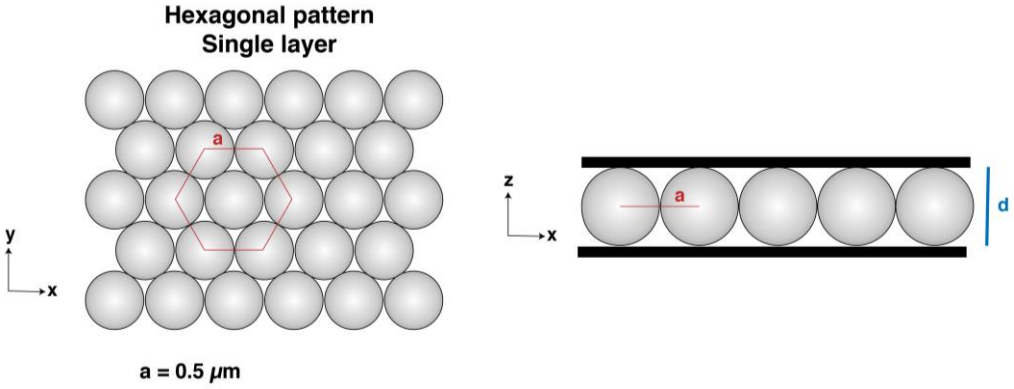

Figure 4-17 Schematic illustration of top and cross section view of a computer generated single layer hexagonal pattern.

Rectangular patterns that were observed in our experiments were made of at least two layers. The particles in second layer are not exactly located on top of the

particles in the first layer, they are positioned on the empty wells between the particles of the first layer (for 3D pictures check appendix B). Figure 4-18 demonstrates the top and side view of a computer generated rectangular lattice. The values of *a* and *b* are measured from experimental pictures using ImageJ software, a is equal to the diameter of particles which is 0.5μm, and b was measured to be 0.77μm. Using geometrical relations, the minimum thickness of a quasi 2D rectangular lattice is calculated to be 0.7 μm. For the same reasons mentioned above about the one-layer hexagonal pattern, the minimum thickness of liquid film required to obtain rectangular pattern should be larger than 0.7 μm.

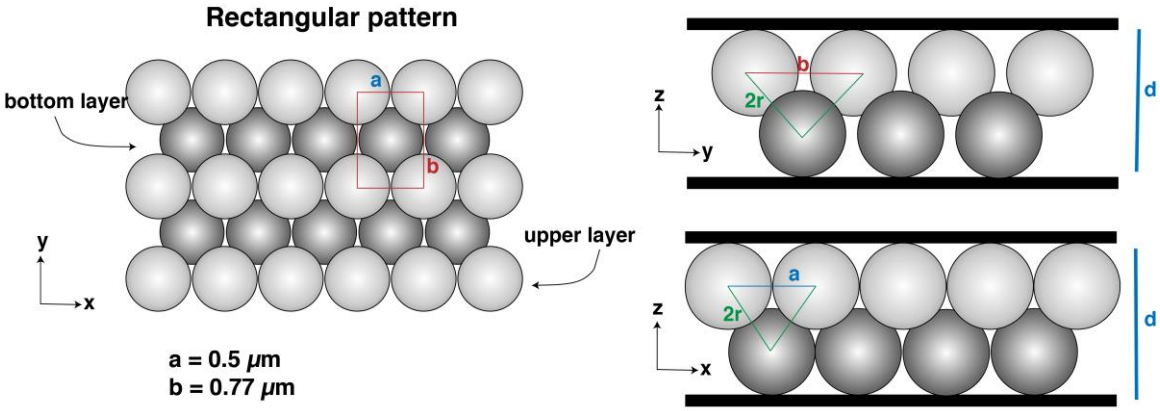

Figure 4-18 Top and cross section view of rectangular pattern, different colors indicate different layers of colloids (check appendix C for 3D images).

Similar to rectangular patterns, square patterns observed in our experiments are quasi 2D. We also calculated the thickness of square patterns, which are made of at least two layers (Figure 4-19). The parameter a is the lattice constant here which was measure to be ~580nm, so particles in one layer of square lattice do not touch each other, and the packing direction is [1 1 1] in terms of miller indices. The thickness of totally confined square pattern is 0.79 μm, hence the minimum thickness required to obtain 2-layer square pattern in our system is larger than 0.79 μm.

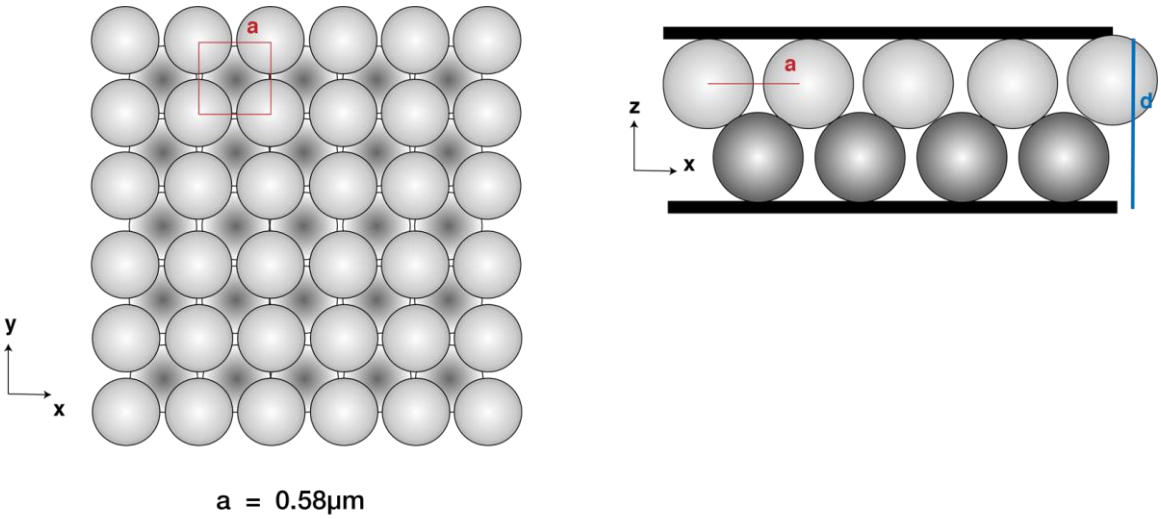

Figure 4-19 Top and cross section view of square pattern (check appendix C for 3D images)

Thickness of totally confined two-layered hexagonal pattern (Figure 4-20) was calculated to be 0.9 μm using the same method. This means that the minimum thickness required to observe double layer hexagonal pattern is larger than 0.9 μm.

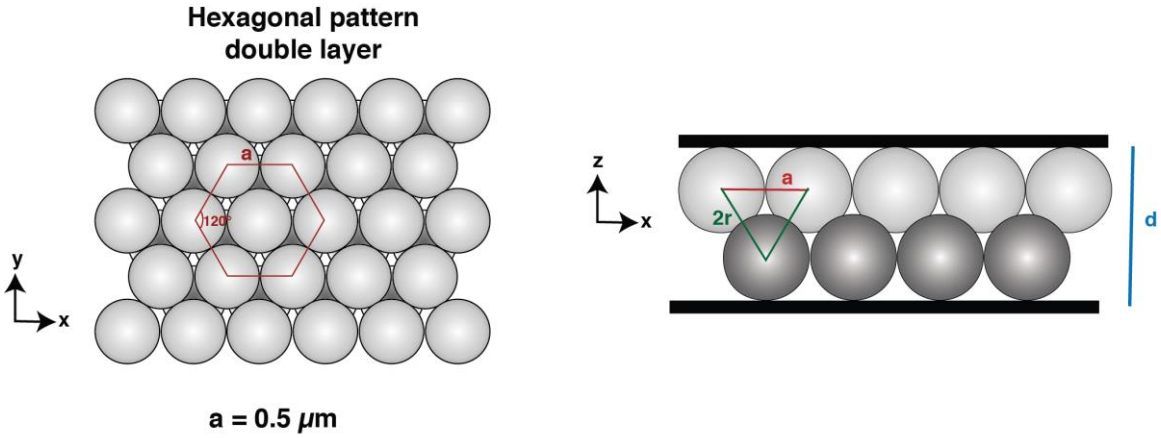

Figure 4-20 Top and cross section view of computer generated double layer hexagonal pattern.

Minimum thickness value for formation of Moiré patterns is varying between 0.9 μm to 1 μm depending on the misorientation angle of Moiré patterns, since Moiré patterns are double layer hexagonal structures, which one layer is slightly rotated on the other layer hence the upper layer is not placed on the tetrahedral holes, it is placed slightly over the holes based on the rotation angle. The layers can rotate on top of each

other due to fluid flow in the middle of layers, small changes in the direction or strength of the flow can result in movement or rotation of hexagonal layers on top of each other. Therefore, we can easily see transformation of Moiré patterns, honeycomb patterns and quasicrystals to each other.

The only one-layer pattern observed in our system is hexagonal lattice which is two-dimensional, the rest of the observed patterns are quasi 2D and are made of at least two layers of particles. Therefore, if the thickness is smaller than certain limits, some patterns are geometrically impossible to be observed, for example if the thickness of the sample is 0.85 μm we cannot observe double layer hexagonal patterns, but single layer hexagonal lattices, rectangular pattern, and square patterns are possible to be formed. As the thickness increases, there will be the possibility to observe multiple patterns. If the thickness is about 1 μm and larger all the patterns are geometrically possible to be formed.

One of the earliest studies on effect of thickness on formation of colloidal crystals was conducted by P. Pieranski *et.al* (1983)[122]. They confined colloidal solution of polystyrene spheres (1.1 μm in diameter) between two slides and slowly increased the thickness by moving one of the slides in Z direction, and observed series of patterns. By increasing the thickness slowly, the observed transitions from single layer hexagonal, to double layer rectangular lattice, double layer square lattice and double layer hexagonal, which has the same trend that was observed here. However, the self-assembly process was static there, and the crystals did not have dynamic behavior, yet it can confirm that thickness is an important parameter in formation of quasi two-dimensional colloidal crystals. Our system operates far from equilibrium which provides the conditions for dynamic self-assembly and assembly of various patterns. The experimentally observed structures in our system are much more diverse; Complex patterns such as quasicrystals, Moiré, and honeycomb patterns can be observed in our system. Furthermore, we are able to see dynamic transitions of these patterns to each other in response to perturbations and fluctuations of the system which was discussed earlier.

4.7.2 Brownian motion velocity and pattern formation

As described in fluctuation-dissipation theorem, the response of system to an external perturbation is generally related to internal fluctuations in the undisturbed

system[76]. Therefore, response of our system to external perturbation (caused by the laser) which is formation of patterns can be generally related to fluctuations of the system in undisturbed state (laser off) which is Brownian motion. To investigate how patterns change with respect to Brownian motion velocities of particles in undisturbed state, a set of experiments were designed as described in section 3.7.

The average Brownian velocity of particles when laser was blocked was calculated for each area, then the laser was turned on and types of patterns that could be obtained within the same spatial area (200μm * 200μm) were recorded.

Since our samples are quasi 2D, particles are confined by glass slides in Z direction. If particles undergo random Brownian motion near a fully wetted solid liquid boundary, their mobility would be lower compared to particles in bulk[109]. This is predicted by the following equation[110]:

$$D_w = D_b(1 - \frac{9R}{16h}) \qquad (4\text{-}1)$$

Where D_w is diffusion coefficient near wall (solid liquid boundary), D_b is diffusion coefficient in the bulk, kT is thermal energy, η is viscosity of liquid, and R is the hydrodynamic radius of the particle, h is the distance between center of particle and the wall[111]. It can be concluded from equation 4-1 that if the distance between particle and wall increases, the diffusion coefficient increases therefore mean square displacement also increases ($< x^2 >= Dt$). Which means as particles are more confined in Z-direction, their movement is slower and the velocity of Brownian motion decreases.

In total 43 videos were recorded from 15 samples, the videos were processed by the Matlab algorithm explained in section 3.8. The results of these experiments can be seen in Figure 4-21 to Figure 4-23. The statistical analysis and data are for following patterns: single layer hexagonal, rectangular, square, double layer hexagonal, honeycomb, Moiré and quasicrystal patterns. There are no statistical data on centered rectangle and oblique lattices since formation of these structures were rarely observed.

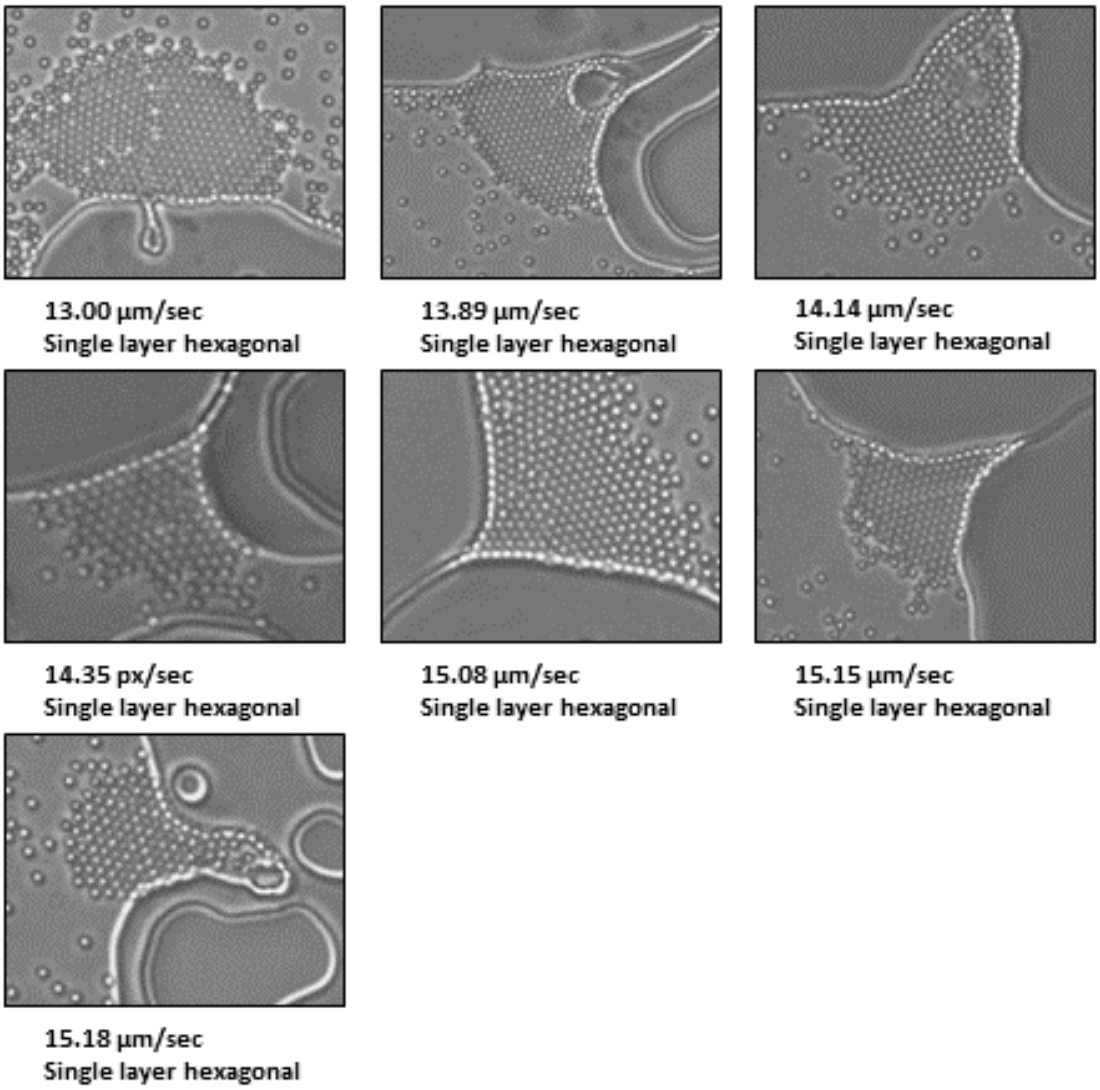

Figure 4-21 Snapshots of Brownian motion experiments for single layer hexagonal patterns and corresponding average Brownian motion velocities.

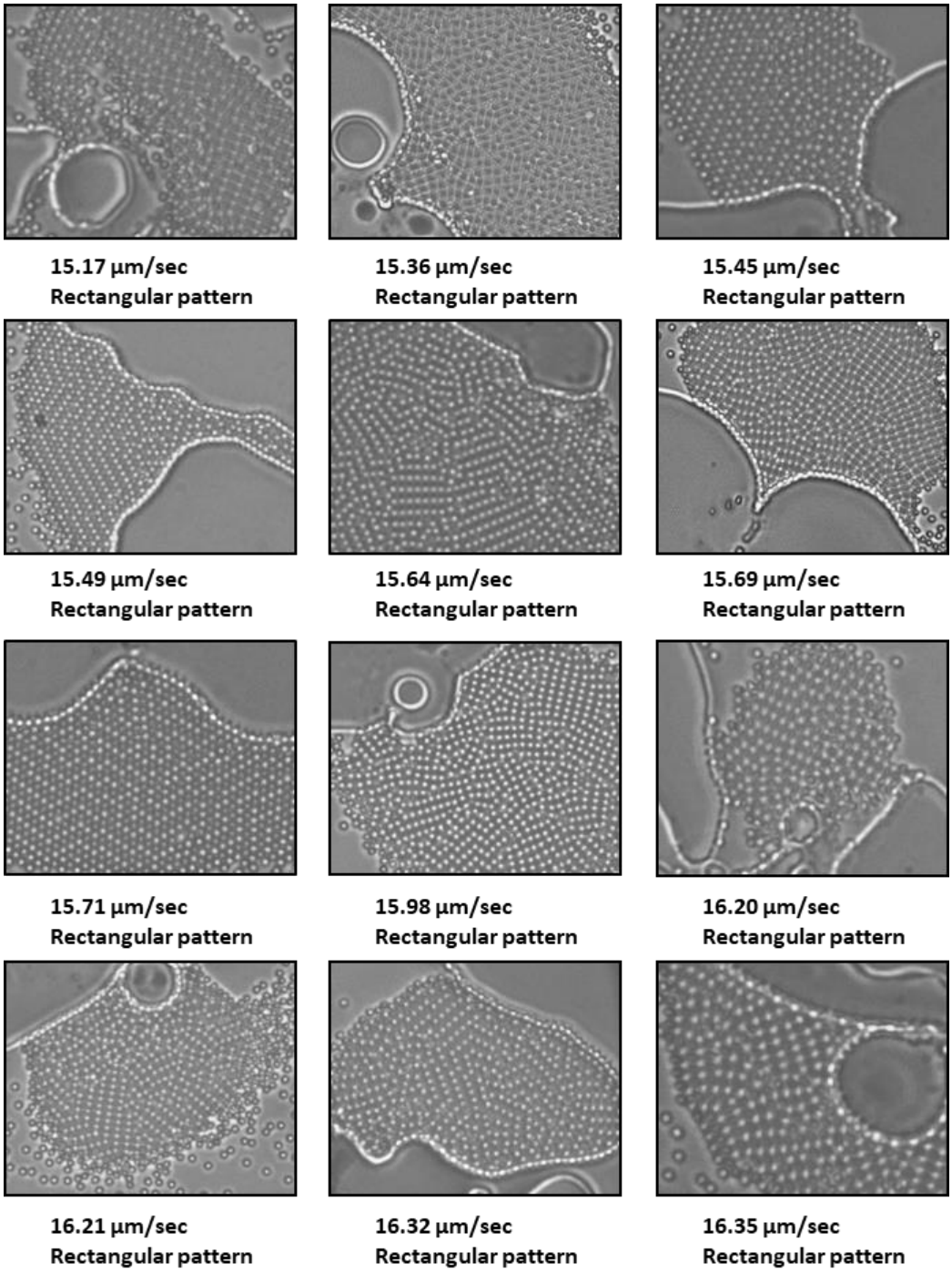

Figure 4-22 Snapshots of Brownian motion experiments for rectangular patterns and corresponding average Brownian motion velocities.

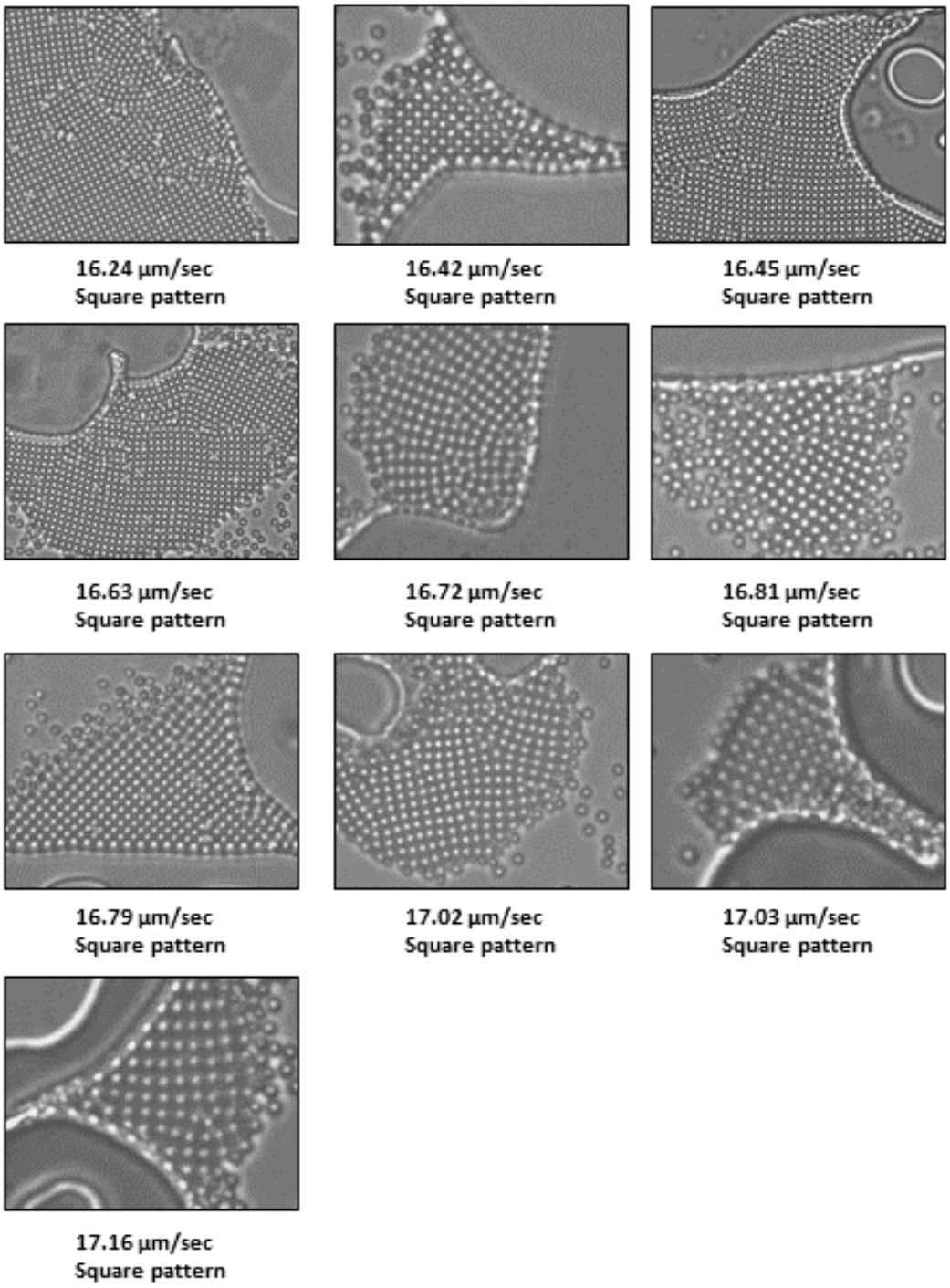

Figure 4-23 Snapshots of Brownian motion experiments for square patterns and corresponding average Brownian motion velocities.

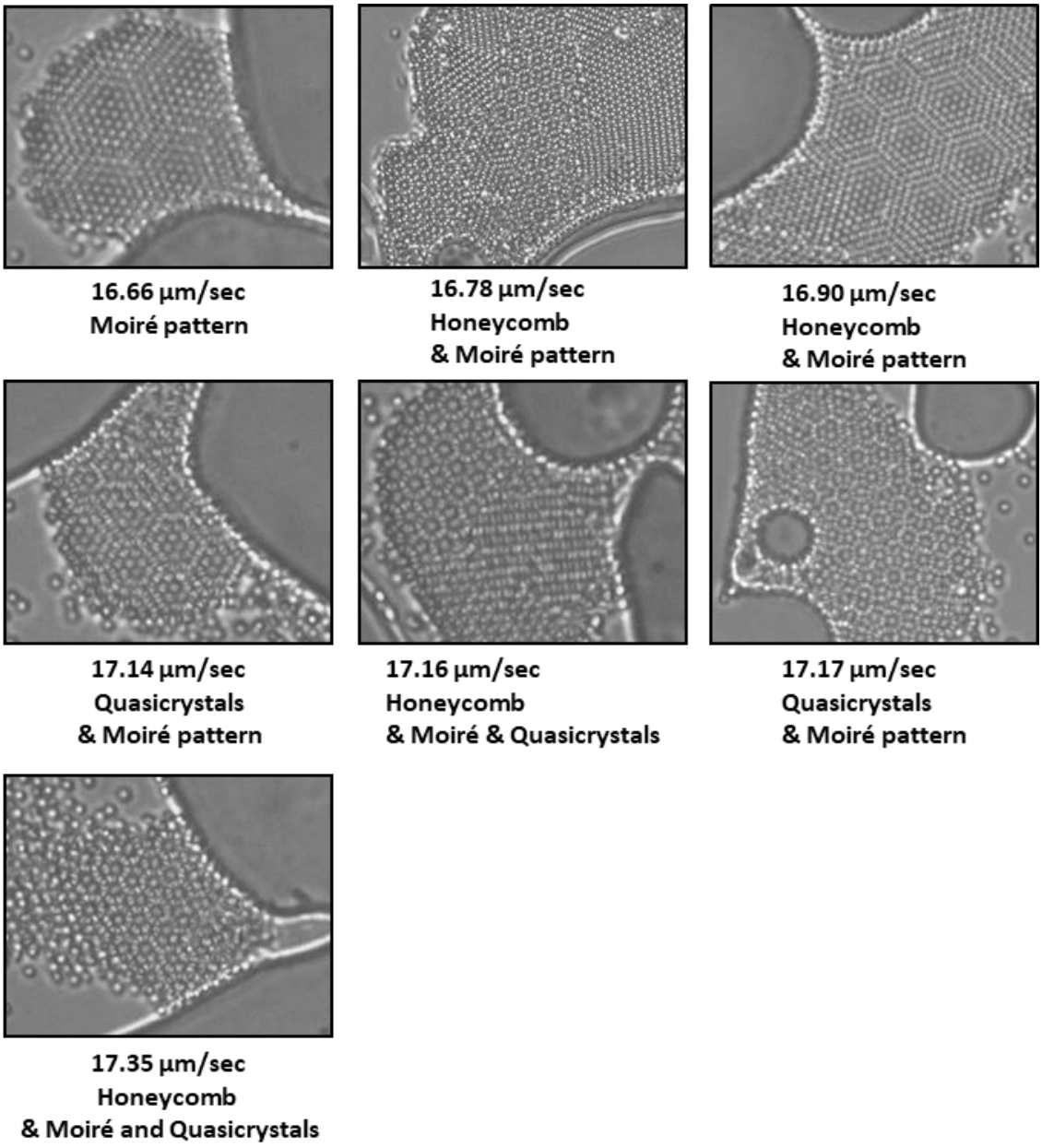

Figure 4-24 Snapshots of Brownian motion experiments for honeycomb, Moiré and Quasicrystals patterns and corresponding average Brownian motion velocities.

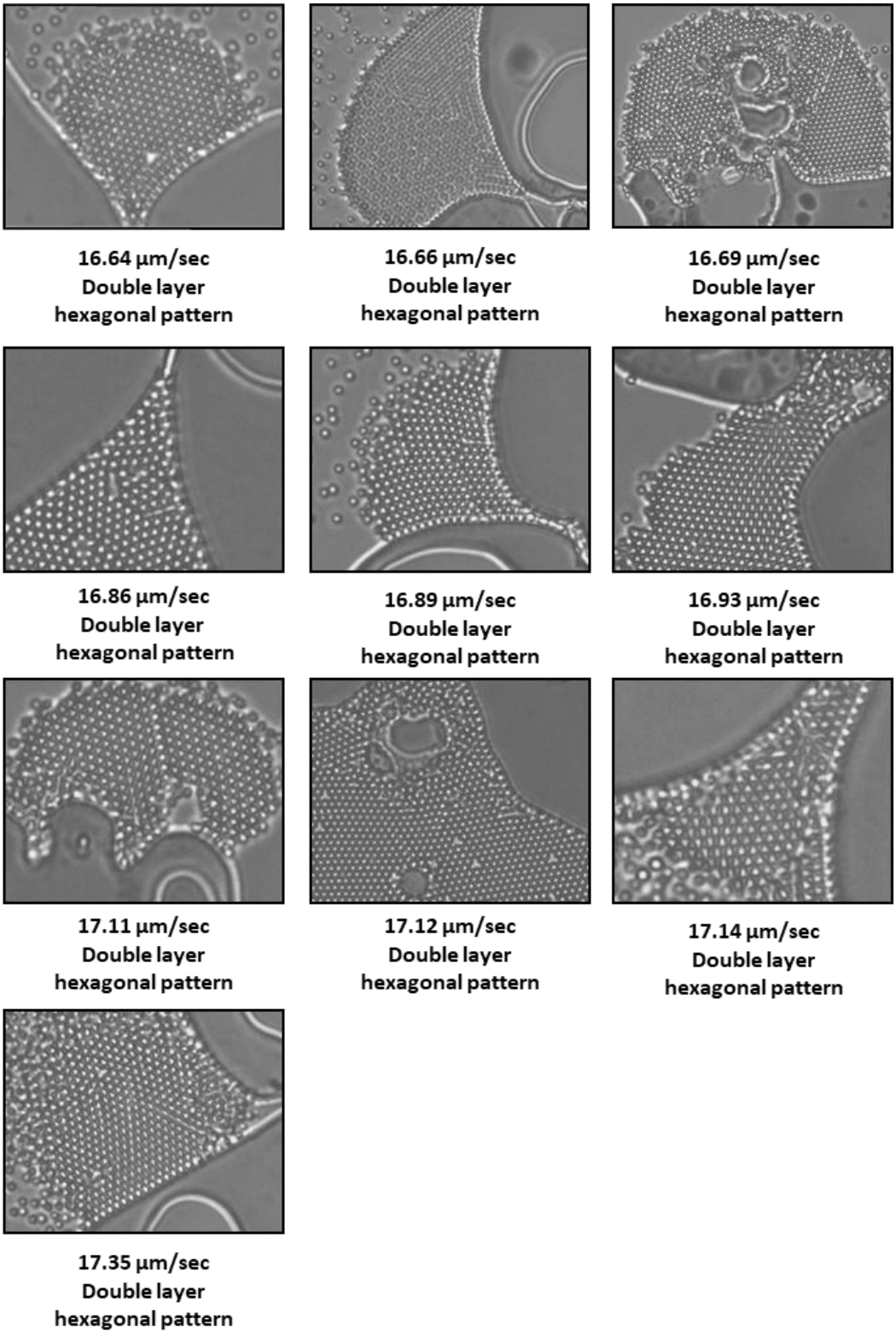

Figure 4-25 Snapshots of Brownian motion experiments double layer hexagonal patterns and corresponding average Brownian motion velocities.

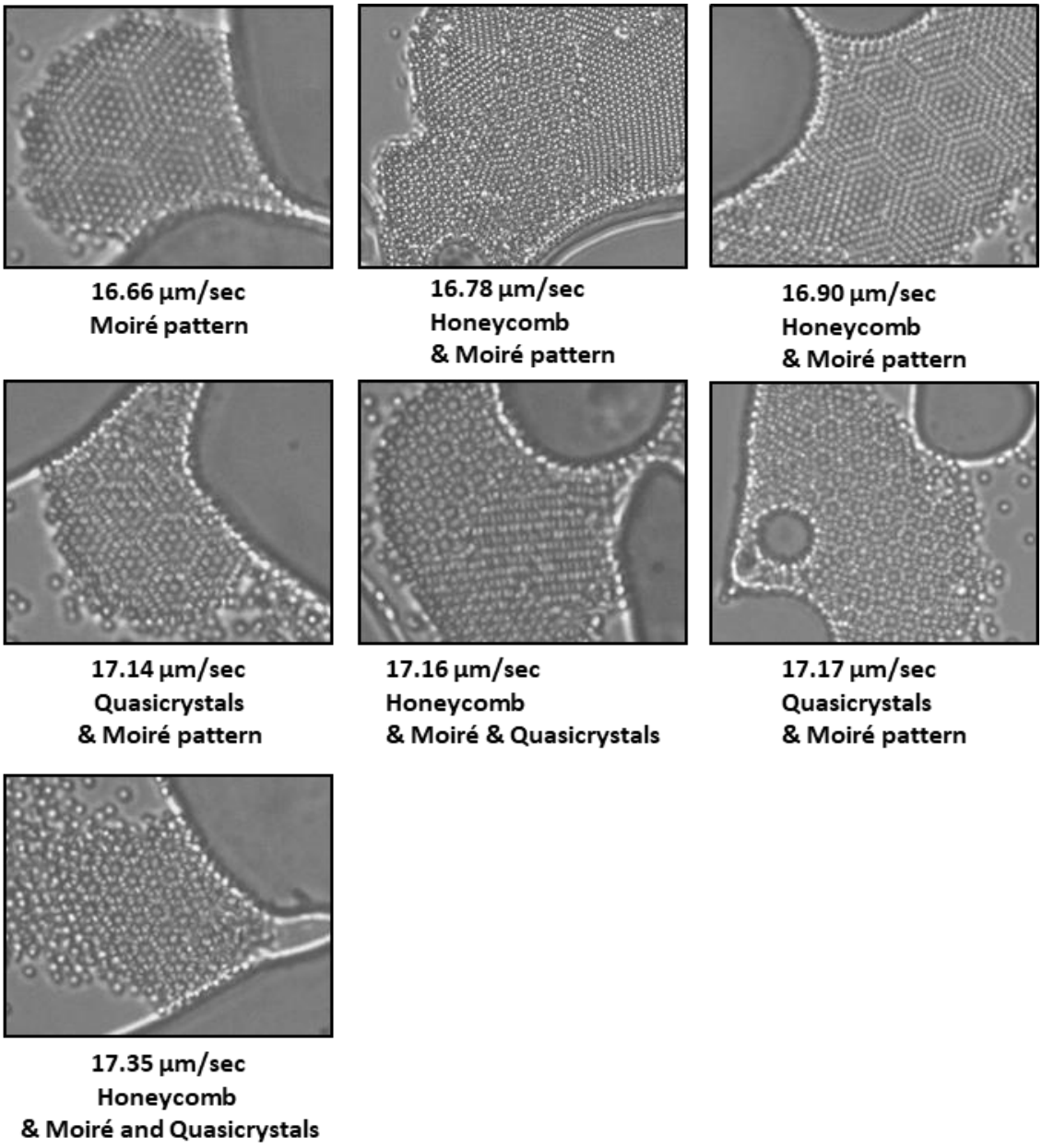

Figure 4-26 Snapshots of Brownian motion experiments for honeycomb, Moiré and Quasicrystals patterns and corresponding average Brownian motion velocities.

Table 4-1 shows descriptive statistical analysis of the results and Figure 4-27 show distribution plots provided by Jasp statistical analysis software (version 10.0). Low standard deviation in data indicates low dispersion of data points from mean value, dispersion of data points can be seen in the distribution plots Figure 4-27. Among all the patterns single layer hexagonal can be formed in high range of Brownian motion velocities, at low Brownian motion velocities (13 µm/sec – 15.18 µm/sec) only single layer hexagonal patterns were observed. Since concentration of particles, temperature, and particle size are identical for all samples and all vicinities,

the only parameter affecting Brownian motion velocity is confinement of particles or thickness, therefore it can be concluded that at these velocities the thickness is so low that no other patterns are geometrically observable.

Table 4-1 Descriptive statistical analysis of Brownian motion velocity experiments; (other patterns are listed as: Moiré, honeycomb, and quasicrystals)

	Descriptive Statistics of Brownian Motion velocity experiments				
	Rectangle	Single layer hexagonal	Square	Double layer hexagonal	Other patterns
Number of videos	12	7	10	10	7
Mean value of BM velocities (µm/sec)	15.85	14.41	16.72	16.93	16.99
Std. Deviation	0.40	0.81	0.29	0.23	0.24
Range of data (µm/sec)	1.17	2.17	0.91	0.71	0.69
Minimum BM velocity (µm/sec)	15.17	13.00	16.24	16.64	16.65
Maximum BM velocity (µm/sec)	16.35	15.18	17.16	17.35	17.35

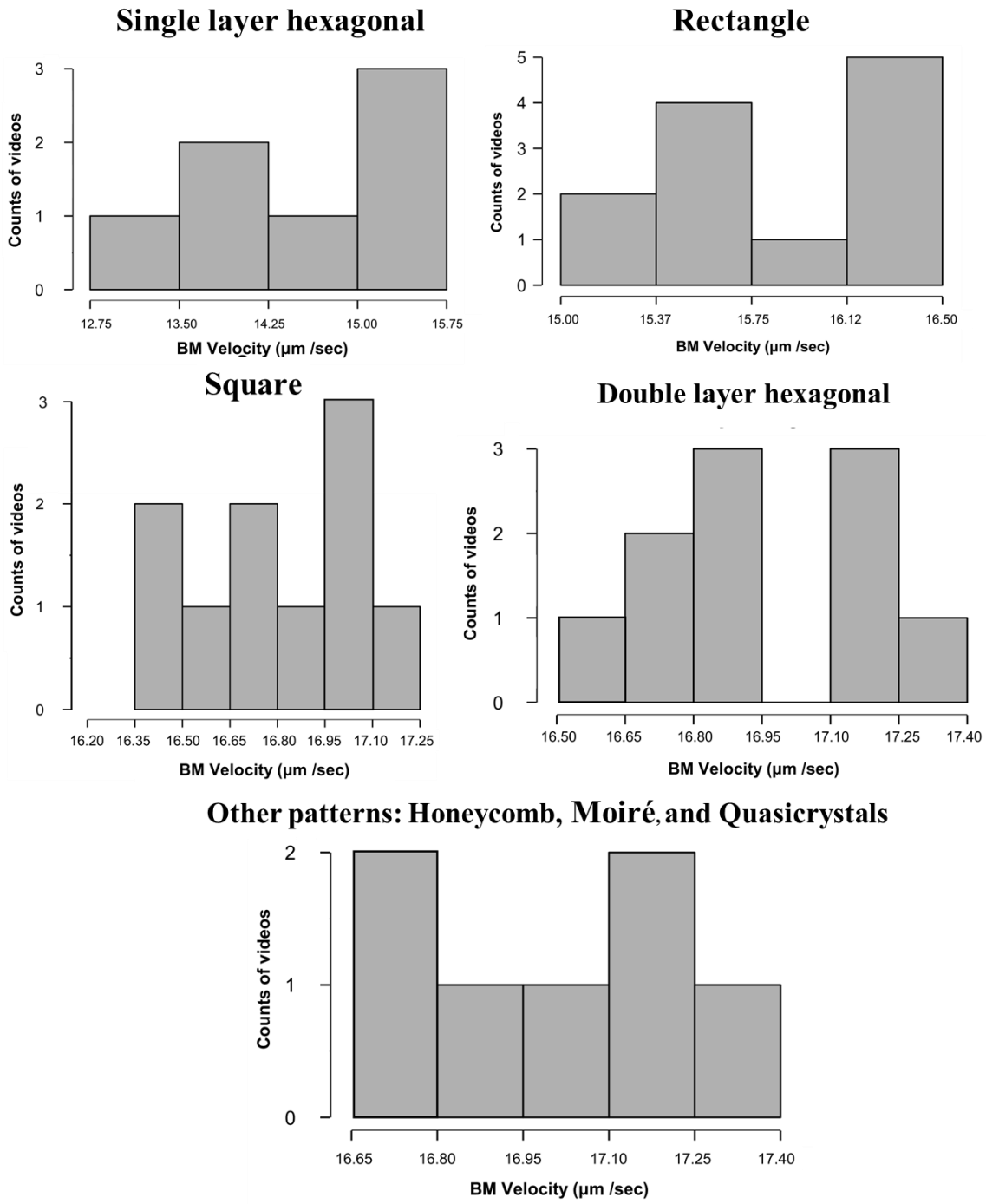

Figure 4-27 Distribution plots of Brownian motion (BM) velocity experiments with respect to the formed patterns.

Thickness is the only parameter that affects Brownian motion velocity here, therefore we expected that Brownian motion of patterns which require lower thickness to be lower than patterns which require higher thicknesses. Minimum required thickness for patterns increases in the following trend: single layer hexagonal, rectangular pattern, square pattern, double layer hexagonal, and honeycomb, Moiré

and Quasicrystals. The same trend was observed here, mean value of Brownian motion velocity increases from single layer hexagonal patterns to Moiré, honeycomb, and quasicrystals.

To show distribution of data boxplot of the statistical data is provided in Figure 4-28. It can be interpreted form this plot that single layer hexagonal patterns cannot be formed in same spatial position with square patterns, double layer hexagonal, honeycomb, Moiré and quasicrystals. Rectangular patterns cannot coexist with honeycomb, Moiré and quasicrystals and double layer hexagonal patterns.

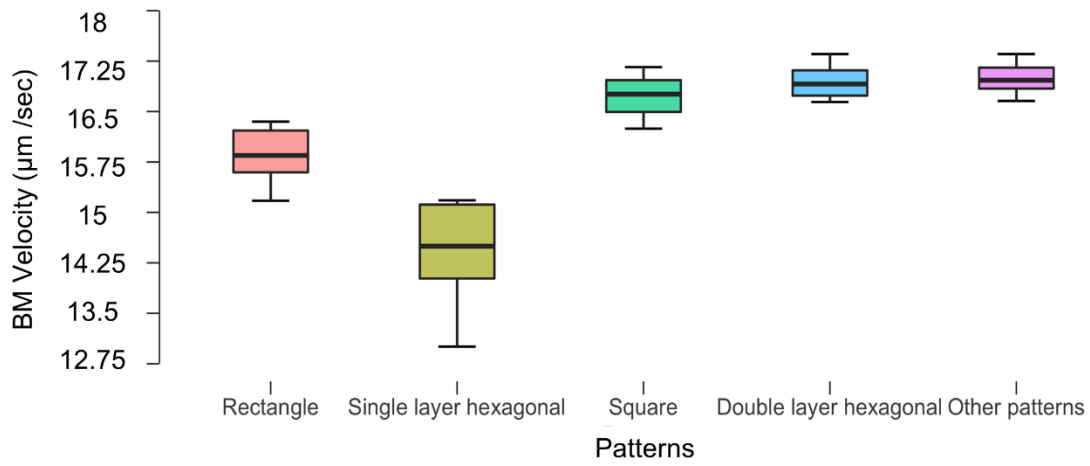

Figure 4-28 Boxplots of Brownian motion (BM) velocities of each pattern. Boxplots are a standard way to show the distribution of statistical data, it is based on five significant numbers: minimum, first quartile (Q1), median, third quartile (Q3), and maximum.

Figure 4-29 summarizes the results of 43 experimental videos, from left to right as the average Brownian velocity of particles increases. It can be seen that in low Brownian velocities (low thickness of liquid film) only single layer hexagonal patterns are observed, and as the average velocity of Brownian motion increases other patterns can be observed as well.

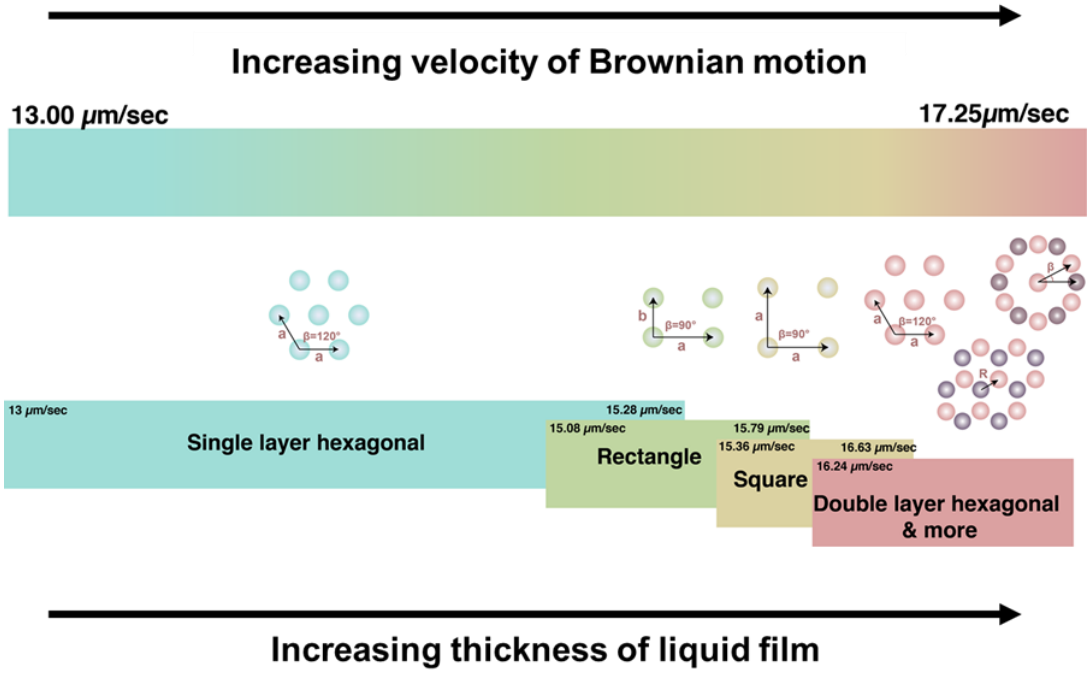

Figure 4-29 Graph summarizing range of Brownian motion velocity with respect to the type of patterns obtained in the same spatial position.

Brownian motion is the source of fluctuation in our system. As the fluctuations increase, some will be amplified and come back as larger fluctuations[115] hence there will be a possibility to jump between various patterns.

4.7.3 Patterns formed in the same spatial position

So far the results indicate that if environmental parameters change (such as Brownian motion velocity) patterns can also change. In this section we want to answer the following question: which patterns can be formed in the similar environmental parameters?

To answer this question patterns were formed around the same spatial position (~350μm * 350μm) with distances ~ 70μm apart repeatedly for 9 trials, and thickness values were measured by changing focus to make sure it does not change significantly in each spatial position. Figure 4-30, Figure 4-31, and Figure 4-32 show experimental pictures from 3 different vicinities. Figure 4-30 shows formation of rectangular patterns was observed repeatedly in one spatial position, conversion of this pattern to other patterns was not observed here. Figure 4-31 shows formation of square patterns in one spatial position, similar to rectangular patterns, conversion of this pattern to

other patterns was not observed here. Figure 4-32 shows formation of honeycomb, Moiré and Quasicrystals and double layer hexagonal patterns all in the same spatial position, unlike the square and rectangular patterns these structures can coexist, and interconvert to each other repeatedly.

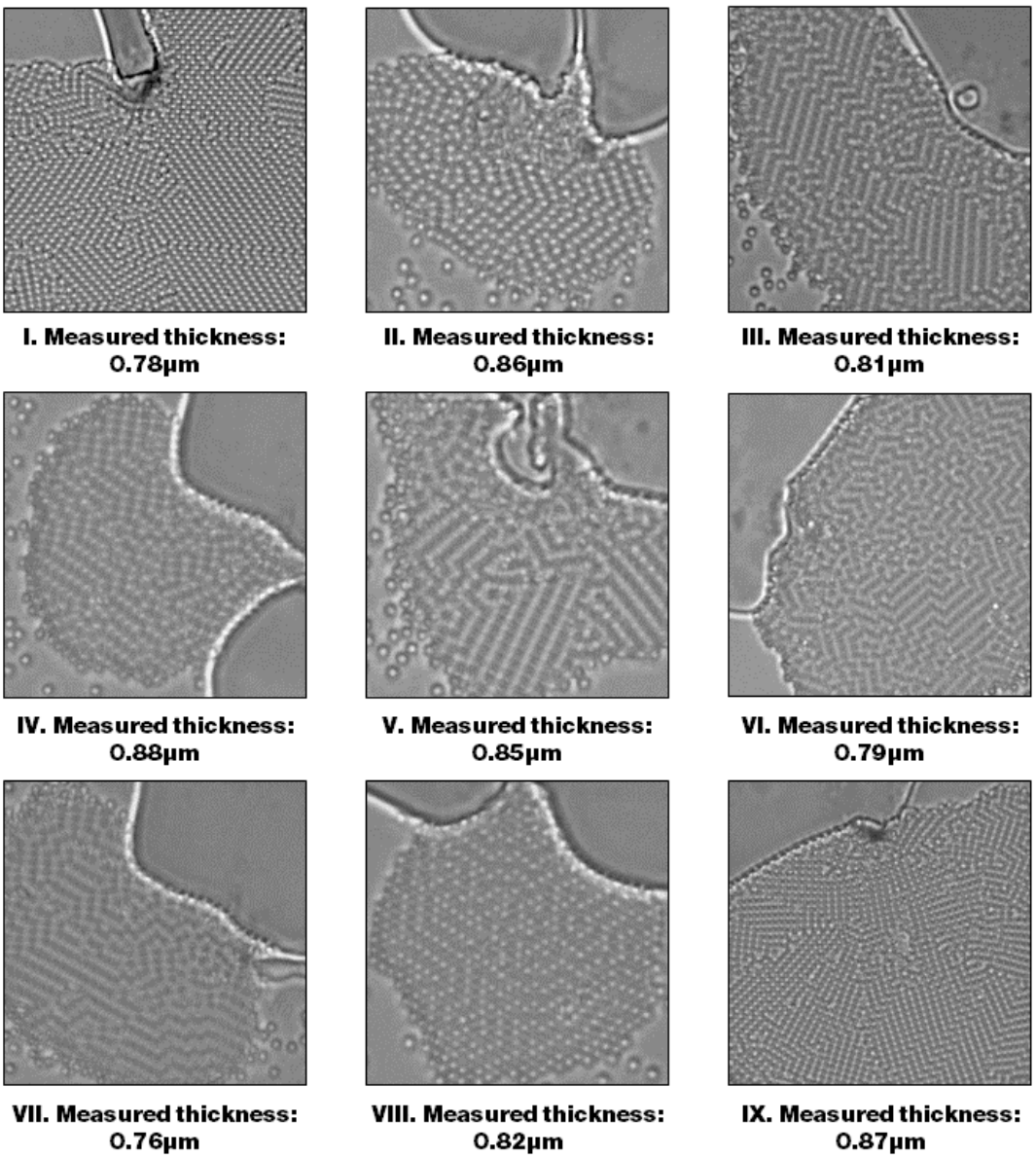

Figure 4-30 Formation of rectangular patterns repeatedly within one spatial area.

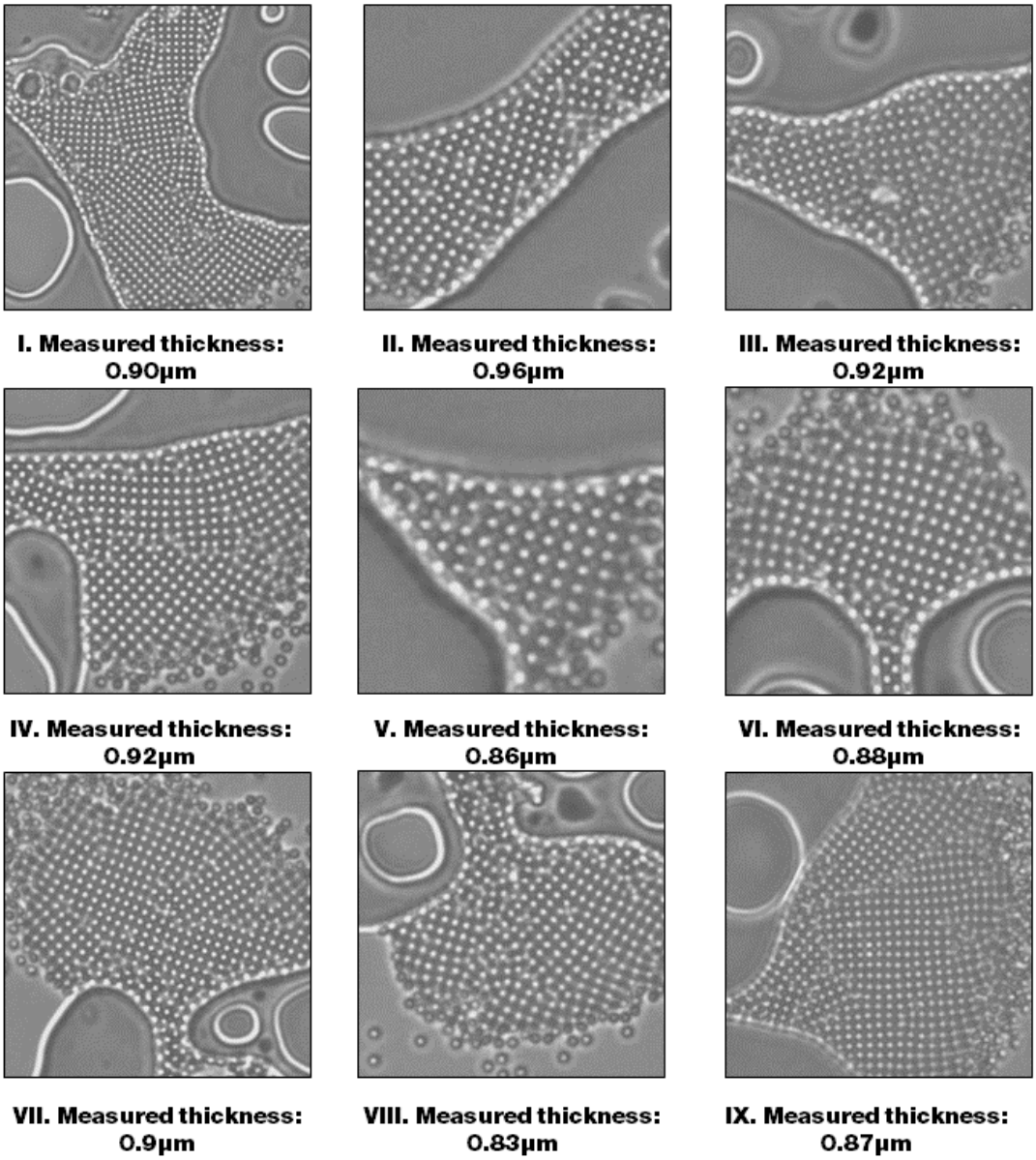

Figure 4-31 Formation of square patterns repeatedly one spatial area.

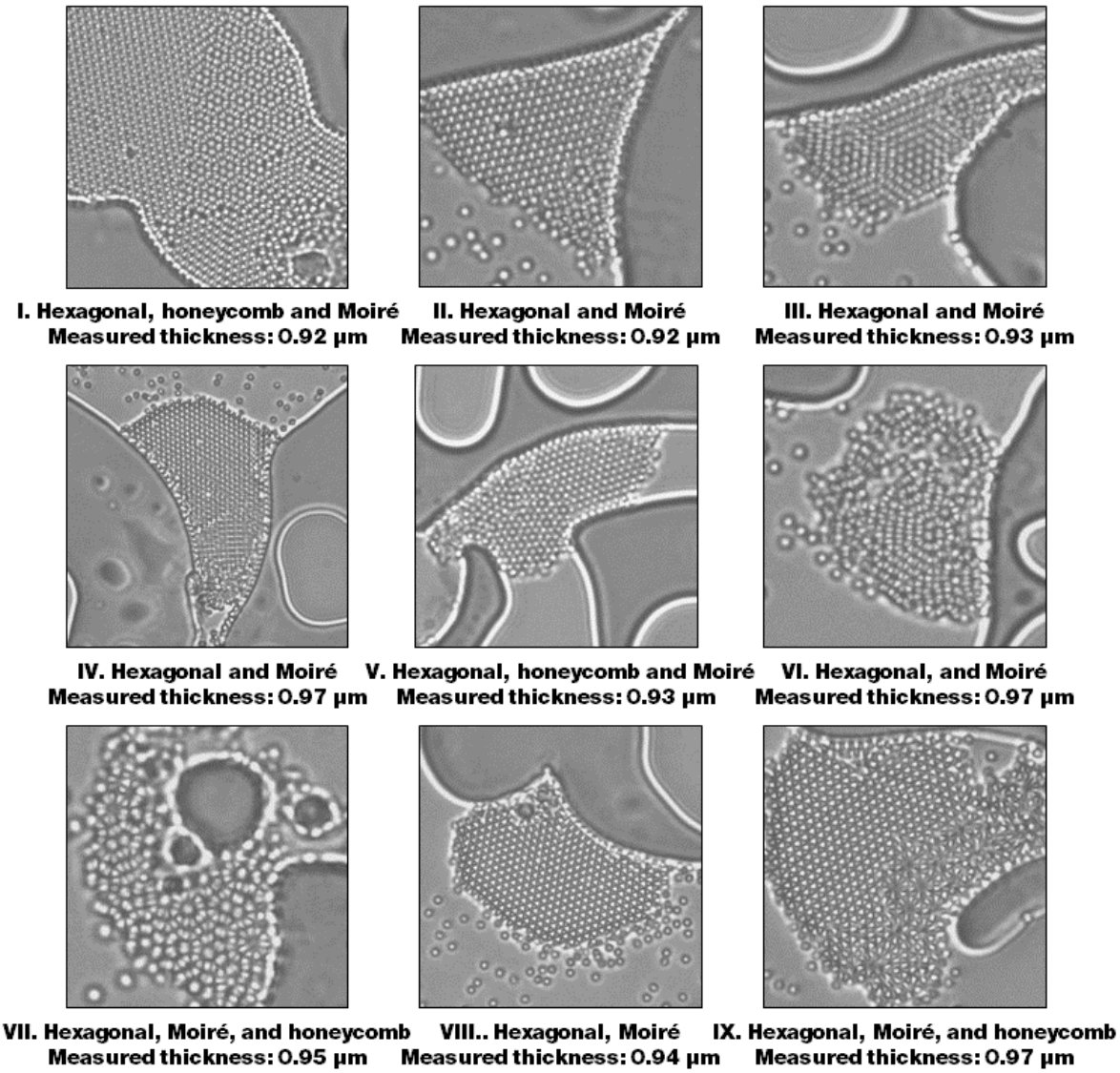

Figure 4-32 Formation of four different patterns (Double layer hexagonal, honeycomb, Moiré and Quasicrystal) one spatial area.

As discussed before, each of the observed patterns represent a steady state and an attractor in the phase space. When far from equilibrium each steady state is dependent on environmental conditions and energy flow. Since to form all pattern the laser (energy source) properties were similar, it can be concluded that formation of different patterns here is very much dependent on environmental constraints.

The experimental results of this section show the required environmental conditions for formation of double layer hexagonal, honeycomb, Moiré and quasicrystal are similar and these patterns can dynamically interconvert to each other, however, the same scenario is not true rectangular and square patterns, we were able

to see these patterns repeatedly in the same spatial position. It can be concluded that basin of attraction for Moiré patterns quasicrystals, double layer hexagonal and honeycomb patterns is close to each other in the phase space while the basin of attraction for square and rectangular patterns are far from other patterns and the conversion of these patterns were not observed.

For each trial of forming pattern, thickness of the liquid film was measured experimentally, the results are shown in Table 4-2.

Table 4-2 statistical results of measured thickness values based on type of the patterns.

	Descriptive Statistics Measured thickness values (μm)		
	Double layer hexagonal Moiré, Honeycomb, and Quasicrystals	Rectangle	Square
Valid	9	9	9
Mean (μm)	0.942	0.820	0.896
Std. Deviation (μm)	0.021	0.039	0.036
Range (μm)	0.050	0.110	0.120
Minimum (μm)	0.920	0.770	0.830
Maximum(μm)	0.970	0.880	0.950

The results show the measured average thickness value for rectangular lattice is 0.82 ±0.2 μm, the measured average thickness value for square lattice is 0.89 ±0.2 μm, and the measured average thickness value for double layer hexagonal, honeycomb and Moiré lattice is 0.94 ±0.2 μm. These values show the same trend as Brownian motion experiment results (average value of Brownian motion velocity increased from single layer hexagonal and rectangular pattern to double layer hexagonal, honeycomb and Moiré), and the theoretical thickness constraints explained earlier this section (Thickness increases from single layer hexagonal and rectangular patterns to double layer hexagonal). Within the scope of our experiments it can be concluded that thickness of the liquid film is one of the important parameters that can affect formation of colloidal crystals in this complex system.

Chapter 5

Conclusion and future perspectives

This thesis reports far from equilibrium dynamic self-assembly of colloidal crystals. A dynamic self-assembly setting introduced by S.Ilday *et al*[4]. is used for formation of quasi 2D colloidal crystals with various structures. We showed rich variety of dynamic adaptive colloidal crystals, namely all 2D Bravais lattices, honeycomb lattices, Moiré patterns, and quasicrystals. All these crystals are dynamic and adaptive, exhibiting life-like behavior such as competition, self-healing, and self-regulation. Some patterns are capable of coexisting in same spatial positions such as double layer hexagonal, quasicrystal, honeycomb, and Moiré patterns. These patterns can readily interconvert to one another in response to fluctuations in system.

Formation of these colloidal crystals can be influenced by changes in energy flux parameters (power, type, etc.), and environmental parameters (thickness of the liquid film, concentration of particles, type of the liquid, etc.). Therefore, to investigate the effect of energy flux, we studied the laser induced fluid flows which are directly related to the energy source (laser). We simulated the fluid velocity and pressure fields in two-dimension using commercial finite element software COMSOL Multiphysics. Simulations show patterns are formed in regions that fluid velocity is close to zero and pressure is lower than the rest of the sample.

Furthermore, to investigate the effect of environmental parameters on formation of patterns firstly constraints of thickness of the liquid film were studied, we calculated minimum value of required thickness for patterns to be geometrically possible. The minimum required thickness for patterns were calculated as follows: 0.5μm for single layer hexagonal pattern, 0.7μm for rectangular pattern, 0.79μm for square pattern, 0.9μm for double layer hexagonal and 0.9-1μl for various quasicrystal,

honeycomb, and Moiré patterns depending on the misorientation angle or shifting distances.

Next we studied the effect of internal fluctuations on pattern formation, we calculated the average velocity of Brownian motion of particles prior to forming each pattern using video processing algorithms. Since Brownian motion velocity depends on confinement of particles, the change in the value of Brownian motion velocity indicates change in confinement of particles in z direction (thickness). Therefore, Brownian motion velocity of particles is another indicator of thickness of the liquid film. As expected the average Brownian motion velocity increases in the same trend as minimum required thickness for each pattern, the results are as follows: 14.41 μm/sec for single layer hexagonal pattern, 15.85 μm/sec for rectangular pattern, 16.72 μm/sec for square pattern, 16.93 μm/sec for double layer hexagonal and 16.99 μm/sec for various quasicrystal, honeycomb, and Moiré patterns. Also the results show as the average velocity of Brownian motion increases more variety of patterns can be observed in system. Since Brownian motion of particles is the source of fluctuations in our system, as the fluctuations increase the possibility of toggling between available steady states is provided which the reason that we can observe variety of patterns. These results are based on our observations from 42 videos recorded from 15 samples.

Lastly, to study which patterns can interconvert to one another and coexist in same environmental parameters, we recorded videos of forming patterns in one spatial position repeatedly for 9 trials. We observed that square and rectangular patterns were formed repeatedly in one spatial position and they did not interconvert to any other patterns, while in case of double layer hexagonal, quasicrystal, honeycomb, and Moiré patterns, they all coexisted in the same spatial position and readily interconvert to each other which is the same results as observed in other experiments.

Our experimental data was extracted from ~6000 minutes of recorded videos in total. These results indicate that thickness and Brownian motion of particles (which is also related to thickness of the liquid film) as environmental factors affect formation of patterns, therefore they are parameters among many other parameters that can be used to control formation of patterns. For future works and further improvements, we suggest the improvement of simulations for various liquid film thicknesses by including particles in the fluid. Investigate other types of flows that can be formed in the system such as vortex flow or local flows and their effect on pattern formation.

The colloidal crystals formed in this system have great potential to be used as photonic papers, photonic devices, bandgap materials, in lithography or as patterned substrates for crystal growth. The challenge is to freeze the dynamic crystals in a desired structure and create a static structure with desired pattern. To achieve this firstly other parameter that can affect the shape of patterns should be identified and studied to precisely control formation of each pattern. After formation of each pattern the laser can be kept on for long time to sustain the aggregate while water is being slowly evaporated in the sample and when the sample is dried a static structure is formed in desired structure, another way to create static structure is to mix some polymeric materials into the solution which can be polymerized using UV light. Therefore, the nonequilibrium structures would be trapped in a hydrogel media. However, this methodology can have certain challenges that are yet to be discovered.

Chapter 6

Bibliography

1. Whitesides, G. M., Grzybowski, B., Whiteside, G. M. & Bartosz, G. Self Assembly at all scales. *Science,* **295**, 2418–2421 (2002).
2. Fialkowski, M. *et al.* Principles and implementations of dissipative (dynamic) self-assembly. *J. Phys. Chem. B* **110**, 2482–2496 (2006).
3. Ozin, G. A. *et al.* Nanofabrication by self-assembly. *Mater. Today* **12**, 12–23 (2009).
4. Ilday, S. *et al.* Rich complex behaviour of self-assembled nanoparticles far from equilibrium. *Nat. Commun.* **8**, 14942 (2017).
5. Mirkin, C. A., Letsinger, R. L., Mucic, R. C. & Storhoff, J. J. A DNA-based method for rationally assembling nanoparticles into macroscopic materials. *Nature* **382**, 607–609 (1996).
6. Rothemund, P. W. K. Folding DNA to create nanoscale shapes and patterns. *Nature* **440**, 297–302 (2006).
7. Zhang, J., Luijten, E., Grzybowski, B. A. & Granick, S. Active colloids with collective mobility status and research opportunities. *Chem. Soc. Rev.* **46**, 5551–5569 (2017).
8. Yan, J., Bloom, M., Bae, S. C., Luijten, E. & Granick, S. Linking synchronization to self-assembly using magnetic Janus colloids. *Nature* **491**, 578–581 (2012).
9. Palacci, J., Sacanna, S., Steinberg, A. P., Pine, D. J. & Chaikin, P. M. Living crystals of light-activated colloidal surfers. *Science,* **339**, 936–939 (2013).
10. Timonen, J. V. I., Latikka, M., Leibler, L., Ras, R. H. A. & Ikkala, O. Switchable Static and Dynamic Self-Assembly of Magnetic Droplets on Superhydrophobic Surfaces. *Science,* **341**, 253–257 (2013).

11. Grzybowski, B. A., Stone, H. A. & Whitesides, G. M. Dynamic self-assembly of magnetized, millimetre-sized objects rotating at a liquid-air interface. *Nature* **405**, 1033–1036 (2000).
12. Makey, G. *et al.* Universal Dissipative Self-Assembly: From quantum dots to colloids, microorganisms, and human cells. *submitted*
13. Ghaffari, R., Nizam, U. S., Kahraman, S., Galioglou, S. & Ilday, S. Dynamic adaptive colloidal crystals far from equilibrium. *in preparation.*
14. Anzola, D., Barbrook-Johnson, P. & I. Cano, J. Self-organization and social science. *Comput. Math. Organ. Theory* (2016).
15. Yackinous, W. S. & Yackinous, W. S. Overview of an Ecological System Dynamics Framework. *Underst. Complex Ecosyst. Dyn.* 83–91 (2015).
16. Grzybowski, B. A., Winkleman, A., Wiles, J. A., Brumer, Y. & Whitesides, G. M. Electrostatic self-assembly of macroscopic crystals using contact electrification. *Nat. Mater.* **2**, 241–245 (2003).
17. Lozano, C., Ten Hagen, B., Löwen, H. & Bechinger, C. Phototaxis of synthetic microswimmers in optical landscapes. *Nat. Commun.* **7**, 1–10 (2016).
18. Whitesides, G. M. & Grzybowski, B. Self-Assembly at All Scales. *Science*, **295**, 2418–2421 (2002).
19. Bäcklund, F. G., Pallbo, J. & Solin, N. Controlling amyloid fibril formation by partial stirring. *Biopolymers* **105**, 249–259 (2016).
20. Tien, J., Terfort, A. & Whitesides, G. M. Microfabrication through Electrostatic Self-Assembly. *Langmuir* **13**, 5349–5355 (1997).
21. Van Rossum, S. A. P., Tena-Solsona, M., Van Esch, J. H., Eelkema, R. & Boekhoven, J. Dissipative out-of-equilibrium assembly of man-made supramolecular materials. *Chem. Soc. Rev.* **46**, 5519–5535 (2017).
22. Kay, J. J. & Schneider, E. D. Life as a manifestation of the second law of thermodynamics. *Math. Comput. Model.* **19**, 25–48 (1994).
23. Ben-jacob, E. & Levine, H. The artistry of nature Pattern. *Nature* **409**, (2001).
24. Kessler, M. A. & Werner, B. T. Self-organization of sorted patterned ground. *Science* **299**, 380–383 (2003).
25. Noorduin, W. L., Grinthal, A., Mahadevan, L. & Aizenberg, J. Rationally designed complex, hierarchical microarchitectures. *Science* **340**, 832–837 (2013).
26. Campbell, C. J., Smoukov, S. K., Bishop, K. J. M. & Grzybowski, B. A.

Reactive surface micropatterning by wet stamping. *Langmuir* **21**, 2637–2640 (2005).

27. Singh, G. *et al.* Self-Assembly of Magnetite Nanocubes into Helical Superstructures. *Science* **345**, 1149–1152 (2014).
28. Ke, Y. *et al.* Three-Dimensional Structures Self-Assembled from DNA Bricks. *Science* **338**, 1177 LP – 1183 (2012).
29. Zhao, K. & Mason, T. G. Self-organized chiral colloidal crystals of Brownian square crosses. *J. Phys. Condens. Matter* **26**, (2014).
30. Cong, H. & Cao, W. Colloidal crystallization induced by capillary force. *Langmuir* **19**, 8177–8181 (2003).
31. Li, F., Josephson, D. P. & Stein, A. Colloidal assembly: The road from particles to colloidal molecules and crystals. *Angew. Chemie - Int. Ed.* **50**, 360–388 (2011).
32. Kesavamoorthy, R. & Babu Rao, C. Defects in colloidal crystal. *Bull. Mater. Sci.* **20**, 565–572 (1997).
33. Gasser, U., Weeks, E. R., Schofield, A., Pusey, P. N. & Weitz, D. A. Real-Space Imaging of Nucleation and Growth in Colloidal Crystallization. *Science* **258**, 258–262 (2014).
34. Okubo, T., Tsuchida, A. & Kato, T. Nucleation and growth processes in the colloidal crystallization of silica spheres in the presence of sodium chloride as studied by reflection spectroscopy. *Colloid Polym. Sci.* **277**, 191–196 (1999).
35. Li, B., Zhou, D. & Han, Y. Assembly and phase transitions of colloidal crystals. *Nature Reviews Materials* (2016). doi:10.1038/natrevmats.2015.11
36. Blanco, A. *et al.* Large-scale synthesis of a silicon photonic crystal with a complete three-dimensional bandgap near 1.5 micrometres. *Nature* **405**, 437–440 (2000).
37. Furumi, S., Fudouzi, H., Miyazaki, H. T. & Sakka, Y. Flexible polymer colloidal-crystal lasers with a light-emitting planar defect. *Adv. Mater.* **19**, 2067–2072 (2007).
38. Fudouzi, H. & Xia, Y. Colloidal crystals with tunable colors and their use as photonic papers. *Langmuir* **19**, 9653–9660 (2003).
39. Hoi, S. K. *et al.* A microfluidic chip with integrated colloidal crystal for online optical analysis. *Adv. Funct. Mater.* **21**, 2847–2853 (2011).
40. Zhao, Y. *et al.* Encoded Silica Colloidal Crystal Beads as Supports for Potential

Multiplex Immunoassay. *Anal. Chem.* **80**, 1598–1605 (2008).

41. Song, J. H. & Kretzschmar, I. Assembled surface-anisotropic colloids as a template for a multistage catalytic membrane reactor. *ACS Appl. Mater. Interfaces* **1**, 1747–1754 (2009).
42. Zhang, X. *et al.* Morphology and wettability control of silicon cone arrays using colloidal lithography. *Langmuir* **25**, 7375–7382 (2009).
43. Cong, H. & Yu, B. Fabrication of superparamagnetic macroporous Fe3O4 and its derivates using colloidal crystals as templates. *J. Colloid Interface Sci.* **353**, 131–136 (2011).
44. Ariga, K. *et al.* Challenges and breakthroughs in recent research on self-assembly. *Sci. Technol. Adv. Mater.* **9**, 14109 (2008).
45. Kokot, G., Piet, D., Whitesides, G. M., Aranson, I. S. & Snezhko, A. Emergence of reconfigurable wires and spinners via dynamic self-assembly. *Sci. Rep.* **5**, 1–8 (2015).
46. Li, B., Zhou, D. & Han, Y. Assembly and phase transitions of colloidal crystals. *Nat. Rev. Mater.* **1**, 1–18 (2016).
47. Snezhko, A. & Aranson, I. S. Magnetic manipulation of self-assembled colloidal asters. *Nat. Mater.* **10**, 698–703 (2011).
48. Cross, M. C. & Hohenberg, P. C. Pattern formation outside of equilibrium. *Rev. Mod. Phys.* **65**, 851–1112 (1993).
49. Manneville, P. *et al.* Propagation in Systems Far from Equilibrium: Introduction and Overview. in *Propagation in Systems Far from Equilibrium* (eds. Wesfreid, J. E., Brand, H. R., Manneville, P., Albinet, G. & Boccara, N.) 2–11 (Springer Berlin Heidelberg, 1988).
50. Getling, A. V. *Rayleigh-B nard Convection: Structures and Dynamics*. **11**, (World Scientific, 1998).
51. Pellitero, M. A., Lamsfus, C. A.´ L. & Borge, J. The Belousov−Zhabotinskii Reaction: Improving the Oregonator Model with the Arrhenius Equation. (2012).
52. Benini, O., Cervellati, R. & Fetto, P. The BZ Reaction: Experimental and Model Studies in the Physical Chemistry Laboratory. *J. Chem. Educ.* **73**, (1996).
53. Cera, L. & Schalley, C. A. Under Diffusion Control: from Structuring Matter to Directional Motion. *Adv. Mater.* **30**, 1–17 (2018).

54. Pulselli, F. M., Catalucci, M., Rossi, F. & Marchettini, N. Interaction between the Belousov-Zhabotinsky reaction and lipid membranes: A kinetic investigation. *WIT Trans. Ecol. Environ.* **138**, 339–346 (2010).
55. Zhabotinsky, A. M., Buchholtz, F., Kiyatkin, A. B. & Epstein, I. R. Oscillations and waves in metal-ion-catalyzed bromate oscillating reactions in highly oxidized states. *J. Phys. Chem.* **97**, 7578–7584 (1993).
56. Mathison, T. A. The chemical basis of morphogenesis. *Philos. Trans. R. Soc. Lond. B. Biol. Sci.* **237**, 37–72 (1952).
57. Field, R. J. *et al.* Oscillations in Chemical Systems. II. Thorough Analysis of Temporal Oscillation in the Bromate–Cerium–Malonic Acid System. *J. Am. Chem. Soc.* **94**, 8649–8664 (1972).
58. Budroni, M. A., Masia, M., Rustici, M., Marchettini, N. & Volpert, V. Bifurcations in spiral tip dynamics induced by natural convection in the Belousov-Zhabotinsky reaction. *J. Chem. Phys.* **130**, 1–8 (2009).
59. Vanag, V. K., Zhabotinsky, A. M. & Epstein, I. R. Oscillatory clusters in the periodically illuminated, spatially extended Belousov-Zhabotinsky reaction. *Phys. Rev. Lett.* **86**, 552–555 (2001).
60. Tóth, Á. & Showalter, K. Logic gates in excitable media. *J. Chem. Phys.* **103**, 2058–2066 (1995).
61. Amemiya, T., Kettunen, P., Kádár, S., Yamaguchi, T. & Showalter, K. Formation and evolution of scroll waves in photosensitive excitable media. *Chaos An Interdiscip. J. Nonlinear Sci.* **8**, 872–878 (1998).
62. Babloyantz, A. & Sepulchre, J. A. Target and spiral waves in oscillatory media in the presence of obstacles. *Phys. D Nonlinear Phenom.* (1991). doi:10.1016/0167-2789(91)90193-D
63. Mikhailov, A. S. & Showalter, K. Control of waves, patterns and turbulence in chemical systems. *Phys. Rep.* **425**, 79–194 (2006).
64. Field, R. J. & Schneider, F. W. Oscillating chemical reactions and nonlinear dynamics. *J. Chem. Educ.* **66**, 195 (2009).
65. Isakova, A. & Novakovic, K. Oscillatory chemical reactions in the quest for rhythmic motion of smart materials. *Eur. Polym. J.* **95**, 430–439 (2017).
66. Parrish, J. K., Viscido, S. V. & Grünbaum, D. Self-organized fish schools: An examination of emergent properties. *Biol. Bull.* **202**, 296–305 (2002).
67. Subramani, K., Khraisat, A. & George, A. Self-Assembly of Proteins and

Peptides and their Applications in Bionanotechnology. *Curr. Nanosci.* **4**, 201–207 (2008).

68. Schuster, H. G. Complex adaptive systems. *Collect. Dyn. Nonlinear Disord. Syst.* 359–369 (2005). doi:10.1007/3-540-26869-3_16
69. Grzybowski, B. A., Fitzner, K., Paczesny, J. & Granick, S. From dynamic self-assembly to networked chemical systems. *Chem. Soc. Rev.* **46**, 5647–5678 (2017).
70. Würger, A. Thermophoresis in colloidal suspensions driven by Marangoni forces. *Phys. Rev. Lett.* (2007).
71. Christopher, B. Tears of Wine and the Marangoni Effect. (2015). Available at: https://www.comsol.com/blogs/tears-of-wine-and-the-marangoni-effect/.
72. Berthier, J. *Theory of Wetting*. *Micro-Drops and Digital Microfluidics* (2012).
73. Metcalfe, G., Speetjens, M. F. M., Lester, D. R. & Clercx, H. J. H. *Beyond passive. Chaotic transport in stirred fluids*. *Advances in Applied Mechanics* **45**, (Elsevier Inc., 2012).
74. Hansen, C. M. Diffusion in polymers. *Polym. Eng. Sci.* **20**, 252–258 (1980).
75. The, T. O., Effect, E. R. & Er, S. Chapter 6 Physics of electrorheological fluids. *Stud. Interface Sci.* **22**, 235–340 (2005).
76. Kubo, R. The fluctuation-dissipation theorem. *Reports Prog. Phys.* **29**, 255–284 (1966).
77. Johnson, J. B. Thermal Agitation of Electricity in Conductors. *Phys. Rev.* **32**, 97–109 (1928).
78. Buschow, K. H. J. *Encyclopedia of materials : science and technology*. (Elsevier, 2001).
79. Band, Y. B. & Avishai, Y. *Quantum mechanics with applications to nanotechnology and information science*. (Academic Press, 2012).
80. Ariga, K. *et al.* Self-assembly as a key player for materials nanoarchitectonics. *Sci. Technol. Adv. Mater.* **20**, 51–95 (2019).
81. Trottenberg, T., Melzer, A. & Piel, A. Measurement of the electric charge on particulates forming Coulomb crystals in the sheath of a radiofrequency plasma. *Plasma Sources Sci. Technol.* **4**, 450–458 (1995).
82. Cheng, Z., Zhu, J., Russel, W. B. & Chaikin, P. M. Phonons in an entropic crystal. *Phys. Rev. Lett.* **85**, 1460–1463 (2000).
83. Peng, Y. *et al.* Two-step nucleation mechanism in solid-solid phase transitions.

Nat. Mater. **14**, 101–108 (2015).

84. Kosterlitz, J. M. Kosterlitz-Thouless physics: A review of key issues. *Reports Prog. Phys.* **79**, (2016).
85. Popli, P., Ganguly, S. & Sengupta, S. Translationally invariant colloidal crystal templates. *Soft Matter* **14**, 104–111 (2017).
86. Keim, P., Maret, G., Herz, U. & von Grünberg, H. H. Harmonic Lattice Behavior of Two-Dimensional Colloidal Crystals. *Phys. Rev. Lett.* **92**, 2–5 (2004).
87. Kryuchkov, N. P., Yurchenko, S. O., Fomin, Y. D., Tsiok, E. N. & Ryzhov, V. N. Complex crystalline structures in a two-dimensional core-softened system. *Soft Matter* **14**, 2152–2162 (2018).
88. Porter, D. A. & Easterling;, K. E. *Phase transformations in metals and alloys. Chapman and Hall* (Springer, 1992).
89. Portal-marco, S., Àngels, M., Arteaga, O., Ignés-mullol, J. & Corbella, C. Colloids and Surfaces A : Physicochemical and Engineering Aspects Structure and physical properties of colloidal crystals made of silica particles. *Colloids Surfaces A Physicochem. Eng. Asp.* **401**, 38–47 (2012).
90. Cong, H., Yu, B., Tang, J., Li, Z. & Liu, X. Current status and future developments in preparation and application of colloidal crystals. *Chem. Soc. Rev.* **42**, 7774–7800 (2013).
91. U, O. D. V. & Lenhoff, A. M. Colloidal crystals as templates for porous materials. 56–63 (2000).
92. Mikhael, J., Gera, G., Bohlein, T. & Bechinger, C. Phase behavior of colloidal monolayers in quasiperiodic light fields. *Soft Matter* **7**, 1352–1357 (2011).
93. Hwang, H., Park, Y. H. & Park, J. K. Optoelectrofluidic control of colloidal assembly in an optically induced electric field. *Langmuir* **25**, 6010–6014 (2009).
94. Zhang, J., Li, Y., Zhang, X. & Yang, B. Colloidal self-assembly meets nanofabrication: From two-dimensional colloidal crystals to nanostructure arrays. *Adv. Mater.* **22**, 4249–4269 (2010).
95. Khanh, N. N. & Kyung, B. Y. Facile organization of colloidal particles into large, perfect one-and two-dimensional arrays by dry manual assembly on patterned substrates. *J. Am. Chem. Soc.* **131**, 14228–14230 (2009).
96. Zhou, Z., Yan, Q., Li, Q. & Zhao, X. S. Fabrication of binary colloidal crystals

and non-close-packed structures by a sequential self-assembly method. *Langmuir* **23**, 1473–1477 (2007).

97. Zhou, Z. & Zhao, X. S. Flow-Controlled Vertical Deposition Method for the Fabrication of Photonic Crystals. *Langmuir* **20**, 1524–1526 (2004).
98. Chen, K. *et al.* Moiré nanosphere lithography: use colloidal moiré patterns as masks. *Plasmon. Met. Nanostructures Their Opt. Prop. XIII* **9547**, 95471L (2015).
99. Jiang, L., Yang, S., Tsang, B., Tu, M. & Granick, S. Vector assembly of colloids on monolayer substrates. *Nat. Commun.* **8**, 1–7 (2017).
100. Talapin, D. V. *et al.* Quasicrystalline order in self-assembled binary nanoparticle superlattices. *Nature* **461**, 964–967 (2009).
101. Mikhael, J., Roth, J., Helden, L. & Bechinger, C. Archimedean-like tiling on decagonal quasicrystalline surfaces. *Nature* **454**, 501–504 (2008).
102. Blaaderen, A. Van. Quasicrystals from nanocrystals. *Nature* **461**, 892–893 (2009).
103. Shechtman, D., Blech, I., Gratias, D. & Cahn, J. W. Metallic phase with long-range orientational order and no translational symmetry. *Phys. Rev. Lett.* **53**, 1951–1953 (1984).
104. Roichman, Y. & Grier, D. G. Holographic assembly of quasicrystalline photonic heterostructures. *Opt. Express* **13**, 5434 (2005).
105. Zhou, Z., Yan, Q., Li, Q. & Zhao, X. S. Fabrication of binary colloidal crystals and non-close-packed structures by a sequential self-assembly method. *Langmuir* **23**, 1473–1477 (2007).
106. Thompson, D. The reciprocal lattice as the Fourier transform of the direct lattice. *Am. J. Phys.* **64**, 333–334 (2005).
107. Tritton, D. J. Physical Fluid Dynamics. *American Journal of Physics* (1978).
108. The Boussinesq Approximation. Available at: https://www.comsol.com/multiphysics/boussinesq-approximation.
109. Mo, J., Simha, A. & Raizen, M. G. Broadband boundary effects on Brownian motion. *Phys. Rev. E - Stat. Nonlinear, Soft Matter Phys.* **92**, 1–13 (2015).
110. Lorentz, H. A. *Abhandlungen über theoretische Physik.* (BG Teubner, 1907).
111. Huang, K. & Szlufarska, I. Effect of interfaces on the nearby Brownian motion. *Nat. Commun.* **6**, 1–6 (2015).
112. Duda, R. O. & Hart, P. E. Use of the Hough transformation to detect lines and

curves in pictures. *Commun. ACM* (2002).

113. Nandashri D & Smitha P. An Efficient Tracking of Multi Object Visual Motion using Hungarian Method. *Int. J. Eng. Res.* **V4**, (2015).
114. Pavlov, I. *et al.* Femtosecond laser written waveguides deep inside silicon. *Opt. Lett.* **42**, 3028 (2017).
115. Yin, R. Concept and Theory of Dynamic Operation of the Manufacturing Process. in *Theory and Methods of Metallurgical Process Integration* (ed. Yin, R. B. T.-T. and M. of M. P. I.) (Academic Press, 2016).
116. Luchnikov, V., Kondyurin, A., Formanek, P., Lichte, H. & Stamm, M. Moiré Patterns in Superimposed Nanoporous Thin Films Derived from Block-Copolymer Assemblies. *Nano Lett.* **7**, 3628–3632 (2007).
117. Levine, D. & Steinhardt, P. J. Quasicrystals. I. Definition and structure. *Phys. Rev. B* **34**, 596–616 (1986).
118. Caspar, D. L. D. & Fontano, E. Five-fold symmetry in crystalline quasicrystal lattices. *Proc. Natl. Acad. Sci.* **93**, 14271 LP – 14278 (1996).
119. Janot, C. Quasicrystals. in *Neutron and Synchrotron Radiation for Condensed Matter Studies: Applications to Solid State Physics and Chemistry* (eds. Baruchel, J., Hodeau, J.-L., Lehmann, M. S., Regnard, J.-R. & Schlenker, C.) 197–211 (Springer Berlin Heidelberg, 1994). doi:10.1007/978-3-662-22223-2_9
120. Förster, S., Meinel, K., Hammer, R., Trautmann, M. & Widdra, W. Quasicrystalline structure formation in a classical crystalline thin-film system. *Nature* (2013).
121. Singh, A., Dickinson, C. & Ryan, K. M. Insight into the 3D architecture and quasicrystal symmetry of multilayer nanorod assemblies from moiré interference patterns. *ACS Nano* **6**, 3339–3345 (2012).
122. Pieranski, P., Strzelecki, L. & Pansu, B. PHYSICAL REVIEW, LETTERS Thin Colloidal Crystals. *Vor. UMZ* **50**, 900–904 (1983).

Appendix A

Codes

7.1 Matlab code for fourier transform analysis

```
close all
clear all

im=imread('~/Desktop/Thesis/Results picture/1.jpeg');
im=im(:,:,1);

im=double(im)/double(max(im(:)));
figure
imshow(im)
title('processed image')

im_f=abs(fftshift(fft2(im-mean(im(:)))));
figure
x =70;
imshow(im_f(floor(end/2)-x:floor(end/2)+x,floor(end/2)-
x:floor(end/2)+x)/max(im_f(:)))
title('reciprocal image')

drawnow
```

7.2 Matlab code for calculating average Brownian motion velocity from the built tracks

```
clear v;
c=0;

for i=1:length(x)-1

    c=c+1;

v(c)=mean(sqrt(diff(x{i}(:)).^2+diff(y{i}(:)).^2)./diff(tt{i}(:)));
    if isnan(v(c))

        v(c)=[];
        c=c-1;
    end
    if rem(i,length(x)/4)==0
        i/(length(x)/4)*100
    end
end
plot(v)
mv=mean(v)
```

Appendix B

8.1 3D illustration of 2-layer square patterns

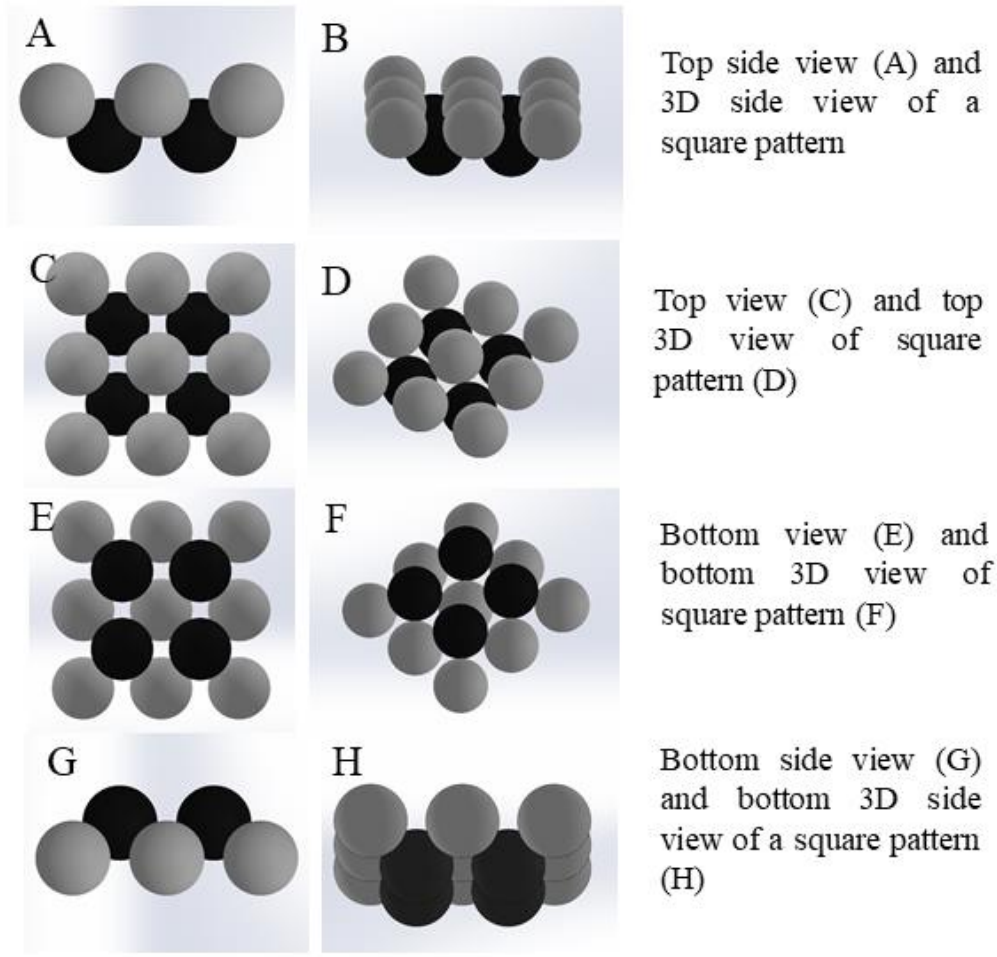

Figure 8-1 Three dimensional views of 2-layer square pattern

8.2 3D illustration of 2-layer rectangular patterns

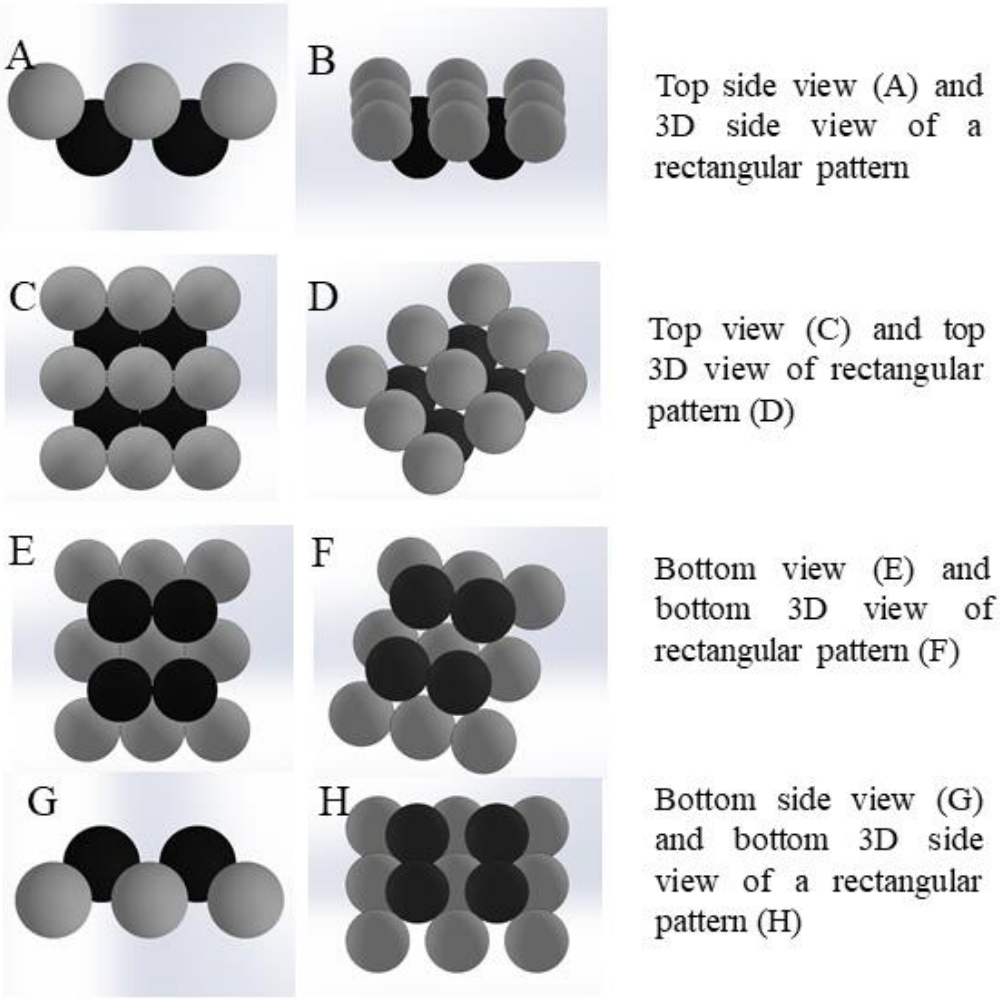

Figure 8-2 Three dimensional views of 2-layer rectangular pattern.